STEERING OF REDUNDANT ROBOTIC MANIPULATORS AND SPACECRAFT INTEGRATED POWER AND ATTITUDE CONTROL - CONTROL MOMENT GYROSCOPES

A THESIS SUBMITTED TO
THE GRADUATE SCHOOL OF NATURAL AND APPLIED SCIENCES
OF
MIDDLE EAST TECHNICAL UNIVERSITY

BY

ALKAN ALTAY

IN PARTIAL FULFILLMENT OF THE REQUIREMENTS
FOR
THE DEGREE OF MASTER OF SCIENCE
IN
AEROSPACE ENGINEERING

JANUARY 2006

Approval of the Graduate School of Natural and Applied Sciences

_____

Prof. Dr. Canan Özgen

Director

I certify that this thesis satisfies all the requirements as a thesis for the degree of Master of Science.

_____

Prof. Dr. Nafiz Alemdaroğlu

Head of Department

This is to certify that we have read this thesis and that in our opinion it is fully adequate, in scope and quality, as a thesis for the degree of Master of Science.

_____

Assoc. Prof. Dr. Ozan Tekinalp

Supervisor

Examining Committee Members

Assoc. Prof. Dr. Altan Kayran (METU,AEE) _____

Assoc. Prof. Dr. Ozan Tekinalp (METU,AEE) _____

Prof. Dr. Tuna Balkan (METU,ME) _____

Dr. İlkay Yavrucuk (METU,AEE) _____

Dr. Erhan Solakoğlu (TAI) _____

I hereby declare that all information in this document has been obtained and presented in accordance with academic rules and ethical conduct. I also declare that, as required by these rules and conduct, I have fully cited and referenced all material and results that are not original to this work.

Name, Last name :

Signature :

ABSTRACT

STEERING OF REDUNDANT ROBOTIC MANIPULATORS AND SPACECRAFT INTEGRATED POWER AND ATTITUDE CONTROL - CONTROL MOMENT GYROSCOPES

Altay, Alkan
M.S., Department of Aerospace Engineering
Supervisor : Assoc. Prof. Dr. Ozan Tekinalp

January 2006, 115 pages

In this thesis, recently developed Blended Inverse (B-inverse) steering law is applied to two different redundant actuator systems. First, repeatability of B-inverse is demonstrated on a redundant robotic manipulator. Its singularity avoidance and singularity transition performance is also demonstrated on the same actuator system. It is shown that B-inverse steering law provides singularity avoidance, singularity transition and repeatability. Second, its effectiveness is demonstrated for an Integrated Power and Attitude Control - Control Moment Gyroscope (IPAC-CMG) cluster, which can perform energy management and attitude control functions simultaneously. For this purpose, an IPAC-CMG flywheel is conceptually designed. A control policy is developed for the energy management.

Keywords: IPACS, Robotic Manipulator, Inverse Kinematics, Spacecraft Energy Storage and Attitude Control, Control Moment Gyroscope

ÖZ

YEDEKLİ ROBOTİK KOLLARIN VE UYDU TÜMLEŞİK GÜÇ VE YÖNELİM KONTROL SİSTEMLERİNDE KULLANILAN ENERJİ SAKLAYABİLEN MOMENT KONTROL JİROSKOPLARININ SÜRÜLMESİ

Altay, Alkan
Y. Lisans, Havacılık ve Uzay Mühendisliği Bölümü
Tez Danışmanı : Doç. Dr. Ozan Tekinalp

Ocak 2006, 115 sayfa

Bu tezde, iki farklı yedekli eyleyici sisteminde yakın zamanda geliştirilmiş olan Bütünleşik Ters Sürme Kanunu (B-ters) uygulaması yapılmıştır. İlk olarak, bu kanunun tekrarlama yeteneği bir yedekli robot kolu üzerinde gösterilmiştir. Buna ilaven B-ters'in tekillikten kaçma ve tekillikten geçme yetenekleri de yine aynı sistem üzerinde gösterilmiştir. B-ters'in tekillikten kaçma, tekillikten geçme ve tekrarlama işlemlerini başarıyla gerçekleştirdiği görülmüştür. İkinci olarak, B-ters'in -hem enerji saklama hem de yönelim kontrolü işlevlerini aynı anda gerçekleştirebilen- Enerji Saklayabilen Moment Kontrol Jiroskobu (ESMKJ) kümelerindeki etkinliği gösterilmiştir. Bu amaçla bir ESMKJ tekerinin kavramsal tasarımı yapılmıştır. Ayrıca enerji saklama yönetimini gerçekleştiren bir kontrol algoritması da geliştirilmiştir.

Anahtar Kelimeler: ESMKJ, Robotik Kol, Uydularda Enerji Saklama ve Yönelim Kontrolü, Sürme Kanunu

TABLE OF CONTENTS

CHAPTER 1

INTRODUCTION

1.1 Overview

An actuator is the muscle of the control system that physically makes the control possible and provides the necessary performance to the control goal. A robotic manipulator (Figure 1.1), for example, has many actuators realizing the rotation, or sliding one arm relative to the other, for the purpose of moving its end-effector in space to perform various operations.

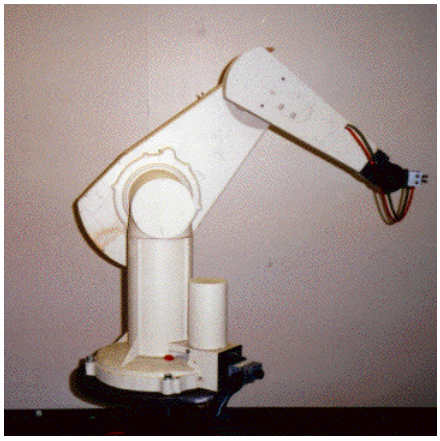

Figure 1.1 A typical robotic manipulator, a 6-DOF PUMA 560 (from [45])

A Single Gimbal Control Moment Gyroscope (CMG) (Figure 1.2), on the other hand, is another example to actuators, which is used in spacecraft attitude control systems. A CMG consists of a gimbaled flywheel that rotates at a constant speed.

Torque is produced by rotating the gimbal to change the spin axis orientation of the flywheel with respect to the spacecraft [50]. In order to produce torque in 3-axis, they are used in clusters of at least 3 CMGs. A CMG cluster of the same mass can provide much larger torque than momentum or reaction wheels. They are attracting more attention in space applications due to this torque amplification property [43].

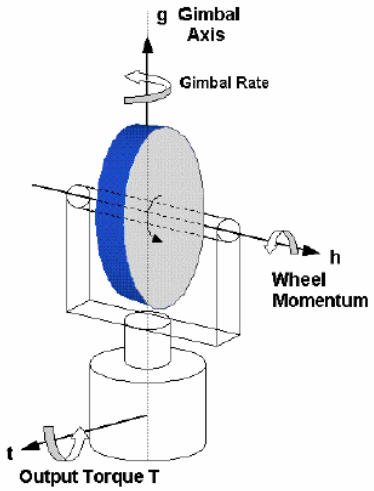

Figure 1.2. A conceptual sketch of a CMG (taken from [21])

A different kind of CMG, An Integrated Power and Attitude Control-CMG (IPAC-CMG) is considered in this study. An IPAC-CMG is a CMG with a variable flywheel spin rate. The flywheel is a part of a motor/generator unit, through which electrical energy is converted to mechanical energy and vice versa. In such a system, electrical energy may be stored in the form of mechanical energy at the flywheel and may be drawn when necessary. Thus, an IPAC-CMG system can handle both the energy storage and attitude control functions in a spacecraft. The device is discussed in more detail in the following chapters of this document. The integration of these two functions in a single system, which is known as Integrated Power and Attitude Control System (IPACS), offers significant mass

savings and numerous advantages over current implementation of using attitude control actuators and chemical batteries to store electrical energy [8].

The inverse kinematics problem in both robotic manipulators and CMG clusters has been a challenging problem. In certain configurations, which are known as singular configurations, the actuators partially or completely lose their output capabilities in certain directions. A novel solution to this inverse kinematics problem was developed in a previous study [43,51]. It is possible to avoid singular configurations or even perform smooth transitions through them with this new steering law (algorithm) called Blended Inverse (B-inverse). Although it is developed for CMG clusters, it may be used for any redundant actuator systems, such as IPAC-CMG clusters and robotic manipulators. In addition, repeatability may also be achieved using B-inverse. None of the other inverse kinematics solutions presented in the literature guarantees repeatability.

1.2 Statement of the Problem

In the present study, the main goal is to apply B-inverse steering law (algorithm) to robotic manipulators and IPAC-CMG based spacecraft IPACS. Singularity avoidance, singularity transition and repeatability capabilities of B-inverse are demonstrated through numerical simulations. Many different test cases are conducted to demonstrate the performance of B-inverse in these actuator systems. The conceptual design of an IPAC-CMG flywheel is also carried out. The feasibility and potential problems that may be encountered in constructing spacecraft IPACS are discussed. Simulation models of the system are constructed and used in the steering studies.

1.3 Previous Works

The inverse kinematics problem, or the control allocation problem, has been a challenging problem that is encountered when there are redundant actuators, i.e., robotic manipulators, CMG clusters, etc. The problem itself is well defined in [26] and [33] for CMG clusters and the analogy between manipulator and CMG clusters is defined in [7]. Interested reader may find a more extended literature survey on the CMG systems in [51]. The singularity problem in Variable Speed CMG clusters is discussed in [52].

For redundant robotic manipulators, the inverse kinematics problem and singular configurations are clearly identified in [6,7,54,34]. Two studies based on the Lie Bracketing Method discuss the repeatability in robotic manipulators [38,37]. The proposed solutions for the inverse kinematics problem can be analyzed in two groups; the singularity robust solutions and those that offer smooth transitions through singular configurations.

The singularity robust inverses disturb the solution in the neighborhood of singular configuration. SR inverse of Hanafusa and Nakamura [30] and Damped Least Squares Method [46] are two examples to this kind of solutions. The performance of these solutions is extensively manifested by means of theoretical analyses and simulation results. Unfortunately, there are several disadvantages of these methods. Disturbing the kinematics of the actuator increases the tracking error in the task space. Moreover there exists sharp velocity changes around singularity and the actuator may still experience a lock at a singular configuration.

There are three theoretically well –established solutions in the literature offering a smooth and accurate transition through singular configurations.

One of them is the Extended Jacobian Method [35] that extends the kinematic relation of the manipulator with additional constraint functions, creating a “virtual” manipulator whose kinematics differs from the original one. It is possible to guarantee repeatability by this method choosing an appropriate constraint function. Algorithmic singularity problem and the extra computational load brought by adding an extra function are the two drawbacks of this method.

Another one is the Normal Form Approach [42], which proposes to solve the inverse kinematics in its quadratic normal form around singularities. In the remaining locations of the configuration space, far from singularities, basic Newton algorithm is used. These two solutions are then “glued” to each other. This approach enables to pass through singularity in a smooth and accurate fashion but a significant increase in computational effort comes into the picture and also two different algorithms instead of one are now needed in this method with a suitable switching between them.

The third method is the Modified Jacobian Method [10]. In this method, the kinematical relation of the manipulator is modified around the singularity. Modified Jacobian Method works for the most common forms of the singularities. Interpolation of a few configurations around a singular configuration is performed to guarantee a perfectly smooth transition through singularities. It handles the inverse kinematics problem locally around singularity, just like the normal form approach, while it does not provide any global solution to the inverse kinematics problem. In such a situation, additional algorithms shall be used to realize repeatability.

The Blended Inverse developed in [51] performs both singularity avoidance and smooth transition through singular configurations, it offers repeatable solutions, while it is not computationally too demanding.

IPACS is a fairly old concept that regained its popularity in the last decade. The idea of energy storage in rotating flywheels goes as back as 1961 [36], while the name IPACS was originally used in a paper in 1973 [4]. The subject is evaluated in many aspects through comparisons to its competitor systems in [8] and [13]. The results of the experiments running on IPACS are presented in [18]. Reference [3] is another study concentrated on the application of IPACS on small spacecraft. The use of Variable Speed CMG in IPACS, on the other hand, is considered in [12,53]. A more extensive overview of the related literature may be found in [14] and [5].

1.4 Original Contributions

In this thesis, B-inverse steering law is employed in robotic manipulator systems. Its performance in singularity avoidance and transition are demonstrated. It is also demonstrated that B-inverse provides repeatability to redundant actuator systems.

Control algorithms and simulation models for IPAC-CMG cluster and spacecraft IPACS are constructed. Also, a conceptual IPAC-CMG flywheel design is presented. B-inverse is employed in IPAC-CMG cluster and spacecraft IPACS simulation models. Numerical simulations are performed to evaluate the constructed algorithms. The means of using B-inverse for combined attitude control and energy management is presented.

1.5 Scope of the Thesis

In Chapter 2, the inverse kinematics problem in redundant actuator systems is discussed through redundant robotic manipulators and the simulation results for a 3-link planar robotic manipulator are presented.

In Chapter 3, attitude control and energy storage operations in space applications and the units that carry out these operations are reviewed. IPACS is introduced and compared against their traditionally used competitors.

Chapter 4 is dedicated to the IPAC-CMG systems. First the principles of the IPAC-CMG are given and the mechanical analogy between IPAC-CMG clusters and robotic manipulators are presented. An energy management algorithm is also introduced. Then the simulation results are given.

In Chapter 5, the simulation model of the spacecraft IPACS that employs the IPAC-CMG system and the control algorithms of Chapter 4 is presented and the simulation results are given.

The concluding remarks and future work are given in Chapter 6.

In Appendix A the conceptual design of IPAC-CMG flywheel is given. Appendix B presents the optimization code used in the studies concerning the robotic manipulators.

CHAPTER 2

ROBOTIC MANIPULATORS

2.1 Introduction

In this chapter robot manipulator control problem is introduced. For this purpose, kinematics equations of robot manipulators are presented and inverse kinematics problem is stated. The commonly used Moore Penrose Pseudo Inverse and Blended Inverse kinematics algorithms (or steering laws) are introduced next. The results of the simulations for three test cases are presented and simulation results are given. At the end of the chapter, a general discussion is given.

2.2 Kinematics of Robotic Manipulators

A robotic manipulator is an actuator system consisting of a series of segments where articulation is realized through prismatic or revolute joints [24]. The kinematics relation between the end effector and the joint degrees of freedom may be written as:

$$\mathbf{x} = f(\boldsymbol{\theta}) \tag{2.1}$$

where $\mathbf{x}$ is the vector defining the position and posture of the end effector and while the vector $\boldsymbol{\theta}$ defines the joints degrees of freedom. Thus, for the desired $\mathbf{x}$ the required $\boldsymbol{\theta}$ needs to be calculated. For this purpose the inverse of the relation of Eq. 2.1 is required. The kinematics relation f is non-linear. In differential form the equation may be expressed as:

$$\boldsymbol{\delta x} = \frac{\partial f}{\partial \boldsymbol{\theta}}.\boldsymbol{\delta\theta} = \mathbf{J}.\boldsymbol{\delta\theta} \tag{2.2}$$

This equation is the differential relation between end effector motion and joint motion and used in position feedback control systems. The control of the manipulator may also be realized by velocity-based control or acceleration based control. But position control is selected since the position of the end-effector is often more important than velocity or acceleration. This differential relation will also be used in the simulations performed in this thesis. In the equation, the coefficient matrix $\mathbf{J}$ is called the Jacobian matrix. From Eq. 2.2, the inverse relation may be found as:

$$\boldsymbol{\delta\theta} = \mathbf{J}^{-1}.\boldsymbol{\delta x} \tag{2.3}$$

For a non-redundant system, for which the number of joint space coordinates is equal to the number of coordinates of the operational space, $\mathbf{J}$ is square, then the inversion of the Jacobian matrix is trivial (as long as $\det(\mathbf{J}) \neq 0$) and the solution is unique. However, in a redundant system, the number of joint coordinates is more than the number of operational space coordinates. So $\mathbf{J}$ becomes a rectangular matrix having more columns than its rows, which cannot be inverted directly as in the case of non-redundant systems. There exist multiple solutions in the joint space for a desired position of the end effector in the task space. In other words, the inversion of the $\mathbf{J}$ becomes an optimization problem for the redundant systems, in which the best solution should be selected according to some optimization criterion. This selection process is also called redundancy resolution. And the solutions proposed to find the appropriate joint motion for the desired end effector motion are called steering laws, inverse kinematics algorithm.

The main superiority of redundant systems to non-redundant ones is their null motion ability. The null motion is defined as the motion that does not generate any end-effector motion, that is

$$\delta \mathbf{x} = \mathbf{J}.\delta\boldsymbol{\theta}_{null} = \mathbf{0} \tag{2.4}$$

A redundant manipulator can move through its multiple $\boldsymbol{\theta}$ solutions without changing the position of its end effector by this null motion. When there is redundancy, singularity avoidance, obstacle avoidance, performance optimization are possible [2].

The most common inverse for a rectangular matrix is the minimum two-norm solution known as Moore-Penrose pseudo inverse (MP-inverse). Whitney [49] offered the use of MP-inverse for redundant manipulators. It is given as:

$$\delta\boldsymbol{\theta}^{MP} = \mathbf{J}^T.(\mathbf{J}.\mathbf{J}^T)^{-1}.\delta\mathbf{x} \tag{2.5}$$

The singularity is still a problem in this case, since the above equation obviously fails when $\mathbf{J}$ loses rank and becomes singular; $\det(\mathbf{J}.\mathbf{J}^T)$ becomes zero and $(\mathbf{J}.\mathbf{J}^T)$ becomes uninvertible. The manipulator loses its capability to produce motion for its end effector in a certain direction. The situation is illustrated in Figure 2.1. The singular direction is the direction of the eigenvector of the minimum eigenvalue of $\mathbf{J}.\mathbf{J}^T$. This expression, with a square –root, is defined as the manipulability measure in robotics:

$$M = \sqrt{\det(\mathbf{J}.\mathbf{J}^T)} \tag{2.6}$$

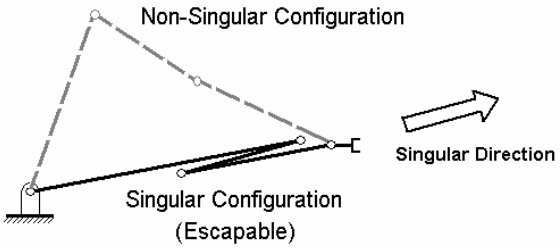

Figure 2.1 Physical illustration of a singular configuration for a redundant manipulator

Manipulability measure indicates how much close is the manipulator to the nearest singular joint configuration. As the measure gets smaller, the manipulator is more close to a singular configuration. It is also a performance measure for a manipulator that defines the quality of the controllability of the end-effector through joint motions. The manipulability measure drops to zero at a singular configuration, denoting that the controllability is lost for the singular direction [7].

There are different singularity types for a robot manipulator and a classification of the singular configurations of robot manipulators can be found in [6,34]. Basically, in a singular configuration, three possibilities exist: (1) configurations in which null motion is not possible, (2) configurations in which null motion is possible but the null motion moves the manipulator along a set of singular configurations, (3) configurations in which null motion is possible and the null motion reconfigure the robot into a non-singular configuration. The first two possibilities where the singularity cannot be escaped by the help of the null motion are called "inescapable singularity", while the third type is known as "escapable singularity". The inescapable and escapable singularity types for the manipulators are illustrated in Figure 2.2.

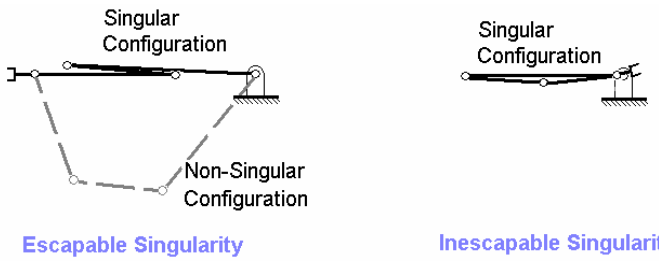

Figure 2.2 Singularity types in redundant robotic manipulators

The repeatability of the inverse kinematics algorithm is also a desirable property. Many of the proposed solutions for the inversion of $\mathbf{J}$, such as MP-inverse do not guarantee repeatability, i.e., when a closed path $\mathbf{x}(t)$ in task space is tracked by the

end effector, the correspondingly generated path $\boldsymbol{\theta}(t)$ in joint space is not closed in general. The repeatability problem was raised originally by Klein and Huang [19] where several simulation experiments were run, using the Moore-Penrose pseudo inverse steering law. It is shown that this steering law does not generate repeatable joint history, but if a cyclic end effector trajectory is repeated sufficiently, the joint trajectories appear to converge to repeatable limit cycles. Repeatability is also subject of two other studies, in which analytical methods are developed to identify the repeatability of the steering laws [38,37].

There are many steering laws in the literature that proposes different approaches to the inverse kinematics problem of redundant actuator systems, some of which are briefly discussed in Section 1.3. In fact, these problems point out the need for control over joint configurations at any desired location on the trajectory within a feedback control system. Blended Inverse (B-inverse) is a steering logic that is developed to have the control on the configurations of redundant actuator systems while it is performing a given task. It is shown in [51] that it provides singularity avoidance, smooth singularity transition and repeatable actuator configurations for CMG clusters. The following discussion on the derivation and description of B-inverse is due to [51]. However, the notation is modified for robotic manipulators.

B-inverse steering law is the solution of a mixed minimization problem, which aims to realize the two goals simultaneously: to generate the desired end effector trajectory, $\mathbf{x}$, and to control the joint configurations, $\boldsymbol{\theta}$.

$$\min_{\dot{\boldsymbol{\theta}}} \frac{1}{2} \{\dot{\boldsymbol{\theta}}^T{}_{err}.\mathbf{Q}.\dot{\boldsymbol{\theta}}_{err} + \dot{\mathbf{x}}^T_{err}.\mathbf{R}\dot{\mathbf{x}}_{err}\} \tag{2.7}$$

where $\dot{\boldsymbol{\theta}}_{err} = \dot{\boldsymbol{\theta}} - \dot{\boldsymbol{\theta}}_{desired}$, $\dot{\mathbf{x}}_{err} = \mathbf{J}.\dot{\boldsymbol{\theta}} - \dot{\mathbf{x}}$, while $\mathbf{Q}$ and $\mathbf{R}$ are symmetric positive definite weighting matrices. The solution of this problem gives us the following expression for the joint rates:

$$\dot{\boldsymbol{\theta}}_{BI} = (\mathbf{Q} + \mathbf{J}^T.\mathbf{R}.\mathbf{J})^{-1}(\mathbf{Q}.\dot{\boldsymbol{\theta}}_{desired} + \mathbf{J}^T.\mathbf{R}.\dot{\mathbf{x}}) \tag{2.8}$$

$\dot{\boldsymbol{\theta}}_{BI}$ is the solution vector that is obtained by B-inverse. The manipulator will follow the requested trajectory closely while also following $\dot{\boldsymbol{\theta}}_{desired}$. The relative importance attained to these two tasks would be determined through the weighting matrices $\mathbf{Q}$ and $\mathbf{R}$. This steering logic apparently blends the desired joint rates that are going to take the system to a desired joint configuration and the required end effector velocity. A more simplified version of Eq. 2.8 is more convenient to use, when the weighting matrices are considered as $\mathbf{Q} = q.\mathbf{I}_n$ and $\mathbf{R} = \mathbf{I}_m$:

$$\dot{\boldsymbol{\theta}}_{BI} = (q.\mathbf{I}_n + \mathbf{J}^T.\mathbf{J})^{-1}(q.\dot{\boldsymbol{\theta}}_{desired} + \mathbf{J}^T.\dot{\mathbf{x}}) \tag{2.9}$$

where $\mathbf{I}_i$ is an $(i \times i)$ identity matrix. In this simplified equation, q is the blending coefficient that determines the importance between $\dot{\boldsymbol{\theta}}_{desired}$ and $\dot{\mathbf{x}}$ commands. It is usually a very small number, on the order of 10^{-3} to 10^{-6}, since the primary task for the manipulator has to be to follow the desired end-effector trajectory as closely as possible. The key point here is that, if the $\dot{\boldsymbol{\theta}}_{desired}$ profile supplied to B-inverse also realizes the same desired end-effector trajectory, the end-effector would realize the desired trajectory in the task space while following the joint trajectory dictated by the $\dot{\boldsymbol{\theta}}_{desired}$ command. On the other hand, if the $\dot{\boldsymbol{\theta}}_{desired}$ command dictates radically high joint velocities or tries to steer the end effector to a point that is not on the desired trajectory, B-inverse simply neglects the $\dot{\boldsymbol{\theta}}_{desired}$ command and follows the trajectory in a devoted manner, since the blending coefficient q is a very small number.

Calculation of $\dot{\boldsymbol{\theta}}_{desired}$ is critically important in employing B-inverse. Many different ways may be proposed for the adjustment of the $\dot{\boldsymbol{\theta}}_{desired}$. One possible way that also seems operationally suitable for the manipulators is to determine $\dot{\boldsymbol{\theta}}_{desired}$

through nodes in the trajectory. A node is defined as a joint configuration for a specific position of the end effector in the task space. In the trajectory to be followed by the end effector, suitable joint configurations are selected for some points on the desired trajectory of the end effector (Figure 2.3). The manipulator is asked to have the node configurations at these specified points on the trajectory, as seen in Figure 2.3. The $\dot{\boldsymbol{\theta}}_{desired}$ value to be supplied to B-inverse may instantaneously be calculated by the following formula.

$$\dot{\boldsymbol{\theta}}_{desired} = \frac{\boldsymbol{\theta}_{node} - \boldsymbol{\theta}_{current}}{t_{node} - t_{current}} \qquad \text{for} \quad t_{current} < t_{node} \tag{2.10}$$

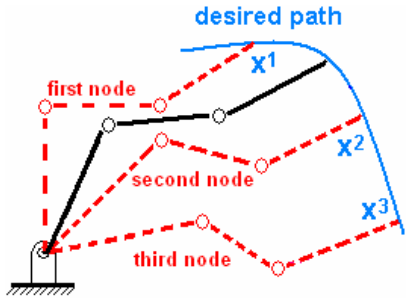

Figure 2.3 Nodes on a desired path

The method of determining $\dot{\boldsymbol{\theta}}_{desired}$ using pre-determined node configurations is called as pre-planned steering, since the desired trajectory of the end effector should be known in advance. It is also possible to supply $\dot{\boldsymbol{\theta}}_{desired}$ to the B-inverse in an online manner, without knowing the task of the manipulator in advance. But, in many uses of robotic manipulators the task of the manipulator is always known before it starts to operate and the node determination for the manipulators is a relatively simple process that can be performed in a very short time, without bringing any significant computational burden to the system. The selection process of the nodes would be discussed numerically in the coming sections including simulations, which would be a more clear and satisfactory discussion.

With this trajectory and node following properties, B-inverse can be used to avoid obstacles, to assure repeatability, to avoid singularities or even perform through them with a careful selection of nodes. After this introductory discussion on B-inverse, it is intended to demonstrate its applicability and performance solely over the redundant robot manipulators in the rest of this chapter.

2.3 Simulation Model

A 3-link planar manipulator is employed in the simulations since it is the simplest and also the most popular manipulator configuration used in the relevant literature. A sketch of the 3-link planar manipulator is given in Figure 2.4. When the joint angles are measured as shown in Figure 2.4, the kinematical equations expressing the position of the end effector in the task space is given by:

$$\begin{aligned} x_1 &= l_1.c_1 - l_2.c_{12} - l_3.c_{123} \\ x_2 &= l_1.s_1 - l_2.s_{12} - l_3.s_{123} \end{aligned} \tag{2.11}$$

in which $c_{ij..k}$ and $s_{ij..k}$ is the short hand notation representing $\cos(\theta_i + \theta_j + ... + \theta_k)$ and $\sin(\theta_i + \theta_j + ... + \theta_k)$ respectively. In the simulations, the link lengths are taken as $l_1 = 2\,\text{m}, l_2 = 1\,\text{m}, l_3 = 1\,\text{m}$.

The Jacobian matrix of this manipulator, which will be used in the inverse kinematics calculations then becomes

$$\mathbf{J}(\boldsymbol{\theta}) = \frac{\partial f(\boldsymbol{\theta})}{\partial \boldsymbol{\theta}} = \begin{bmatrix} (-l_1.s_1 + l_2.s_{12} - l_3.s_{123}) & (l_2.s_{12} - l_3.s_{123}) & (l_3.s_{123}) \\ (-l_1.c_1 + l_2.c_{12} - l_3.c_{123}) & (l_2.c_{12} - l_3.c_{123}) & (l_3.c_{123}) \end{bmatrix} \tag{2.12}$$

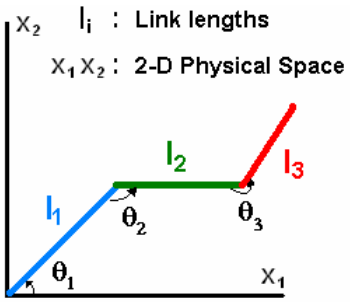

Figure 2.4 Sketch of a 3-link planar robotic manipulator

Robot manipulator dynamic equations contain many non-linearities due to the change of the moment of inertia, gravity, Coriolis and centrifugal forces. However, to focus the discussion on the inverse kinematics problem, the dynamics of the manipulator is modeled in a simplified manner as the joint dynamics, which is taken from Reference [30]:

$$0.01\ddot{\theta}_i + 0.1\dot{\theta}_i = u_i \quad \text{for } i = 1,2,3 \tag{2.13}$$

where subscript indicates the related joint. This representation of the dynamics shows second order characteristics with $\omega_n = 10$ rad/s and $\zeta = 0.5$ when the position feedback loop is closed with unity gain.

The closed loop block diagram of the manipulator and the controller system is given in Figure 2.5. In the block diagram, the direct kinematics block contains Eq. 2.11. It takes the current joint angles as an input and outputs the current position of the end effector. The robot dynamics block contains the model of the manipulator given in Eq. 2.13. The power amplifier block of the dynamical model converts its input, the position error, to the input command **u** of the robot dynamics block. In this simulation study, the input of the manipulator dynamics is directly the position error, so no amplification is performed in this block. Instead it performs the saturating characteristic of the joints, so the joint velocities are limited in this block. This block consists of the equations:

$$\mathbf{u}_i = \begin{cases} \delta\theta_i & \text{if } \|\delta\theta_i\| \le u_{\max} \\ u_{\max}.\,\mathrm{sgn}(\delta\theta_i) & \text{if } \|\delta\theta_i\| \ge u_{\max} \end{cases} \tag{2.14}$$

where $i = 1,2,3$ again stands for each joint and $u_{\max} = 3$ deg is taken. This $u_{\max}$ selection limits the joint velocities to 30 deg/sec, since the coefficient of $\dot{\theta}_i$ in Eq. 2.13 is 0.1. The inverse kinematics block, or the motion resolution block, accepts the position error between current position and the desired position of the end effector and calculates the angular joint motion required. The steering law employed in this block performs this calculation. So any steering law to be tested, i.e., MP-inverse or B-inverse, should be placed here.

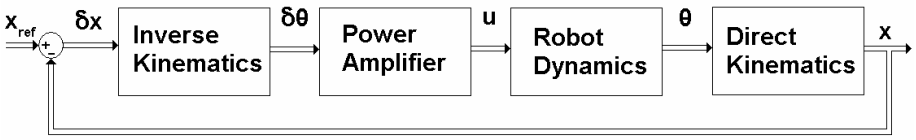

Figure 2.5 Block diagram of robot manipulator control system [30]

Another issue that needs to be revealed in this section is the selection of the nodes to be used in Eq. 2.10 to calculate $\dot{\boldsymbol{\theta}}_{desired}$. One may also find studies on node selection in References [22] and [23]. Since a manipulator is a system that is relatively easy to visualize, the node determination process starts with a heuristic step. The end effector position of the desired node configuration is already known beforehand, the node configuration is first guessed in the neighborhood of the desired node configuration. This first guess is used to specify the upper and lower constraints to $\boldsymbol{\theta}$ in the optimization routine constructed for node determination of the robot manipulators. The optimization routine starts with an initial guess in between the constraints and performs the following optimization problem to find a local minimum.

$$\min_{\boldsymbol{\theta}} \left(\mathbf{x}_{node} - \mathbf{x}\right)^2 \qquad \text{subject to} \qquad \boldsymbol{\theta}_{lower} \le \boldsymbol{\theta} \le \boldsymbol{\theta}_{upper} \tag{2.15}$$

The "fmincon" command of the MatLab Optimization Toolbox is used in the construction of the software of this optimization process. When the cost is sufficiently minimized, a joint angle set between the constraints provided in Eq. 2.15 is determined, which also satisfies the end effector position of the node. Multiple node configurations may be obtained by this code. The constructed MATLAB code is presented in Appendix B.

2.4 Simulation Results

In this section, the simulation results of three different test cases are presented. These test cases are designed to demonstrate the capabilities and performance of B-inverse steering law under certain critical conditions such as a singularity or a repeatable situation. The end effector tracks in the test cases are chosen to include these critical configurations. MP-inverse simulation results are presented first, to show the characteristic of each test case. MP-inverse is the most basic and natural solution to the inverse kinematics problem, the character of the test cases is best observed through MP-inverse results. After that the simulation results of B-inverse are given. In all the numerical simulations of robotic manipulators, the blending coefficient of B-inverse is taken as $q = 1 \times 10^{-5}$.

2.4.1 Repeatability Test

In this first test case, the repeatability performance of the B-inverse is demonstrated on a closed path to be followed routinely. In addition, the tracking performance of B-inverse with a false nodal joint angle set is also illustrated. A trajectory is designed in which the end effector would follow a closed path for a couple of times. In such a trajectory, a repeatable steering law should steer the

manipulator through a closed path in the joint angles space. The time history of the selected trajectory is given below:

$$
\begin{aligned}
x_1 &= x_1^0 + \sin(\frac{\pi}{15}t) \\
x_2 &= x_2^0 - 1 + \cos(\frac{\pi}{15}t)
\end{aligned}
\qquad \text{for} \quad 0 \le t \le 105\,\text{sec} \quad \text{and} \quad 135 \le t \le 210\,\text{sec}
$$

$$
\begin{aligned}
x_1 &= x_1^0 + 0.5\sin(\frac{\pi}{15}t) \\
x_2 &= x_2^0 - 2.5 - 0.5\cos(\frac{\pi}{15}t)
\end{aligned}
\qquad \text{for} \quad 105 \le t \le 135\,\text{sec}
\tag{2.16}
$$

where $(x_1^0, x_2^0) = (1.5\,\text{m}, 0.866\,\text{m})$ is the initial position of the end effector. The initial joint configuration of the manipulator is arbitrarily selected. In task space, this trajectory equation generates two different circles tangent to each other as seen in Figure 2.6. Both large and small circles seen in the figure are traversed once in 30 seconds by the end effector.

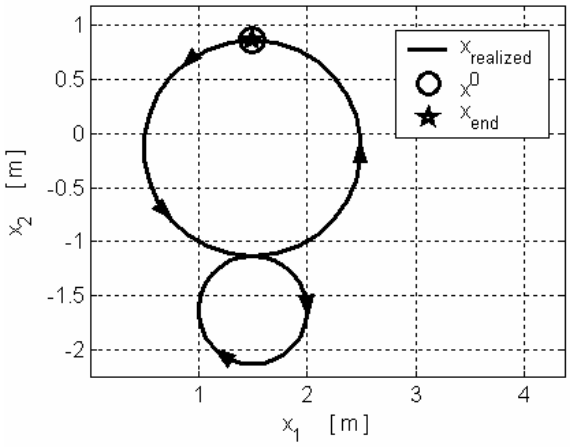

Figure 2.6 The ideal trajectory of the end effector in the repeatability test

The small circle is traversed only once in the simulation. This part of the trajectory is included to this test case to see the behavior of B-inverse when a non-consistent nodal joint angle set is used, as the same joint angle nodal values are used as before while the desired end effector trajectory is changed.

The simulation results using MP-inverse steering law are given in Figure 2.7 to Figure 2.9. The trajectory is realized very closely. The tracking error is given in Figure 2.7. The dynamics of the manipulator and the velocity of the end effector determine the tracking error in a position feed back control system. The lower circle is traced with a lower velocity, thus the tracking errors drops down to half amount at this portion of the simulation, illustrating the time dependency of the tracking error. The manipulability measure of the simulation is also given in Figure 2.8. The singularity measure is in a safe region where there is no singularity around and the tracking performance is acceptable.

The joint angles and velocities history, seen in Figure 2.9, proves that MP-inverse is not repeatable. The joints clearly do not follow a closed path; instead they seem converging to a limit joint cycle, as pointed out in [20]. In fact, for this trajectory, it reaches a repeatable scheme after 300 sec. (totally 10 cycles on the large circle), but this is a useless scheme since we do not have any control on it.

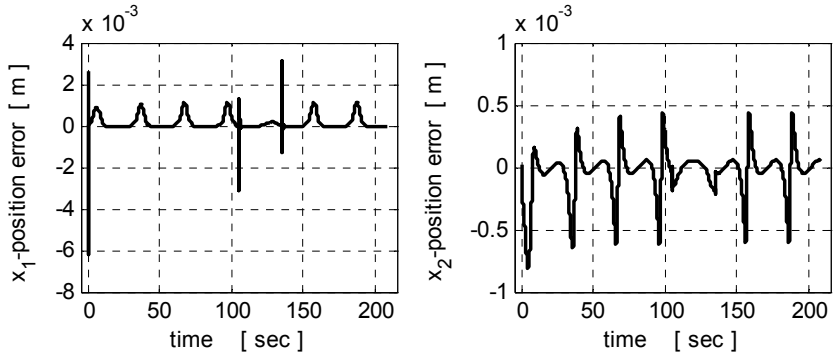

Figure 2.7 The tracking error of the end effector in MP-inverse repeatability test

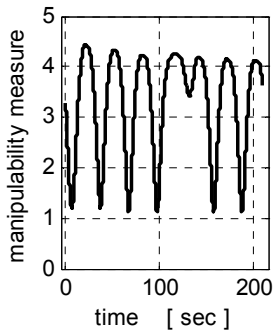

Figure 2.8 The manipulability measure of the manipulator in MP-inverse repeatability test

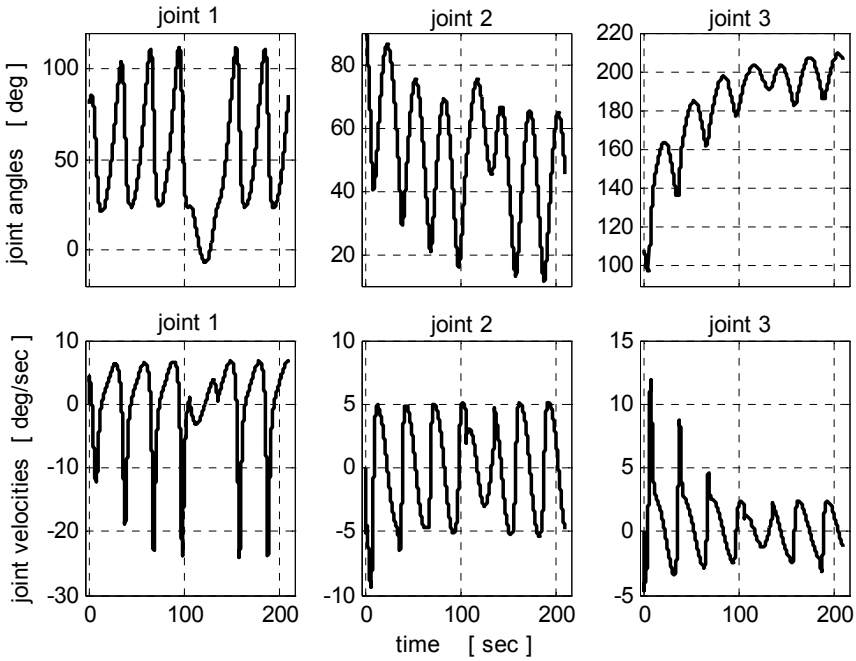

Figure 2.9 The time history of joint angles and velocities in MP-inverse repeatability test

The repeatability test is also run for B-inverse as the steering law. The selected nodes necessary to produce $\dot{\boldsymbol{\theta}}_{desired}$ for B-inverse are in TABLE 2.1. All of the nodes given in the table denote the same configuration at a specific point in the trajectory, as if the end effector would pass through that point in each period. This way, the nodes are used to guarantee repeatability. But for the time interval of $105 \le t \le 135 \text{sec}$, the path comes out to be different from the routine and the end

effector has to trace the lower circle. But the node at $t = 120\,\text{sec}$ is still the one for the routine cycle, so it becomes a false node. There is a conflict between the desired joint configuration and the path to be followed.

TABLE 2.1 List of nodal joint angle sets used by B-inverse in repeatability test

Node	Time [sec]	Joint 1 [deg]	Joint 2 [deg]	Joint 3 [deg]	x_1 position [m]	x_2 position [m]
1	30.0	60.0	120.0	60.0	1.50	0.866
2	60.0	60.0	120.0	60.0	1.50	0.866
3	90.0	60.0	120.0	60.0	1.50	0.866
4	120.0	60.0	120.0	60.0	1.50	0.866
5	150.0	60.0	120.0	60.0	1.50	0.866
6	180.0	60.0	120.0	60.0	1.50	0.866
7	210.0	60.0	120.0	60.0	1.50	0.866

Looking at the simulation results given in Figure 2.10 to Figure 2.12, B-inverse obviously generates closed paths in the joint space wherever available and this is a useful repeatability scheme that can be controlled by the user, since it is constructed using the nodes. At the time interval of $105\,\text{sec} < t < 135\,\text{sec}$, where the path is out of routine and there is the conflict, the end effector tracks the lower circle in a devoted manner without being effected from the false node. After that, it again catches the node at $t = 150\,\text{sec}$. Realize that, the path between the nodes of $t = 90\,\text{sec}$ and $t = 150\,\text{sec}$ is another closed path of eight shaped. As a result, this conflict between the desired track and the desired node does not bring out any tracking error or abnormal joint velocities to the system; the false node is simply neglected in the steering law, thanks to the blending property of B-inverse. Some configurations posed by the manipulator during this simulation is given in Figure 2.13.

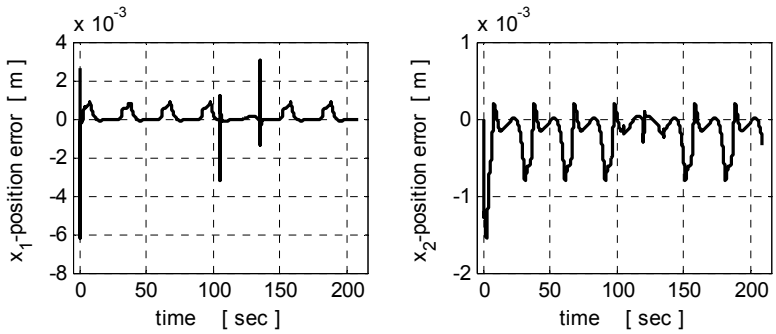

Figure 2.10 The tracking error of the end effector in B-inverse repeatability test

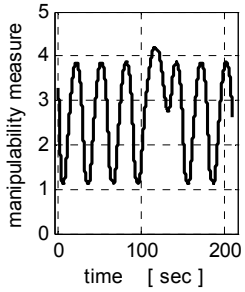

Figure 2.11 The manipulability measure of the manipulator in B-inverse repeatability test

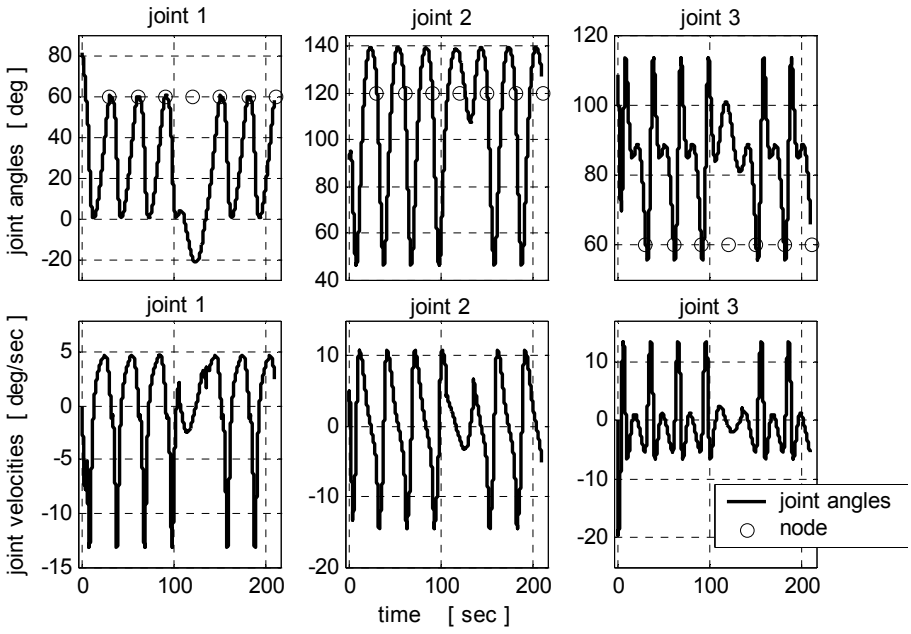

Figure 2.12 The time history of joint angles and velocities in B-inverse repeatability test

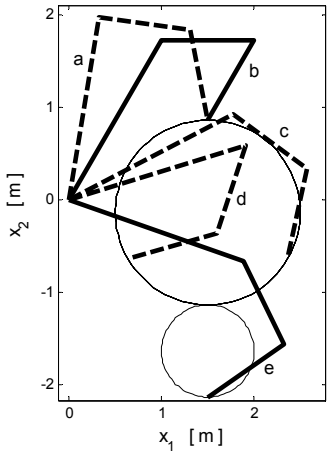

Figure 2.13 Some manipulator configurations from B-inverse repeatabilty test: **a.** initial configuration at t=0, **b.** nodal configuration at t = 30, 60, .., 210 sec., **c.** configuration at t = 40, 70,160 sec., **d.** configuration at t=50, 80 sec., **e.** configuration at t = 120.sec

2.4.2 Escapable Singularity Test

In this particular case, simulations are performed to demonstrate the singularity avoidance capability of B-inverse. For this purpose, a trajectory, on which the manipulator experiences an escapable singularity, is used. The singularity on the trajectory is demonstrated through MP-inverse steering law. Then, B-inverse is employed to avoid this singular configuration by using properly selected nodal joint angle configurations to drive the manipulator away from the singular solution.

The selected trajectory for the above demonstration is an arc shaped trajectory and mathematically defined as:

$$\begin{aligned} x_1 &= x_1^0 + 1 - \cos(\frac{\pi}{30}t) \\ x_2 &= x_2^0 + \sin(\frac{\pi}{30}t) \end{aligned} \qquad \text{for } 0 \le t \le 40\,\text{sec} \qquad (2.17)$$

The shape of this trajectory is given in Figure 2.14. If the initial position of the end effector is selected to be $(x_1^0, x_2^0) = (-3\,\text{m}, -1\,\text{m})$ and MP-inverse is used, then the system passes through the escapable singularity in 15 seconds, at the end effector position $\mathbf{x} = (-2\,\text{m}, 0\,\text{m})$. Notice that, for a redundant manipulator, the end effector position of an escapable singularity may also be satisfied by non-singular configurations. This singularity is encountered when a particular initial condition is used. To find that specific initial configuration, the test trajectory is simulated backwards, from the singular configuration, to the initial configuration. Since Eq. 2.5 is not defined at the singularity, the backwards simulation is initiated from the neighborhood of the singular configuration. Starting from this specific initial configuration, the test simulation using MP-inverse is conducted. The manipulator is going to pass very close to singular configuration with MP-inverse, so it is expected to have unacceptable tracking errors and joint velocities in the simulations.

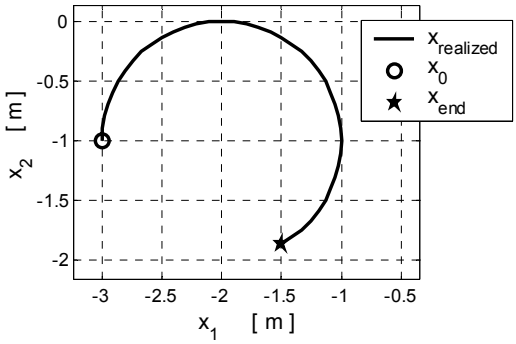

Figure 2.14 The ideal trajectory of the end effector in the escapable singularity test

The simulation results given in Figure 2.15 to Figure 2.18 shows that, the manipulator indeed comes very close to a singular configuration at $t = 15\,\text{sec}$, since the joint velocities display peaks up to the saturation limit of ±30 deg/sec (Figure 2.18). These unrealizable velocity demands also cause severe tracking

errors (Figure 2.14 and Figure 2.16). The approach to the singular configuration may also be observed from Figure 2.17 where manipulability measure goes down very close to zero.

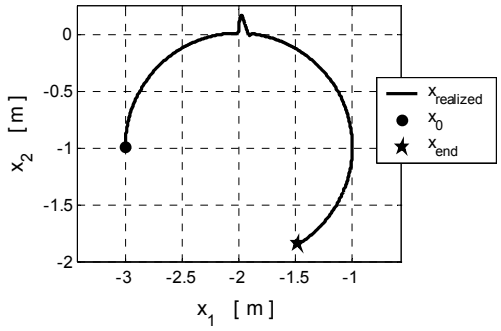

Figure 2.15 The trajectory realized by the end effector in escapable singularity test of MP-inverse

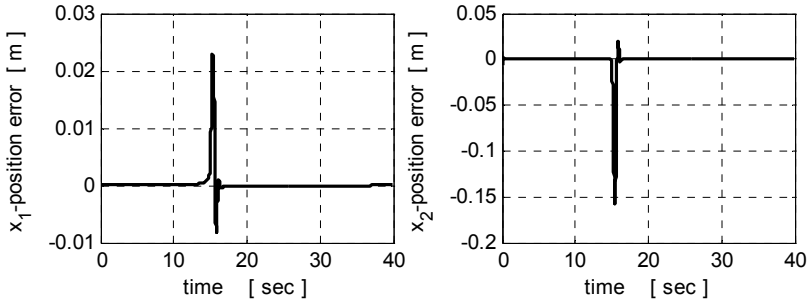

Figure 2.16 The tracking error of the end effector in escapable singularity test of MP-inverse

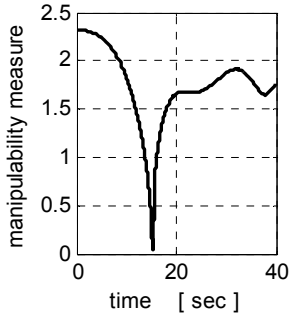

Figure 2.17 Manipulability measure in escapable singularity test of MP-inverse

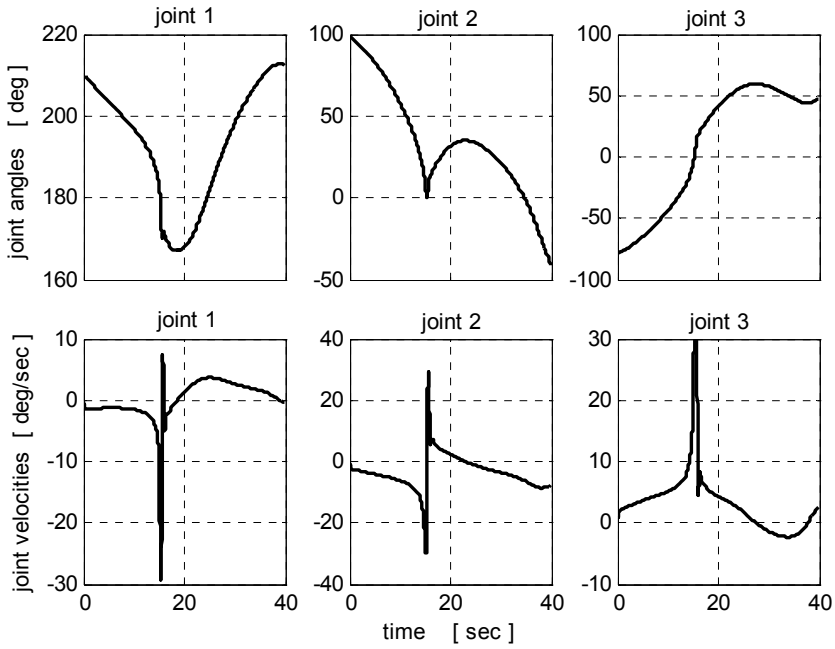

Figure 2.18 The time history of joint angles and velocities in escapable singularity test of MP-inverse

This situation is easily overcome when B-inverse is used. Since this is an escapable singularity, use of one randomly selected node, with a configuration far from the singularity is enough to create the necessary null motion to drive the system safely away from the singularity, without sacrificing the tracking performance at all. The node used for this purpose in this test case is given in TABLE 2.2. The simulation results obtained using B-inverse are given in Figure 2.19 to Figure 2.21. The manipulator finishes the task without coming close to singularity (Figure 2.20) and the tracking error is small while the joint velocities are smooth without any abrupt changes (Figure 2.21). Some joint configurations during those simulations are also given in Figure 2.22.

TABLE 2.2 List of nodes used by B-inverse in escapable singularity test

Node	Time [sec]	Joint 1 [deg]	Joint 2 [deg]	Joint 3 [deg]	x_1 position [m]	x_2 position [m]
1	40	272	121	-256	-1.50	-1.87

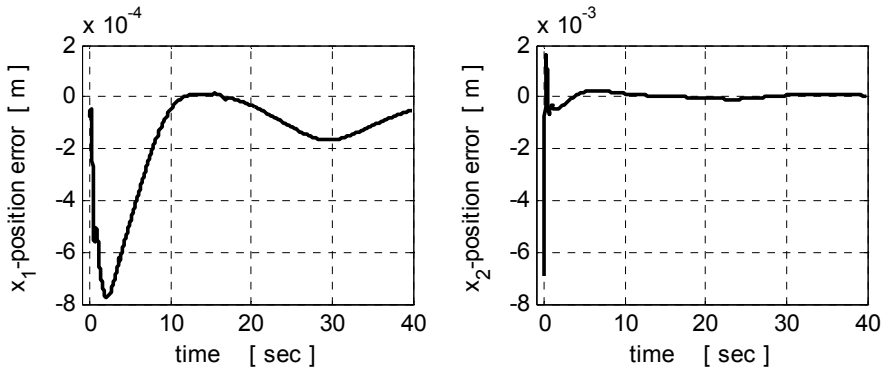

Figure 2.19 The tracking error of the end effector in escapable singularity test of B-inverse

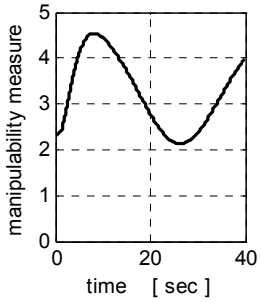

Figure 2.20 Manipulability measure in escapable singularity test of B-inverse

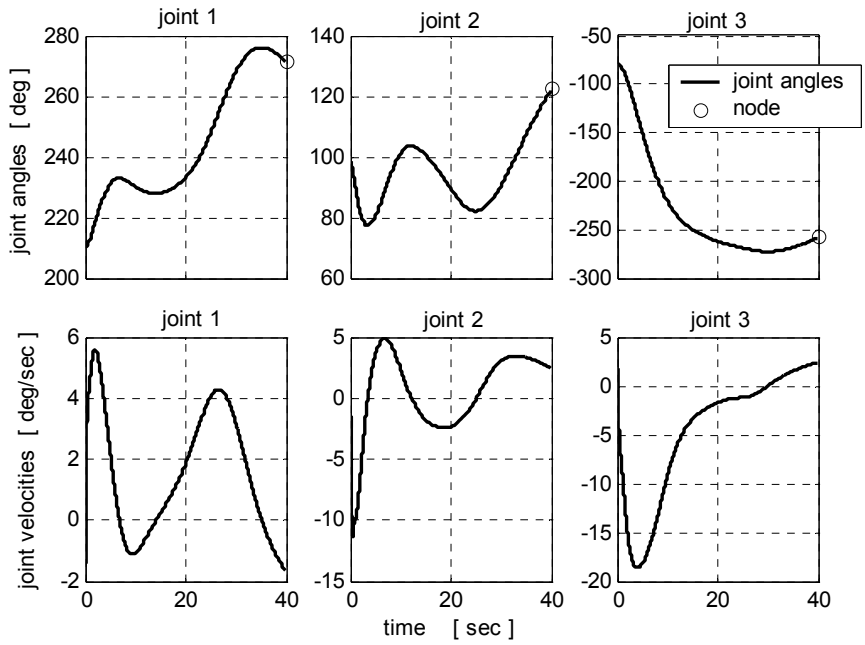

Figure 2.21 The time history of joint angles and velocities in escapable singularity test of B-inverse

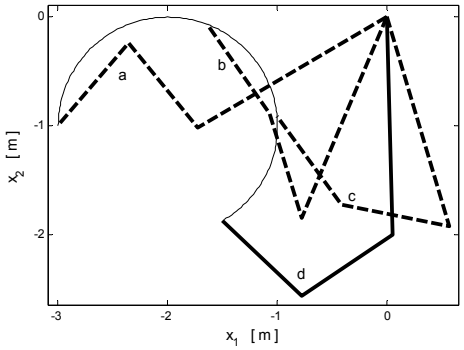

Figure 2.22 Manipulator configurations from the repeatabilty test of B-inverse:
a. initial configuration at t=0 sec, **b.** configuration at t = 20 sec., **c.** configuration at t = 30 sec., **d.** node configuration at t = 40 sec.

2.4.3 Inescapable Singularity Test

In this last test case, the singularity transition properties of B-inverse are demonstrated through an inescapable singular configuration. The end effector position that the manipulator falls into a singular configuration is selected as the

origin of the task space (base of the manipulator). For a manipulator with link lengths $l_1 = 2\,\text{m}, l_2 = 1\,\text{m}, l_3 = 1\,\text{m}$, this position requires a joint configuration of $[\theta_1 \quad 0° \quad 180°]$, which makes the first column of the Jacobian matrix given in Eq. 2.12 zero and decreases the rank to 1. This inescapable singular configuration is the configuration that is given in Figure 2.2 as an example to inescapable singularity. The configuration is singular for any value of θ_1. As seen in the figure, change in the base joint angle does not effect the end effector position indicating the existence of the null motion. However this null motion cannot get the manipulator out of the singular configuration.

The selected trajectory which passes through the origin, point $(0,0)$, at $t = 15\,\text{sec}$ is mathematically describe as:

$$\begin{aligned} x_1 &= x_1^0 - \sin(\frac{\pi}{30}t) \\ x_2 &= x_2^0 - 1 + \cos(\frac{\pi}{30}t) \end{aligned} \qquad \text{for } 0 \le t \le 30\,\text{sec} \tag{2.18}$$

The initial position of the end effector is $(x_1^0, x_2^0) = (1\,\text{m}, 1\,\text{m})$. The graphical representation of the trajectory is given in Figure 2.23.

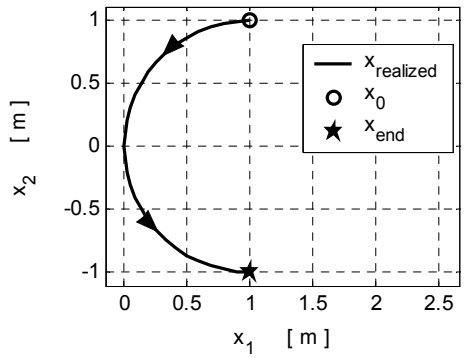

Figure 2.23 The ideal trajectory of the end effector in the inescapable singularity test

The simulation results using MP-inverse is given in Figure 2.24 to Figure 2.27. It may be observed from Figure 2.24 that the simulation stops before the end effector reaches the singularity position. This is because MP-inverse cannot provide a solution at singularity and in this case, there is no other possible configuration but the singular configuration that realizes the end effector position at $(0,0)$. As the manipulator comes close to the singularity, the tracking error given in Figure 2.25 and the joint velocities given in Figure 2.27 become unbounded. Also the manipulability measure goes to zero as seen in Figure 2.26.

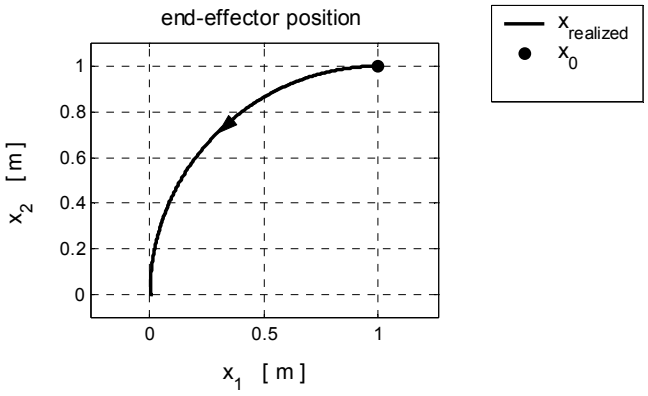

Figure 2.24 The trajectory realized by the end effector in inescapable singularity test of MP-inverse

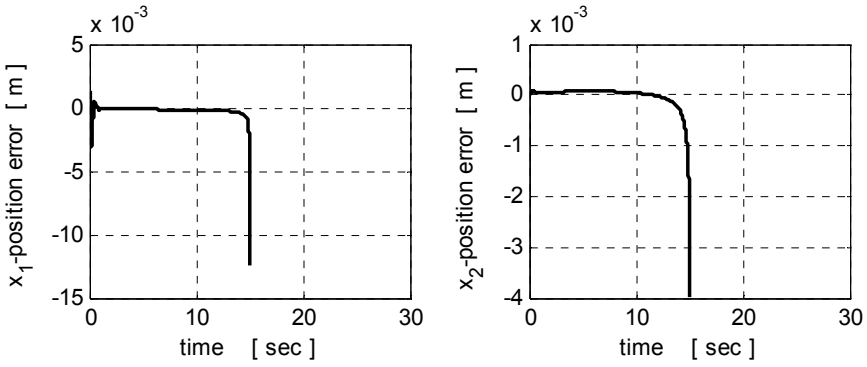

Figure 2.25 The tracking error of the end effector in inescapable singularity test of MP-inverse

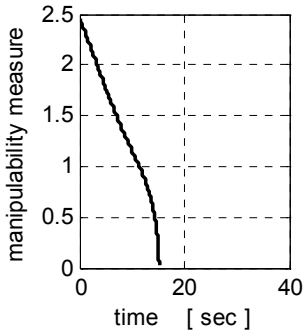

Figure 2.26 Manipulability measure in inescapable singularity test of MP-inverse

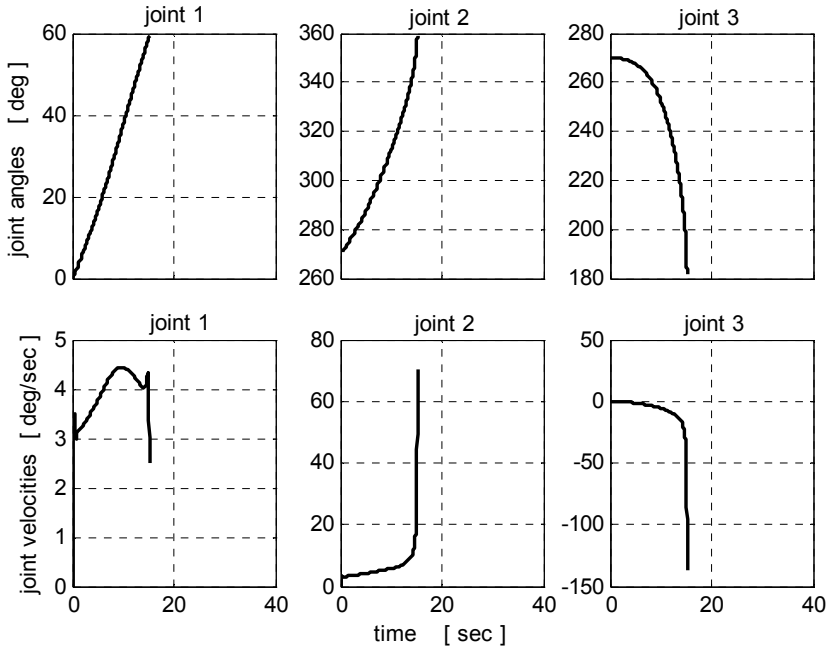

Figure 2.27 The time history of joint angles and velocities in inescapable singularity test of MP-inverse

Three nodes are selected for B-inverse simulations. The list of the selected nodes is presented in TABLE 2.3. The results of the simulation are given in Figure 2.28 to Figure 2.30. Equipped with the secondary task, $\dot{\boldsymbol{\theta}}_{desired}$, which is concurrent with the trajectory following task, B-inverse provides a smooth and accurate transition through the singular configuration. The trajectory is traced very closely as given in Figure 2.23. The tracking error during the simulation is given in Figure 2.28. The

manipulability measure in Figure 2.29 shows the transition through the singularity. There is no delay or any disturbance seen on the graph. The manipulator passes through the singularity, at which manipulability measure is zero, as another ordinary point. The joint angles and velocities are presented in Figure 2.30. Very smooth joint angles histories and joint velocities with reasonable jumps around nodes are most significant observations in those graphs indicating a successful transition through an inescapable singularity. Some joint configurations of the manipulators at the indicated instants during the simulations of B-inverse are also presented in Figure 2.31.

TABLE 2.3 List of nodes used by B-inverse in inescapable singularity test

Node	Time [sec]	Joint 1 [deg]	Joint 2 [deg]	Joint 3 [deg]	x_1 position [m]	x_2 position [m]
1	8	13	308	243	0.257	0.669
2	16	-4	368.5	168.5	0.005	-0.105
3	30	0	450	90	1.0	-1.0

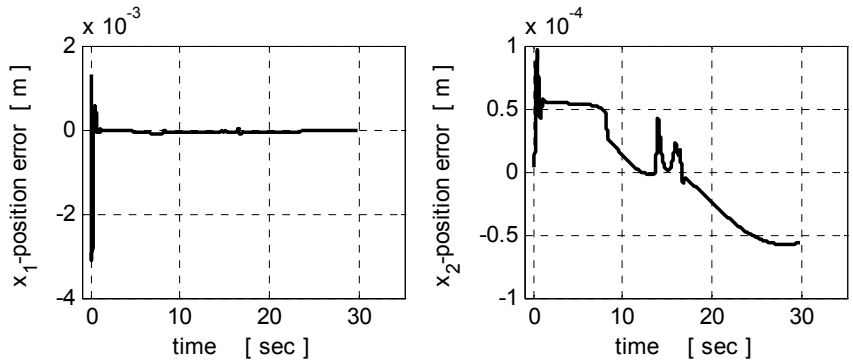

Figure 2.28 The tracking error of the end effector in inescapable singularity test of B-inverse

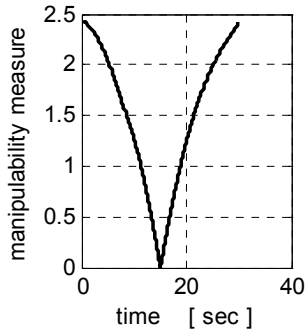

Figure 2.29 Manipulability measure in inescapable singularity test of B-inverse

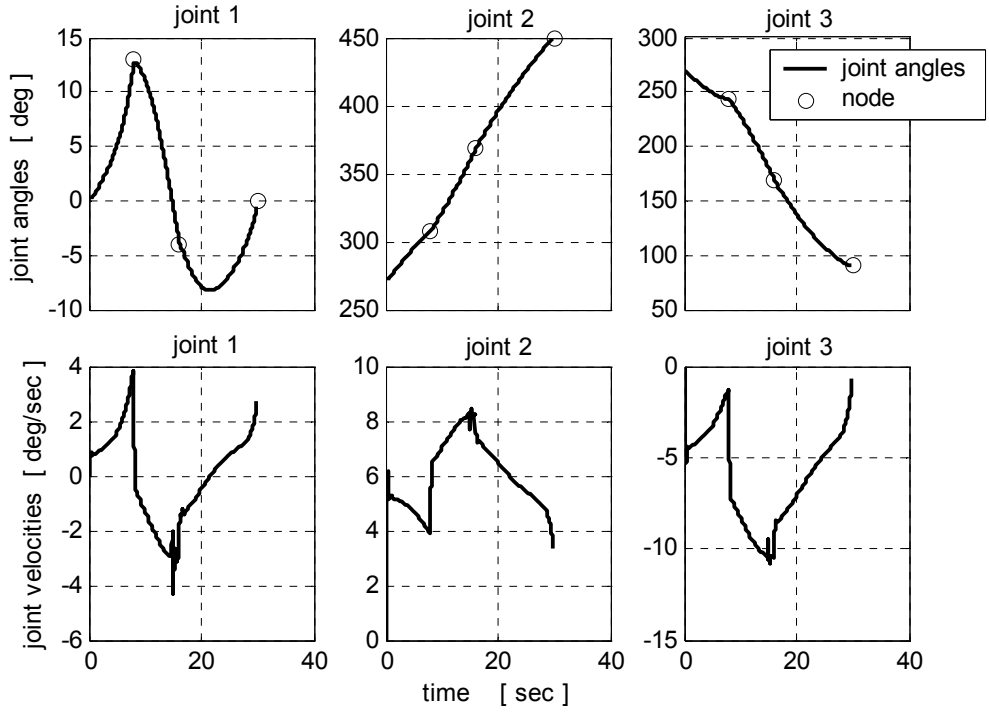

Figure 2.30 The time history of joint angles and velocities in inescapable singularity test of B-inverse

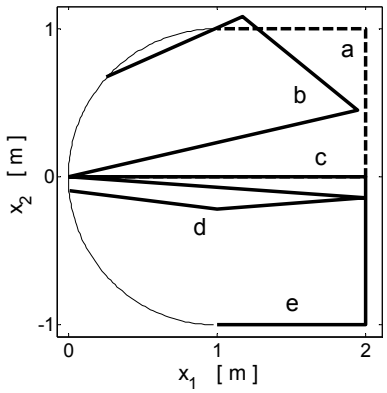

Figure 2.31 Some manipulator configurations from the inescapable sing. test of B-inverse. **a.** initial configuration at t=0 sec, **b.** node configuration at t = 8 sec., **c.** singular configuration at t = 15 sec., **d.** node configuration at t = 16 sec., **e.** node configuration at t=30 sec.

CHAPTER 3

ENERGY STORAGE AND ATTITUDE CONTROL IN SPACECRAFT SYSTEMS

3.1 Introduction

Energy storage and attitude control are two critical functions that has direct bearing on the success of a space mission. This chapter examines these functions and presents the systems performing these functions. The chapter begins with an introductory discussion on the attitude control and energy storage systems respectively and the devices that perform these operations in today's spacecrafts. Next, an integrated subsystem that combines these two functions in the spacecraft, known as Integrated Power and Attitude Control System (IPACS), is considered as an alternative to the conventionally used systems. This system is discussed in detail and comparisons with the commonly used alternatives are presented.

3.2 Spacecraft Attitude Control

In a spacecraft, attitude control function is a part of the attitude determination and control subsystem. This subsystem measures and controls the spacecraft's orientation in space. A block diagram of the spacecraft attitude determination and control subsystem is given in Figure 3.1.

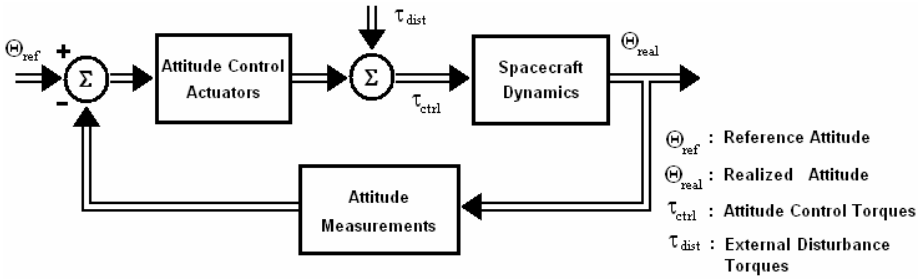

Figure 3.1 General block diagram of a typical attitude determination and control system

The attitude measurements in a spacecraft are commonly performed by two kinds of attitude sensors. The reference sensors gather the orientation information by locating the well-known bodies in space, like earth, sun or stars. Earth horizon sensors, sun sensors and star trackers are such reference sensors. The second type of attitude sensors is gyroscope. In most space applications, groups of different types of sensors are used in combination and the information gathered are fused by statistical techniques, like Kalman filtering, in order to obtain highly accurate attitude measurements throughout the mission [47,48].

The attitude control actuators produce the necessary control torques to provide the spacecraft the desired attitude in the existence of internal and external disturbance torques.

Attitude control through gravity gradient, magnetic field alignment or spin stabilization techniques are the basic methods for passive attitude control. Passive control techniques are usually low cost and provide a stable attitude to the spacecraft with a very limited maneuverability. They also have high lifetimes compared with other subsystems of the spacecraft [48].

Active attitude control, on the other hand, is the control technique that is more common than the passive techniques in today's technology. Current space missions, demanding high maneuvering capabilities, require spacecraft that is

controlled in all directions. They also require high pointing accuracy and agility. TABLE 3.1 lists attitude control methods along with typical characteristics of each. As it may be observed from the table, agility and pointing accuracy requires active control with momentum exchange devices (MED).

TABLE 3.1 Attitude Control Methods and Their Capabilities [39,47,48]

Type	Pointing Options	Attitude Maneuverability	Typical Accuracy	Lifetime Limits
Gravity Gradient	Earth local vertical only	Very Limited	± 5º (two axes)	None
Passive Magnetic	North/South only	Very Limited	± 5º (two axes)	None
Spin Stabilization	Inertially fixed any direction (Repoint with precession maneuvers)	High propellant usage to move stiff momentum vector	± 0.1º to ± 1º in two axes (proportional to spin rate)	Thruster propellant (if applies)
3-Axis Active Control (with momentum exchange devices)	No Constraints	No constraints (High rates possible)	± 0.001º to ± 1º (in all three axes)	Propellant (if applies), Life of wheel bearings

In general different types of attitude control actuators are usually used together. Typically, a MED, which may be a momentum wheel, a reaction wheel or a control moment gyroscope, is used with a thruster or a magnetic torquer to obtain the active control ability in one direction. For a 3-axis active attitude control, these actuators are employed in redundant clusters such that each actuator cluster could produce torques of their own in any direction in space. All these actuators are briefly mentioned below.

3.2.1 Momentum Exchange Devices

A MED basically consists of a system that is able to store angular momentum in a flywheel that spins around its central axis. It produces the necessary control torque by changing the angular momentum vector of its flywheel by either

accelerating/decelerating it or rotating it in an axis other than the spin axis. In this manner, a transfer of angular momentum takes place between the spacecraft and the actuator system. These systems are called as momentum exchange devices owing to this internal momentum transfer. They absorb and store the undesired external disturbance torques applied on the spacecraft through a feedback control, to provide a smooth and precise orientation for the spacecraft. Also they change the angular momentum of the spacecraft in a controlled manner, to make the spacecraft perform the required maneuvers accurately in space.

Reaction wheels are essentially torque motors with high-inertia rotors [39]. They can spin in either direction and provide one axis of control for each wheel. Momentum wheels are reaction wheels with a nominal spin rate above zero to provide a nearly constant angular momentum. This momentum provides gyroscopic stiffness to two axes, while the motor torque may be controlled to precisely point around the third axis. A typical reaction wheel is seen in Figure 3.2

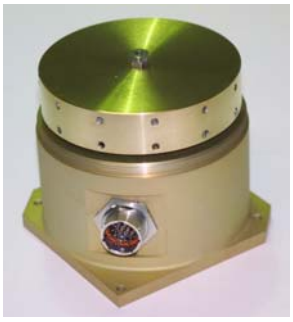

Figure 3.2 A reaction wheel (from [40])

For applications where high torques are required, control moment gyroscopes (CMG) are used instead of reaction or momentum wheels. They also have a wheel spinning at constant speed. But this wheel is gimbaled in at least one axis that is perpendicular to the spin axis of the flywheel. A CMG that is gimbaled along a single axis is called as a Single Gimbal CMG (SGCMG), while a Double Gimbal

CMG (DGCMG) is the one that is gimbaled in two axes. Mechanical and electrical construction of DGCMGs are much more complex than SGCMGs, making them to be less popular than SGCMGs [51]. Throughout this text, only SGCMGs will be considered and they will be referred with the abbreviation CMG. Figure 3.3 shows a cluster of CMGs mounted on a test bed.

By turning the spinning flywheel of a CMG around its gimbal axis, high output torque may be obtained whose size depends on the angular momentum of the spinning flywheel and the rate of rotation of the gimbal. In addition to their mechanical complexity, CMGs also have theoretical control problems with respect to the reaction wheels. However, their large torque amplification capabilities and high momentum storage abilities with limited mass make these actuators very promising for future space applications [43].

Figure 3.3 CMGs installed on a ground test bed (from [16])

The main drawback of the MEDs comes from the fact that they can only produce internal control torques and cannot change the total angular momentum of the spacecraft. The absorbed external torques accumulate on the MED up to its storage limit (momentum buildup), making it impossible to produce torque in a particular direction. This phenomenon is called saturation, which reduces the attitude control

capability of the spacecraft. To dump the excessive momentum, other actuators, such as thrusters or magnetic torquers, which can produce controlled external torques are used in combination with the MEDs [48].

3.2.2 Thrusters

Thrusters produce forces by expelling gas that is accelerated by the energy of the chemical reaction or a latent heat of a phase change occurred in the thruster [9]. A typical thruster is shown in Figure 3.4. Torque is produced by the use of two thrusters in opposite directions. The thruster torques may be quite large due to the amount and type of the propellant used. The thrusters are considered in two types as hot gas and cold gas thrusters. The inherent discontinuity present in their torque production, their torque profiles are not as smooth as the torques generated by the MEDs. They are used in applications with moderately low attitude accuracy requirements, such as large angle attitude maneuvers, orbit adjustments and MED momentum dumping operations.

Figure 3.4 A thruster for use in space applications (from [11])

3.2.3 Magnetic Torquers

Magnetic torquers are commonly used actuation devices in satellite missions. These torquers use a magnetic coil that is energized with electrical current to generate the required electromagnetic dipole moment [39]. In the presence of the geomagnetic field, this dipole moment produces a torque that is always proportional and perpendicular to the geomagnetic field. Since the amount of their torque is dependent on the strength of the geomagnetic field, these torquers are most efficiently used in low-Earth orbits (LEO) where geomagnetic field is relatively strong. The magnetic coils may be wound on an electromagnetic rod, usually made up of ferromagnetic material, to obtain a media with high magnetic permeability inside the coil. These devices are called magnetic torque rods. Having no moving parts, complex electronics and expendables, magnetic torquers are the most reliable attitude control actuators without any lifetime limit. An image of a typical magnetic torque rod is given in Figure 3.5.

Figure 3.5 A typical magnetic torque rod (from [29])

The typical properties of the actuators that are briefly presented above are listed in TABLE 3.2.

TABLE 3.2 Actuators Used in Spacecraft Attitude Control [9,39,47,48]

Actuator	Typical Performance Range	Weight (kg)	Power (Watt)	Advantages	Disadvantages
Reaction / Momentum Wheels	Max torque 0.01 – 1 N.m	2 – 20	10 – 100	Smooth and precise	Need desaturation
Control Moment Gyroscopes	1 – 500 N.m	2 – 40	10 – 150	Smooth, precise, high torque	Complex, expensive, need desaturation
Thrusters (Cold Gas)	< 5 N	Depends on propellant amount	N/A	Simple, precise	Need propellant
Thrusters (Hot Gas)	0.5 – 9000 N	Depends on propellant amount	N/A	Simple, high torque	Need propellant
Magnetic Torquers	10^{-4} – 0.2 Nm	0.4 – 50	0.6 – 16	Simple, reliable, no propellant	Small torque, geomagnetic field dependent

3.3 Energy Storage in Spacecraft Systems

Energy storage is an integral part of the spacecraft's electrical power subsystem, whose block diagram is presented in Figure 3.6. In a spacecraft, energy storage is required mainly for two reasons. First reason is that the power supply system of a spacecraft is designed to handle the nominal power regimes of the space mission and backup is needed for the periods of peak power demands that the power supply system cannot deliver by itself. Secondly, an energy backup is required for the periods in which energy cannot be extracted from the regular power resources.

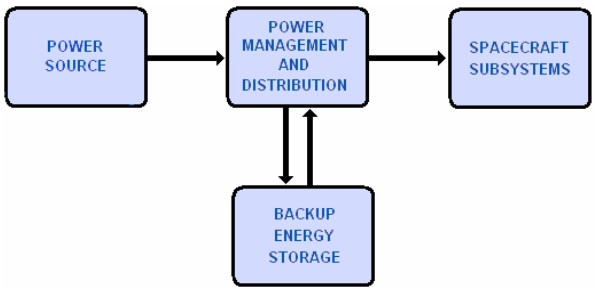

Figure 3.6 General block diagram of a spacecraft electrical power subsystem

As an example, for any spacecraft that utilizes solar panels to generate electricity, stored energy is required in the eclipse periods. In addition, the solar panels are generally sized to handle nominal power loads. Thus, when the spacecraft is in the eclipse or when peak powers are needed, the required additional energy is drawn from the storage units.

3.3.1 Electrochemical Batteries

In space applications, energy is usually stored in the form of chemical energy in electrochemical batteries. These batteries are either primary or secondary. Primary batteries convert the chemical energy into electrical energy but cannot reverse this conversion, so they cannot be recharged and are used only for once. Their limited capability brings them very limited usage. They are employed in very short durations or very long-term tasks that use very little power. Secondary batteries, on the other hand, are rechargeable electrochemical batteries that can repeat charge/discharge process for thousands of cycles. A secondary battery provides power during any power shortage and can also level the power loads. They are charged with the excess amount of energy obtained from the main power source when possible, and then discharged when energy is required. They are widely used in today's space missions [47].

Considering the secondary batteries, the spacecraft's orbital parameters, especially altitude, determine the number of charge/discharge cycles that the batteries have to support during the mission life. In Earth orbiting missions, for instance, the batteries of a spacecraft on a geosynchronous orbit (GEO) needs to store energy for two long eclipse periods of 45 days per year, with eclipses occurring around one hour every day in this period. On the other hand, a spacecraft in LEO experiences around 35 minutes of eclipse in each orbital period of 95 minutes.

The lifetime of rechargeable batteries is given in terms of cycle life instead of time. A battery's capability of storing energy is specified by its specific energy, the amount of energy stored in unit mass or energy density, the amount of energy stored in unit volume. Another important concept concerning the rechargeable batteries is the depth of discharge (DOD). DOD is simply the percent of total battery capacity removed during a discharge period. The importance of DOD comes from its relation with the cycle life. If a battery is discharged in higher percentages, implying a high DOD, its cycle life gets shorter. The relationship is shown in Figure 3.7 for different battery types and manufacturers.

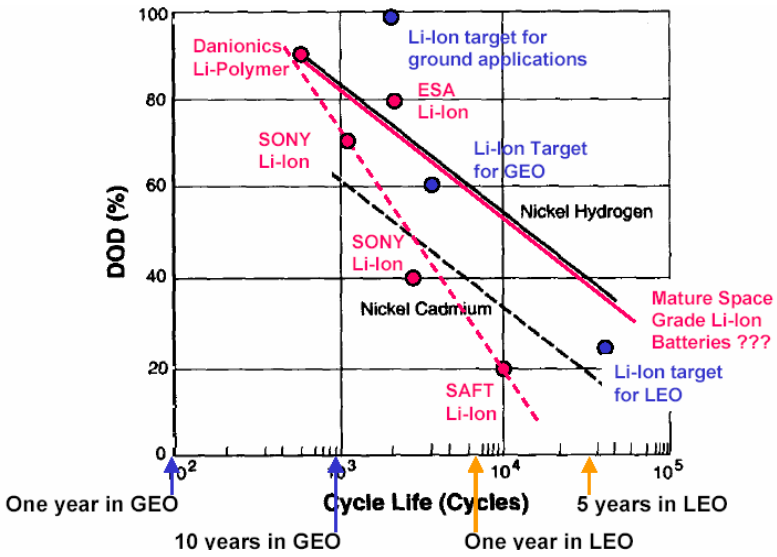

Figure 3.7 DOD vs. Cycle Life relation for different battery chemistries and manufacturers (from [15])

As seen in Figure 3.7, there are different types of electrochemical batteries named according to their chemical compositions. These different batteries have different characteristics, which make them more suitable for different specific missions. The most popular battery types for space applications are Nickel-Cadmium (Ni-Cd), Nickel Hydrogen (NiH_2), Nickel Metal Hydride (NiMH) and Lithium Ion (Li-Ion) batteries. The basic properties of these battery types are tabulated in TABLE 3.3.

TABLE 3.3 Electrochemical Battery Properties [15,17,25,27,46]

Battery	Energy Density (*Wh/kg*)	Advantages	Disadvantages
Ni – Cd	30 – 60	Proven technology with extensive database, low cost	Low DOD and Specific Energy, Memory effect
NiH_2	25 – 60	Higher DOD with respect to Ni – Cd	Low Energy Density (voluminous), suitable for large satellites
NiMH	60 – 80	Highest specific energy and energy density in Ni-based batteries	Insufficient Cycle Life, Complex Charging
Li – Ion	100 – 130	High energy density, no memory effect at all	Intolerant, fragile technology, not space rated yet

Ni-Cd is a well-established chemistry with an extensive flight heritage. They can take a fast charge and are capable of thousands of cycles. On the other hand, this chemistry has reached its energy density limit and does not seem to improve any further. Moreover, they suffer from the so-called "memory effect". The term memory effect implies that the battery "remembers" the amount of energy drawn from the previous discharges and after a number of charge/discharge cycles of the similar DOD, the battery cannot be discharged for a larger DOD [25].

Figure 3.8 Eagle Picher Ni – Cd Cells (from [15])

NiH_2 has intrigued the space community because it appears to be better than Ni-Cd for long term applications. It allows better DOD percentages with respect to Ni-Cd for the same cycle life. They have been qualified on GEO missions but there is not enough data about their LEO performance with a large number of charge/discharge cycles. Due to the H_2 gas included in the chemistry, battery cells are contained in a pressure vessel (See Figure 3.9). This decreases the energy density of the batteries and makes their use impractical, especially for small spacecrafts with limited volume [47].

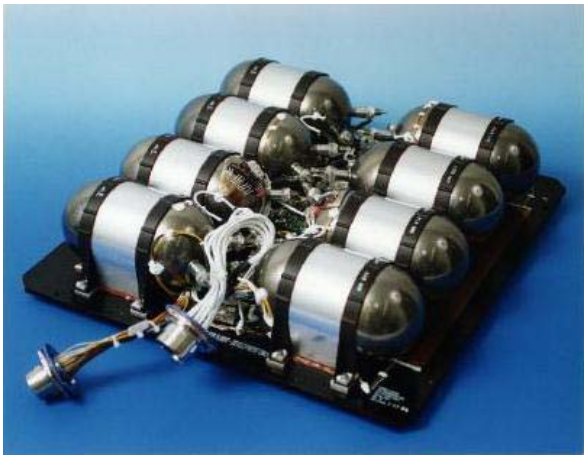

Figure 3.9 NiH_2 battery pack (from [31])

NiMH cells have gained popularity since the late 1980s. Steady increase in their performance have made this chemistry considerable in space applications also. Among the advantages of NiMH are: 30% to 40% more capacity than a NiCd cell the same size, less prone to memory effect than NiCd, and competitively priced (especially compared to lithium-ion). In NiMH battery cells, the hydrogen is not stored under pressure as in the case of NiH_2, but it is stored in a hydrogen-absorbing alloy. NiMH, however, does also have some down sides. NiMHs only yield about 500 cycles, which would be insufficient for LEO applications. Its charging is more complex than NiCd and NiMH loses its charge about twice as fast as NiCd [47].

Li-ion is a delicate technology in production since 1991 that offers increased performance over nickel based chemistries [3,17]. Li-ion has twice the energy density of NiCd, is capable of fairly high discharge currents, and has relatively low self-discharge. Also they are completely free of memory effect. Li-Ion is still a promising technology and is under constant improvement. This constant progress can also be followed from the terrestrial applications. The Li-Ion batteries of mobile phones and laptop computers are still getting smaller and smaller whereas the amounts of energy stored in these battery packs keep increasing. The drawbacks of Li-Ion batteries are that they are very expensive and they need complex control circuits to manage their charging conditions. They are intolerant to overcharge conditions. Also, although it founds many applications in our daily lives for more than a decade, it is still a very young technology with a narrow database, which has not fully proven itself in space applications yet [15,17]. Li-Ion battery cells packed for use in space is shown in Figure 3.10.

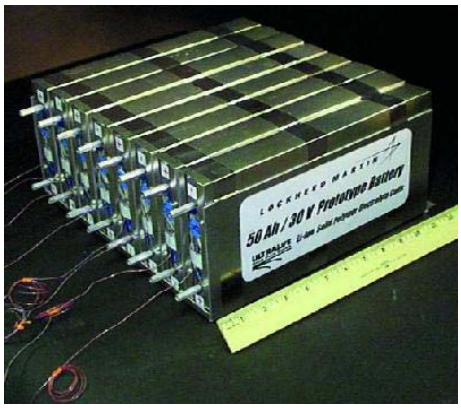

Figure 3.10 Li-Ion battery pack (from [31])

3.3.2 Mechanical Batteries

In spite of being the traditional way of energy storage with a considerably high flight heritage in space, many drawbacks inherent to the electrochemical battery technologies cause dissatisfaction and encourage the search for alternative energy

storage methods. One of these methods is the flywheel energy storage, which is also known as mechanical battery [8]. In mechanical battery concept, the energy is stored in the rotating flywheel in the form of kinetic energy. This is a fairly old and simple idea that has already been in use in many engineering applications. For example, it has been in use in internal combustion engines to smooth their operations. The mechanical batteries have become competitive to electrochemical batteries after the technological improvements in power-conversion electronics, composite materials and magnetic bearings [44]. With these improvements, flywheels may be constructed as efficient and feasible systems to store energy with high specific energies. Flywheels offer numerous advantages for energy storage over electrochemical batteries, some of which are listed in TABLE 3.4.

TABLE 3.4 Improvements of Mechanical Batteries [3]

Electrochemical Batteries	**Mechanical Batteries**
• Capacity fade over life	• No capacity fade over life
• Difficulty in determining the charge status	• Deterministic state-of charge
• 75% round trip efficiency	• 85-95% round trip efficiency
• Overcharging problems	• Overcharging is handled easily
• Charge/Discharge rate limitations	• Much higher rates are achievable
• Coupled energy storage and power capacities	• Energy storage and power capacity are not coupled

As a result of the technological advancements leading to these advantages over electrochemical batteries, the flywheel energy storage systems have already been marketed for ground-based applications. A catalog page of a flywheel energy storage system that is in the market as a UPS is given in Figure 3.11 as an example. They are also considered for use in trains and busses to store the brake energy instead of dissipating it. They will supply the peak power requirements of these vehicles with this stored energy. Experimental prototypes of such so-called

hybrid vehicles have already been built. They are also heavily being considered for the space applications, due to their superiorities over electrochemical batteries [2, 8, 12, 18, 19, 32, 41, 44]. An example to a flywheel energy storage system that is being tested for use in space is given in Figure 3.12. In this thesis work, flywheel energy storage system to be used in spacecraft, as a part of Integrated Power and Attitude Control System, is addressed.

3.4 Integrated Power and Attitude Control System

Like for many other functions of the spacecrafts, for the above-mentioned functions of energy storage and attitude control, there is always a search for the devices that are more capable and less demanding. Devices that perform more than one functions for the spacecraft may sometimes provide better solutions due to the synergy obtained by that combination. Integrated Power and Attitude Control System (IPACS) is one such system that combines the energy storage and attitude control functions of the spacecrafts. These two functions are combined through the concept of mechanical batteries. The rotating flywheels of the momentum exchange devices used in the spacecraft attitude control systems as actuators should also be used to store the energy [4]. A single device performs two different functions in this case. In this way, the mechanical batteries that increase the power subsystem capabilities of the spacecrafts, having many advantages over the traditional electrochemical batteries as pointed out in the previous section, are used in space systems in a wise manner. Substantial weight saving are also possible with the dual usage of a single device. The benefits that IPACS provides to the spacecrafts are listed in TABLE 3.5 [8].

CleanSource DC
BATTERY-FREE ENERGY STORAGE

100 to 2000 kW DC

System Features

- High Reliability
- High Power Density
- Small Footprint
- ~99% Efficient
- Low Maintenance
- Environmentally Friendly
- Microprocessor Based
- Self-Diagnostics
- LCD Control Panel
- Fast Recharge-150 sec
- Soft-start UPS Integration
- Programmable Voltage Settings
- Programmable I/O Contacts
- Quite Operation
- Long Useful Life
- Simple Installation
- No Special Wiring Required
- Compatibility Testing with multiple UPS brands

Optional Features

- Front Panel DC Disconnect
- Parallel up to 2000-kW
- Monitoring Software
- Remote Notification (Email & Pager)
- Remote Monitoring (Network, and/or Modem)
- Ethernet
- SNMP & MODBUS Protocols
- Top/Bottom Entry
- N+1 Configurable
- Seismic Installation

DC Flywheel Energy Storage System

Ultimate Backup Power for UPS Systems

From industrial plants where maximum productivity is crucial, to the worldwide build-out of advanced data centers, power quality is essential to keep businesses online and fully operational. Active Power's CleanSource® DC battery-free technology is an integrated flywheel motor-generator that stores kinetic energy in its constantly spinning, quiet, low-friction steel disc. Stored energy from the flywheel is instantly converted to electricity that bridges the power for critical loads during utility disturbances, and acts as an effective supplement or replacement for chemical energy storage with UPS systems. Compared to batteries, CleanSource DC dramatically reduces space requirements, temperature restrictions, replacement cycles and maintenance while improving UPS system reliability and operational integrity.

Dual flywheel energy storage system pictured

Active Power®

QUALITY POWER FOR A DIGITAL WORLD™

Figure 3.11 A catalog page of a marketed flywheel energy storage system. (From [1])

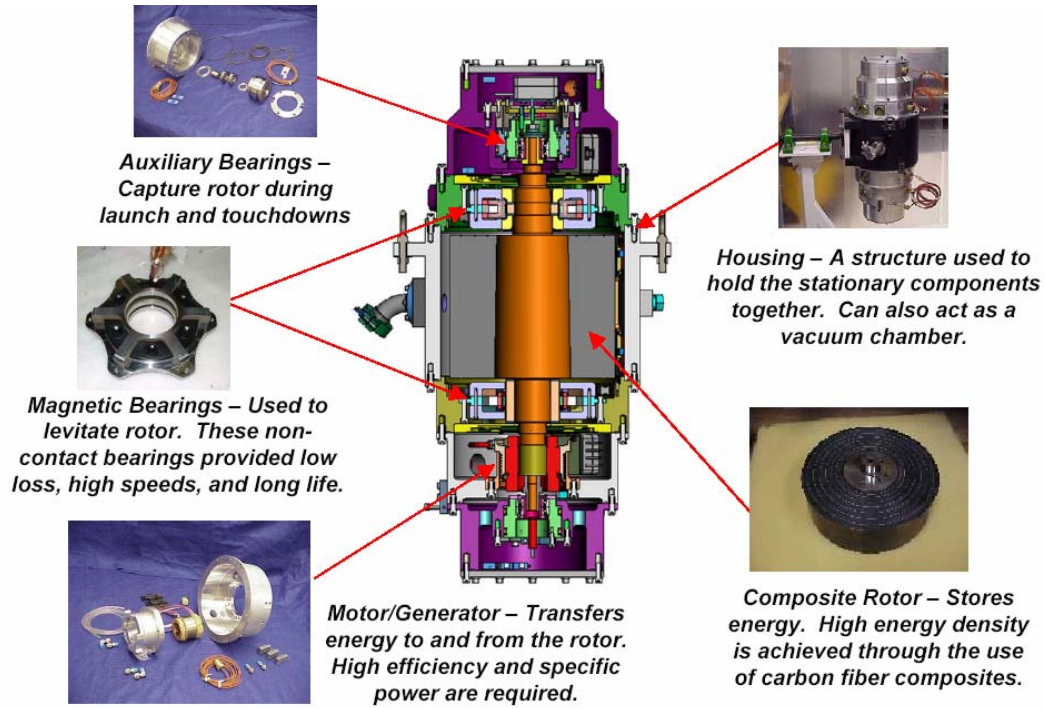

Figure 3.12 A Flywheel with major parts explained (from [28])

TABLE 3.5 Energy Storage and Attitude Control Function Benefits of IPACS [8]

Energy Storage Advantages	Resulting Benefits
• 5-10+ times greater specific energy • Long life (15 yrs.) unaffected by number of charge/discharge cycles • 85-95% round trip efficiency • High charge/discharge rates & no trickle charge required • Deterministic state-of-charge • Inherent bus regulation and power shunt capability	• Lower mass • Reduced logistics, maintenance, life cycle costs and enhanced vehicle integration • More useable power, lower thermal loads • Peak load capability, 5 – 10 % smaller solar array • Improved operability • Fewer regulators needed, e.g., could eliminate solar array shunt regulator
Attitude Control Advantages	**Resulting Benefits**
• Long life • Large control torques • Large momentum storage capability • Magnetic bearing suspension reduces vibration	• Reduced logistics, maintenance and life cycle costs • Reduced propellant needs (wheels can now handle requirements that previously demanded propulsion systems) • Improved sensor payload performance and micro gravity environment

In IPACS, the rotating flywheels that performs both the energy storage and attitude control functions may be utilized either as momentum wheels or they may be gimbaled just like control moment gyros. The momentum wheel type IPACS are to display substantial amount of coupling effects between power and attitude control subsystems, due to the dual usage. The torque generation and energy storage operations are both performed by changing the spin rate of the rotating flywheel. In the latter case, however, this coupling effect is inherently at minimum. That's because the torque generation is realized by simply changing the direction of the angular momentum vector in a CMG. As a result, the energy content of a CMG cluster remains unaffected by the attitude control operations. Since energy storage and attitude control are performed in different axes that are perpendicular to each other, the coupling effects between attitude control and energy storage functions are less with respect to IPAC with momentum wheels [3,12,44,53].

Utilizing a CMG in an IPACS application, it is possible to perform both of these functions simultaneously. Such a CMG that can store energy in its variable speed flywheel is called an IPAC-CMG. A motor/generator unit attached to the spin axis of the flywheel would control the energy storage and generation operations on this variable speed flywheel.

Although an IPAC-CMG is practically a variant of a CMG, the variable spin rate of the flywheel of an IPAC-CMG would cause two important differences that are to be considered before progressing any further. First, as the magnitude of the angular momentum vector of an IPAC-CMG changes due to the variations in the spin rate of its flywheel, undesired torques are produced in the flywheel spin axis direction. In an IPAC-CMG cluster, these undesired torques produced by each IPAC-CMG unit should be balanced so that the total angular momentum vector of the cluster shall be made to have the desired magnitude and direction continuously. In other words, the effect of the energy storage on attitude control shall be eliminated [3].

Fortunately, these undesired torques originated from the energy storage operations are to be harmonic in nature, since a storage operation should be followed by a generation operation in a time period. For instance, in a LEO spacecraft, IPAC-CMGs would spin up in the sun light for about 60 minutes and then would spin down when the spacecraft is in the eclipse, which lasts for about 35 minutes. This process repeats itself in the next orbital period of the spacecraft. So the torques due to these accelerations and decelerations do not create any momentum accumulation in an IPAC-CMG cluster in the long term. In addition, they are small in magnitude with respect to the torques required for the slew maneuvers of a typical small spacecraft. The magnitude of these power torques and their ratio to the typical attitude control torques are revealed in the simulations results presented in the coming chapters.

Assuming that the total angular momentum vector of the IPAC-CMG cluster is not affected by the energy storage operations, the second difference that the variable spin rate of the IPAC-CMG flywheel causes can be discussed. As the flywheels of an IPAC-CMG cluster accelerates and decelerates, the angular momentum storage capacity of the cluster increases and decreases respectively. Here, the constant total angular momentum vector shall be strictly smaller than the minimum momentum storage capacity at all the times. Otherwise, the total angular momentum vector couldn't be kept constant as the momentum storage capacity goes to its minimum at the end of the energy generation phase. Operating the IPACS-CMG clusters inside its minimum momentum capacity should prevent this to happen. Consequently, the angular momentum requirements of the design shall be based on the minimum angular momentum capacity.

From the technological feasibility point of view, to have large energy storage capability with low mass, the flywheel of IPAC-CMG shall be capable of operating at high angular velocities. Magnetic bearings are known to make it

possible achieving such high angular speeds under control [18,19]. Since high rotational speeds also cause high stresses in flywheels at such high rotational speeds, a careful selection of flywheel geometry together with the utilization of high strength composite materials may be needed.

IPAC-CMG is covered in more detail in the next chapter. The device is analyzed both theoretically and through numerical simulations.

CHAPTER 4

INTEGRATED POWER AND ATTITUDE CONTROL – CONTROL MOMENT GYROSCOPE

4.1 Introduction

This chapter is dedicated to the IPAC-CMG. First the basic governing equations are given. Then, to show the similarities between these two different redundant actuator systems, the analogy between robotic manipulators and IPAC-CMG clusters is discussed. Then inverse kinematics problem in IPAC-CMG clusters and the steering solutions for this actuator system are given. The applicability of B-inverse to IPAC-CMG clusters is discussed. Finally, the results of the simulations performed are given and discussed.

4.2 Principles of IPAC-CMG

Since an IPAC-CMG is used both in attitude control and energy storage, the equations governing these functionalities are identified below.

The energy storage characteristic of an IPAC-CMG is defined by the energy and the power equations. Since energy is stored in the rotating flywheel of the IPAC-CMG, the amount of kinetic energy stored in the flywheel at any instant is given by

$$E_{stored} = \frac{1}{2}.I.\omega^2 \tag{4.1}$$

in which I is the mass moment of inertia of the flywheel with respect to its rotation axis and $\boldsymbol{\omega}$ is the angular velocity of the flywheel. The power of the flywheel is then given by

$$\mathrm{P} = \frac{dE}{dt} = I\omega.\dot{\omega} \tag{4.2}$$

Since an IPAC-CMG is an energy storage media, a mechanical battery, the performance parameters such as DOD and Specific Energy that are used for electrochemical batteries should also be defined for it. DOD, the maximum percent of the total battery capacity that is possible to remove from an IPAC-CMG during the discharge period, can be defined as:

$$DOD = 1 - \frac{\omega_{\min}^2}{\omega_{\max}^2} \tag{4.3}$$

where $\omega_{\min}$ and $\omega_{\max}$ are the minimum and maximum operational rotational speeds of the IPAC-CMG flywheel respectively. These speeds are design parameters of an IPAC-CMG and are determined by the designer of its flywheel (See Appendix A for a more detailed discussion on the design of the flywheel of an IPAC-CMG).

Again for IPAC-CMG, Specific Energy, the amount of energy that is stored in the unit mass of the storage device, is given by

$$SE = \frac{E_{stored}}{m} \tag{4.4}$$

In which m is the mass of the rotating flywheel in this case. SE is a key metric that is used to measure and compare the energy storage capabilities of different energy storage devices.

For the attitude control function of an IPAC-CMG the angular momentum of the flywheel and the torque produced by the device should be identified. The angular momentum of an IPAC-CMG is given by the formula

$$h = I.\omega \tag{4.5}$$

And the torque produced by the IPAC-CMG is given by the equation

$$\boldsymbol{\tau} = \dot{\delta} \times I\omega + I\dot{\omega} \tag{4.6}$$

In which $\dot{\delta}$ is the angular rate of the gimbal. The two ways of producing torque by an IPAC-CMG that are independent of each other at a given instant are clearly seen in this torque equation. One of these ways is by rotating the flywheel in a perpendicular direction to its rotation axis by rotating the gimbal, also known as the gyroscopic effect. As in the case of a CMG, this rotation changes the direction of the angular momentum of the flywheel, thus produces a torque whose direction is perpendicular to both of the rotation directions of the flywheel and the gimbal and whose magnitude is proportional to the magnitude of the angular momentum of the flywheel and gimbal rotation speed. The other way of producing torque is by changing the magnitude of the flywheel angular momentum due to the variation in the rotational speed of the flywheel. These torques are demonstrated on a sketch in Figure 4.1.

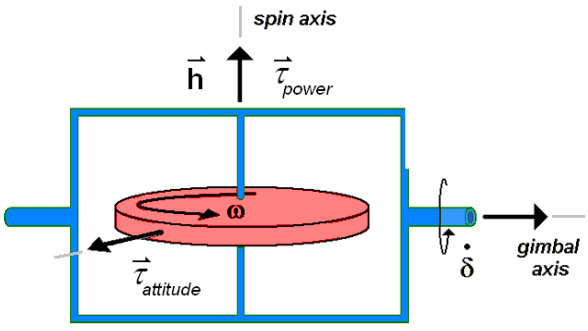

Figure 4.1 A sketch of IPAC-CMG showing the torques produced

As also pointed out in the previous chapter, the first torque producing motion, rotation of the gimbal, would be generated according to the attitude commands of the attitude control subsystem of the spacecraft, whereas the variation of the flywheel rotational speed, thus the torque produced by this way, is originated from the energy storage commands according to the power condition of the spacecraft. Consequently, the torque produced due to the variation of the flywheel angular speed is a byproduct of energy operations affecting the attitude of the spacecraft. This torque is the only coupling effect between energy storage and attitude control operations that come from the dual usage of a single device for both of these operations.

A single IPAC-CMG can produce torque in only one direction at an instant. To have a 3-axis attitude control in a spacecraft, at least three IPAC-CMGs should be used. In space applications, often an extra unit is added to have a redundant actuator cluster of four units. This redundancy provides an extra degree of freedom to the actuator system, which increases its control capability and as well as its operational reliability [43]. Four IPAC-CMGs may be arranged in different configurations with respect to each other according to the mission requirements of the spacecraft. The angular momentum and torque of an IPAC-CMG cluster for an arbitrary geometrical configuration is given by

$$\mathbf{h} = f(\boldsymbol{\delta}, \boldsymbol{\omega}) \tag{4.7}$$

$$\boldsymbol{\tau} = \frac{d\mathbf{h}}{dt} = \frac{df}{d\boldsymbol{\delta}} \cdot \frac{d\boldsymbol{\delta}}{dt} + \frac{df}{d\boldsymbol{\omega}} \cdot \frac{d\boldsymbol{\omega}}{dt} = \mathbf{J} \begin{Bmatrix} \dot{\boldsymbol{\delta}} \\ \dot{\boldsymbol{\omega}} \end{Bmatrix} \tag{4.8}$$

In this equation, $\mathbf{J}$ is the Jacobian matrix including the constant parameters of the IPAC-CMG cluster. This equation gives the kinematical relation between the torque of the IPAC-CMG cluster and the rotation rates of gimbals and flywheels. If the Jacobian matrix is thought as composed of two Jacobian matrices that are augmented column wise, Eq. 4.8 can also be written in different forms as given below:

$$\mathbf{J}\begin{Bmatrix}\dot{\boldsymbol{\delta}}\\ \dot{\boldsymbol{\omega}}\end{Bmatrix} = \mathbf{J}_{att}\dot{\boldsymbol{\delta}} + \mathbf{J}_{power}\dot{\boldsymbol{\omega}} = \boldsymbol{\tau}_{att} + \boldsymbol{\tau}_{power} \tag{4.9}$$

Here $\mathbf{J}_{power}$ relates $\dot{\boldsymbol{\omega}}$ to $\boldsymbol{\tau}_{power}$, which is the torque produced by the energy storage operations and $\mathbf{J}_{att}$ relates $\dot{\boldsymbol{\delta}}$ to $\boldsymbol{\tau}_{att}$, which is the attitude control torque. Here, $\mathbf{J}_{att}$ may be thought of as the Jacobian matrix of a CMG cluster whose flywheel rotational rates are different but constant at each and every instant. This representation provides us the ability to apply any driving algorithm in the literature that has been developed for CMG clusters for use in spacecraft attitude control.

4.3 The Mechanical Analogy

At this point, it should be noted that Eq. 4.8 of IPAC-CMG clusters is in a similar form as Eq. 2.2 of robotic manipulators. Both of these equations put the kinematical relationship between input variables to output variables of the corresponding actuator systems. This relationship between the CMG clusters and robotic manipulators, which is known as the mechanical analogy, is already shown in [6]. In this thesis work, we should extend this analogy to IPAC-CMG clusters, by adding a new analog parameter.

Like CMG clusters, inverse kinematics problem of IPAC-CMG clusters is similar to the inverse kinematics problem of robotic manipulators. The only difference between IPAC-CMG clusters and CMG clusters is that the magnitudes of the angular momentum vectors of the IPAC-CMGs are variable whereas CMG angular momentums have constant magnitude due to the constant speed of their flywheel. This difference should be added to build the new analogy. The situation is realized quiet easily when it is given in graphical form as in Figure 4.2.

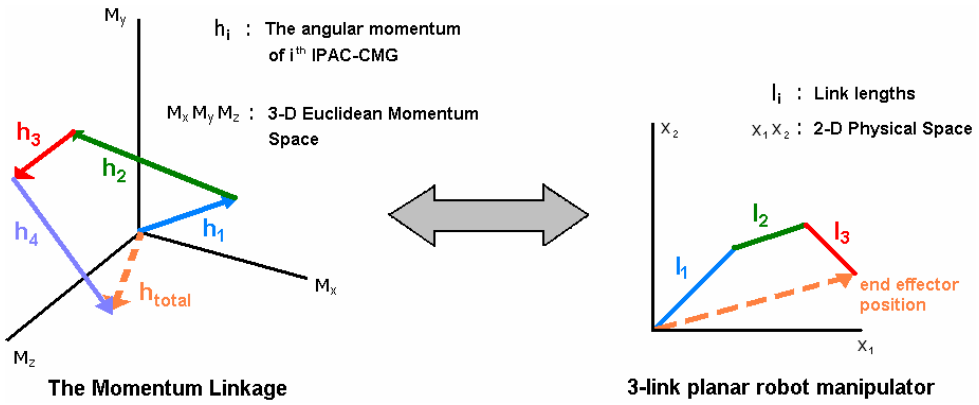

Figure 4.2 Graphical representation of the mechanical analogy between an IPAC-CMG cluster and a robotic manipulator

The momentum linkage concept used in Figure 4.2 helps us to understand the analogy. Shifting the application point of a vector to any location in space, with its magnitude and direction being unaltered, does not influence the vector itself. So, a cluster of IPAC-CMGs may be thought of angular momentum vectors added up in tip-to-tail fashion in momentum space. These analogous variables are also listed in TABLE 4.1 with an extension over the list given in [7]. In this analogy, the link lengths of the manipulator are correspondent to the angular momentum of each IPAC-CMG in the cluster. The variations in these angular momentum vectors of each IPAC-CMG in the cluster become equivalent to the variations in the link lengths of the robotic manipulator. So, through the window of this analogy, an IPAC-CMG cluster may be seen as a manipulator with variable link lengths.

TABLE 4.1 Analogous Quantities Between Two Actuator Systems

Robotic Manipulators	IPAC-CMG Cluster
End Effector Position	Total Angular Momentum of the Cluster
End Effector Task Space	Angular Momentum Envelope
End-Effector Velocity	Torque
Link Length	Magnitude of Angular Momentum Vector of Each IPAC-CMG
Singularity : No motion possible in a certain direction	Singularity : No torque possible in a certain direction
Manipulability Measure	Singularity Measure

4.4 Steering Laws for IPAC-CMG Clusters

The IPAC-CMG cluster is also redundant, so there is the problem of rectangular matrix inversion also. The steering laws used for manipulators may also be employed for IPAC-CMG clusters in order to find the gimbal rotation rates that will generate the commanded torque. For an IPAC-CMG cluster, Moore-Penrose pseudo inverse is

$$\dot{\delta}_{MP} = \mathbf{J}_{att}^{T}(\mathbf{J}_{att}\mathbf{J}_{att}^{T})^{-1}.(\boldsymbol{\tau}_{desired} - \boldsymbol{\tau}_{power}) \tag{4.10}$$

Provided that energy storage and drainage method is decided, $\boldsymbol{\tau}_{power}$ is a known quantity. But just as in the case of robotic manipulators, MP-inverse does not offer any solution for the singularity problem in IPAC-CMG case as well. The steering laws offered for the robotic manipulators and CMG clusters to handle the singularity problem may also be used for IPAC-CMG clusters.

On the other hand, to handle the singularity problem, two application forms of B-inverse steering law may be suggested for IPAC-CMG clusters. First form inverts only $\mathbf{J}_{att}$ to find the necessary gimbal rotation rates.

$$\dot{\boldsymbol{\delta}}_{BI} = \left[q\mathbf{I} + \mathbf{J}_{att}{}^{T}\mathbf{J}_{att}\right]^{-1}\left[q\dot{\boldsymbol{\delta}}_{des} + \mathbf{J}_{att}{}^{T}(\boldsymbol{\tau}_{desired} - \boldsymbol{\tau}_{power})\right] \tag{4.11}$$

where q is again the blending coefficient as explained in Chapter 2. Notice that, in the above steering law equations the power torque is subtracted from the desired torque and then this value is used in the steering law to find the necessary gimbal rates. If the power command coming from the power subsystem is known beforehand, it is possible to calculate the torque caused by the energy storage operations before the steering law calculations.

However, the structure of B-inverse is also suitable for an alternative form of steering approach. The flywheel spin accelerations may also be steered by B-inverse steering law as

$$\begin{Bmatrix} \dot{\boldsymbol{\delta}}_{BI} \\ \\ \dot{\boldsymbol{\omega}}_{BI} \end{Bmatrix} = \left[\mathbf{Q} + \mathbf{J}^{T}\mathbf{J}\right]^{-1}\left[\mathbf{Q}\begin{Bmatrix} \dot{\boldsymbol{\delta}}_{des} \\ \\ \dot{\boldsymbol{\omega}}_{des} \end{Bmatrix} + \mathbf{J}^{T}\boldsymbol{\tau}_{desired}\right] \tag{4.12}$$

In the above equation, $\dot{\boldsymbol{\omega}}_{des}$ is the column vector of flywheel spin accelerations commanded by the power subsystem and $\mathbf{Q}$ is a diagonal matrix containing blending coefficients. In this form, the entire Jacobian matrix of the actuator system, $\mathbf{J}$, is inverted and both the gimbal rotation rates required for the attitude control and the flywheel spin accelerations (or decelerations) required for the energy storage (or drainage) are determined accordingly. In this equation $\dot{\boldsymbol{\omega}}_{des}$ is a command that should strictly be followed by the cluster in an open loop fashion whereas the $\dot{\boldsymbol{\delta}}_{des}$ command is not to be strictly followed. The blending coefficient of flywheel acceleration commands should be relatively much higher than the blending coefficient of $\dot{\boldsymbol{\delta}}_{des}$ to realize the torque and $\dot{\boldsymbol{\omega}}_{des}$ commands closely while $\dot{\boldsymbol{\delta}}_{des}$ command is followed in a more relaxed fashion.

The blending matrix $\mathbf{Q}$ is in the form

$$\mathbf{Q} = \begin{bmatrix} q_{attitude}\mathbf{I}_4 & q_{power}\mathbf{I}_4 \end{bmatrix} \tag{4.13}$$

Proper values of $q_{attitude}$ and q_{power} are determined by trial and error.

Generally speaking, there is no difference between these two forms of application of B-inverse steering law in terms of steering performance. Both forms should realize the attitude and energy storage requirements in the same accuracy. In practice, a larger matrix is inverted in the second application whereas the extra operation of the first application is the calculation of $\boldsymbol{\tau}_{power}$ and its subtraction from the commanded torque. The first approach seems computationally more advantageous than its alternative. However, the second approach is examined in this thesis work, to demonstrate the capabilities of B-inverse steering law. To command two different variables of different steering characteristics in a single calculation is only possible with the B-inverse steering law.

4.5 Control Algorithm Construction

In this section, the mathematical model of a cluster of four IPAC-CMGs and the algorithms to drive the cluster are constructed. The block diagrams representing the two possible control approaches that are suggested in the previous section are given in Figure 4.3 and Figure 4.4 respectively. Since both diagrams contain the same blocks except the steering law block, it is more convenient to discuss the elements of the IPAC-CMG cluster control algorithm part by part under the heading of these blocks. After that, they will be tested through numerical simulations in the next section.

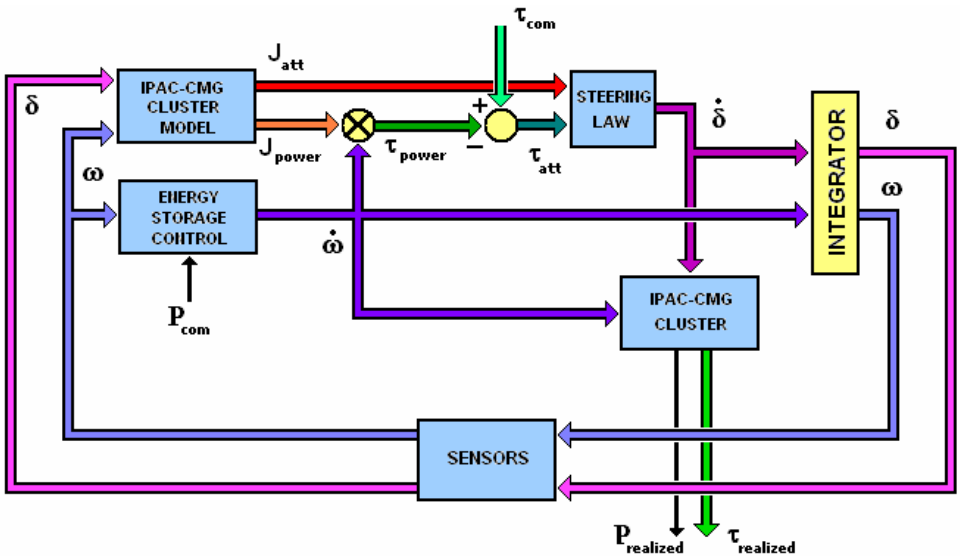

Figure 4.3 Block diagram of IPAC-CMG cluster control model for any steering law.

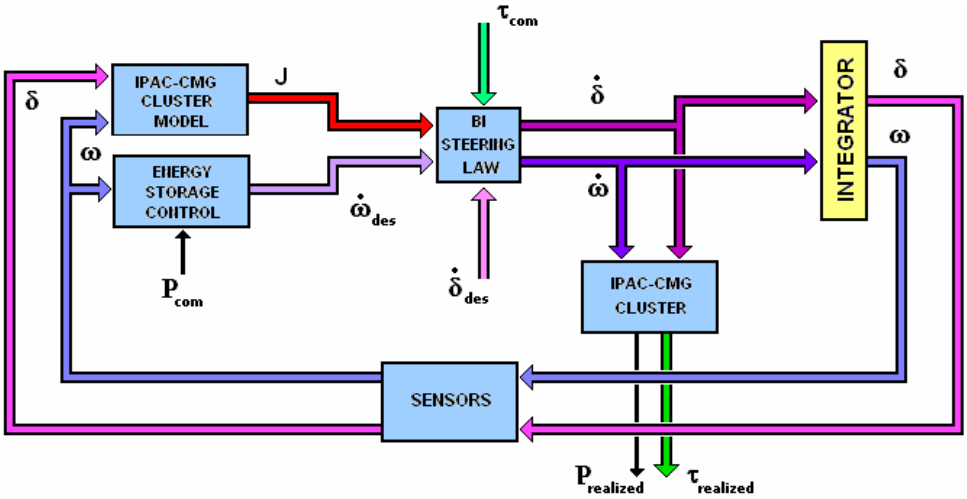

Figure 4.4 Block diagram of IPAC-CMG cluster control model for B-Inverse.

4.5.1 IPAC-CMG Cluster

The first step in constructing a control algorithm for a system is to lay down the mathematical model of the plant. The IPAC-CMG cluster is arranged in a pyramid configuration with a pyramid skew angle of $\beta = 54.73°$ (See Figure 4.5). This

configuration is shown to be the most optimum arrangement in terms of uniformity of the angular momentum envelope of the CMG clusters [26] and in this IPAC-CMG study here.

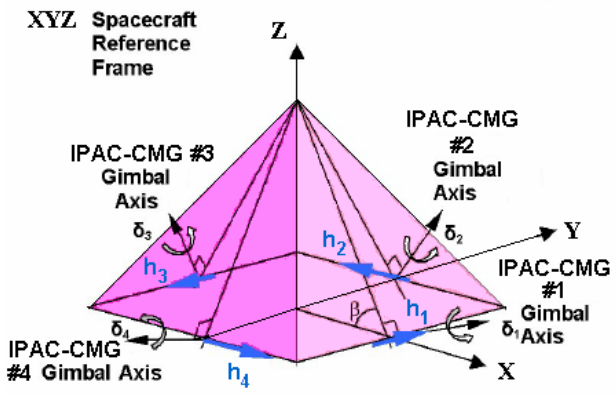

Figure 4.5 Pyramid Arrangement of an IPAC-CMG Cluster [21]

The angular momentum equation, Eq. 4.7, now can be written explicitly for this cluster configuration as

$$\mathbf{h}_{cluster} = \begin{bmatrix} -I\omega_1 \sin\delta_1 c\beta - I\omega_2 \cos\delta_2 + I\omega_3 \sin\delta_3 c\beta + I\omega_4 \cos\delta_4 \\ I\omega_1 \cos\delta_1 - I\omega_2 \sin\delta_2 c\beta - I\omega_3 \cos\delta_3 + I\omega_4 \sin\delta_4 c\beta \\ I\omega_1 \sin\delta_1 s\beta + I\omega_2 \sin\delta_2 s\beta + I\omega_3 \sin\delta_3 s\beta + I\omega_4 \sin\delta_4 s\beta \end{bmatrix} \tag{4.14}$$

And the torque generated by accelerating flywheels or rotating the gimbals may be found by taking the time derivative of Eq. 4.14

$$\boldsymbol{\tau} = \mathbf{J}(\boldsymbol{\omega}, \boldsymbol{\delta}).\begin{Bmatrix} \dot{\boldsymbol{\delta}} \\ \\ \dot{\boldsymbol{\omega}} \end{Bmatrix} \tag{4.15}$$

In this equation, $\mathbf{J}$ is the Jacobian matrix of the IPAC-CMG cluster.

$$\mathbf{J}(\boldsymbol{\omega},\boldsymbol{\delta}) = \begin{bmatrix} -I\omega_1 c\delta_1 c\beta & I\omega_2 s\delta_2 & I\omega_3 c\delta_3 c\beta & -I\omega_4 s\delta_4 & -Is\delta_1 c\beta & -Ic\delta_2 & Is\delta_3 c\beta & Is\delta_4 \\ -I\omega_1 s\delta_1 & -I\omega_2 c\delta_2 c\beta & I\omega_3 s\delta_3 & I\omega_4 c\delta_4 c\beta & Ic\delta_1 & -Is\delta_2 c\beta & -Ic\delta_3 & Is\delta_4 c\beta \\ I\omega_1 c\delta_1 s\beta & I\omega_2 c\delta_2 s\beta & I\omega_3 c\delta_3 s\beta & I\omega_4 c\delta_4 s\beta & Is\delta_1 s\beta & Is\delta_2 s\beta & Is\delta_3 s\beta & Is\delta_4 s\beta \end{bmatrix} \quad (4.16)$$

where, the column vector of Eq. 4.15 is

$$\begin{Bmatrix} \dot{\boldsymbol{\delta}} \\ \dot{\boldsymbol{\omega}} \end{Bmatrix} = \begin{Bmatrix} \dot{\delta}_1 & \dot{\delta}_2 & \dot{\delta}_3 & \dot{\delta}_4 & \dot{\omega}_1 & \dot{\omega}_2 & \dot{\omega}_3 & \dot{\omega}_4 \end{Bmatrix}^T \quad (4.17)$$

This column vector includes the gimbal rotation rates and flywheel rotational accelerations of all of the IPAC-CMGs in the cluster.

In order to perform numerical simulations using these equations, all the parameters of them should be assigned a numerical value. This necessitates at least a conceptual design of an IPAC-CMG system to determine flywheel spin rate limitations and inertias. The calculations are made according to average energy storage and attitude control requirements of a typical Earth observation satellite at LEO. The details of the conceptual design calculations performed for this purpose are given in Appendix A. The relevant properties of the flywheel selected for the simulations are listed in TABLE 4.2.

TABLE 4.2 IPAC-CMG Flywheel Selection (Also see Appendix A)

Energy Storage for each IPAC-CMG [Wh]	25
Min Angular Momentum Capacity of each IPAC-CMG [Nms]	7.7
IPAC-CMG Flywheel Mass Moment of Inertia [kgm^2]	0.0049
IPAC-CMG Max. Flywheel Rotational Speed [kRPM]	60

In the simulations, the mathematical model of the IPAC-CMG cluster described above is used in two different blocks. In IPAC-CMG Cluster Model Block, the model is used to calculate the instantaneous Jacobian matrix to find the necessary gimbal and wheel spin rates. In IPAC-CMG Cluster Block, the same mathematical model is used to calculate the realized power and torque output of the actuator system as if the cluster is modeled perfectly. Thus, any mismatch between the required power and torque outputs and realized ones will be due to the steering calculations.

4.5.2 Energy Storage Control

The energy management of IPAC-CMG cluster is driven according to the power command coming from the power subsystem of the spacecraft. But the distribution of this power command to each IPAC-CMG in the cluster should be regulated. For this purpose, a control algorithm that establishes the contribution of each IPAC-CMG in the cluster to the energy activities is described below.

In energy management, one has the complete freedom of delivering the power command to each of the IPAC-CMGs in the cluster in a desired manner. Any algorithm that follows a storage objective can be employed in this operation. In this thesis study, the algorithm tries to equalize the flywheel rotational speeds of each IPAC-CMG.

The algorithm for energy management is given below. Define, c_k ,

$$c_k = \frac{\mathrm{P}_k}{\mathrm{P}_{com}} \qquad \text{for } \mathrm{k} = 1, 2, 3, 4 \tag{4.18}$$

which is the ratio between the desired power command send to the IPAC-CMG cluster, P_{com} and the power command send to each IPAC-CMG in the cluster, P_k .

Also define, r_k,

$$r_k = \frac{\omega_{\max}^2 - \omega_k^2}{\omega_{\max}^2 - \omega_{\min}^2} \qquad \text{for k = 1, 2, 3, 4} \tag{4.19}$$

which contains the flywheel rotational speed information of each IPAC-CMG. In order to distribute the power requirement to each IPAC-CMGs according to the energy content information in r_k, the ratio c_k may be determined by

For $P_{com} \rangle 0$ For $P_{com} \langle 0$

$$c_k = \frac{r_k}{\sum_k r_k} \qquad c_k = \frac{1 - r_k}{\sum_k r_k} \tag{4.20}$$

As the last step, the power of each flywheel is defined as

$$P_k = I\omega_k\dot{\omega}_k \quad \text{for } k = 1, 2, 3, 4 \tag{4.21}$$

Assuming I is equal for each IPAC-CMG flywheel, the angular acceleration command to each IPAC-CMG can be determined as

$$\dot{\omega}_k = \frac{P_{com}c_k}{I\omega_k} \quad \text{for } k = 1, 2, 3, 4 \tag{4.22}$$

Consequently, this simple algorithm would be able to deliver the power command to the IPAC-CMGs with the objective of leveling the flywheel rotational speeds of each IPAC-CMGs in the cluster. This algorithm is used in the Energy Storage Control Blocks of the block diagrams in Figure 4.3 and Figure 4.4.

4.5.3 Steering Law

As in the case of robotic manipulators, two steering laws are employed in IPAC-CMG cluster simulations; MP-inverse and B-inverse Steering Laws. MP-inverse is applied as in the form given in Eq. 4.10. It is the simplest and natural solution to the inverse of a rectangular matrix for redundant IPAC-CMG Cluster. For B-inverse, on the other hand, two methods were proposed in Section 4.2. In the following numerical simulations, the form given in Eq. 4.12 is used, since it demonstrates the blending capabilities of B-inverse. The application of B-inverse in the form given in Eq. 4.11 is not presented, since it would be the same as in the case of its application to CMG clusters. The performance of B-inverse for CMG clusters has been previously shown [51].

4.6 Numerical Simulations

In this section, the performances of the control algorithms constructed for IPAC-CMG clusters are evaluated through simulations. A single test case is performed in the simulations. The attitude control part of the test case is taken from [51] for comparison and verification purposes. Some numerical modifications, however, are made in the parameters of that test case to tailor it for the IPAC-CMG cluster and to obtain presentable simulation results.

The simulation parameters of the test case are presented in TABLE 4.3. In this test case, the IPAC-CMG cluster is asked to produce a constant torque up to its angular momentum capacity at the instant. The simulation runs until the cluster reaches its maximum angular momentum value. As a constant torque is requested from the cluster, energy is being drawn from the IPAC-CMG flywheels simultaneously. The torque command to the cluster and its resulting ideal angular momentum profile with the initial conditions given in TABLE 4.3 are given in Figure 4.6. The power command and energy profile are also shown in Figure 4.7.

TABLE 4.3 Test Case Parameters

Simulation Time [sec]	183.8
Initial IPAC-CMG Flywheel Spin Rate [kRPM]	[40 40 40 40]
Initial Gimbal Angles [deg]	[0 0 0 0]

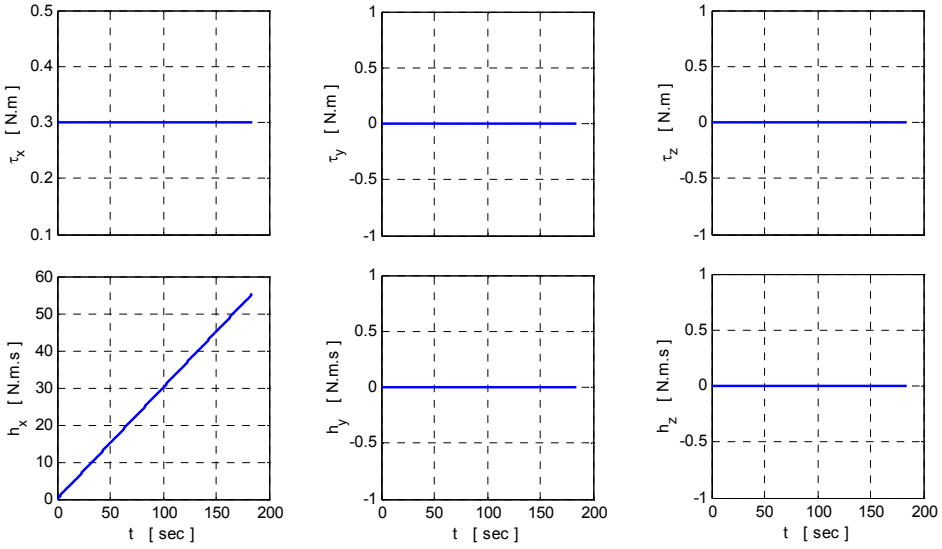

Figure 4.6 Torque command and ideal angular momentum profile for IPAC-CMG cluster test case

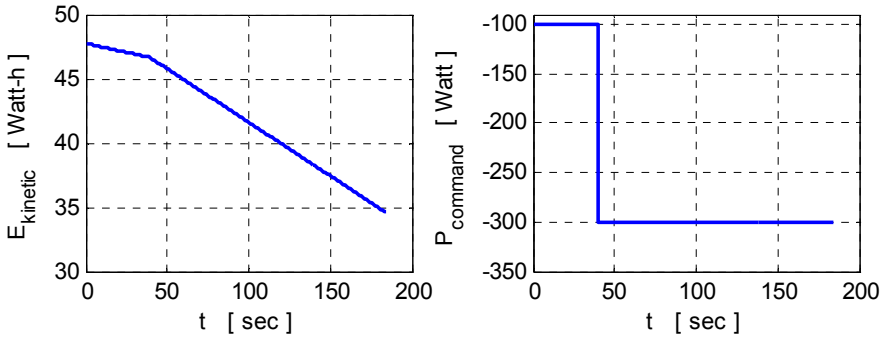

Figure 4.7 Energy profile and power command of the IPAC-CMG cluster test case

4.6.1 MP-inverse Simulation

The results obtained from using MP-inverse steering algorithm in the simulations are given in figures Figure 4.8 to Figure 4.12. The simulation results show that the IPAC-CMG cluster performs well and the commanded torque and power profiles are accurately realized for about 75 seconds. From Figure 4.8, it may be observed that the singularity measure drops to zero and the IPAC-CMG cluster sets trapped into a singularity at around $t = 75\,\text{sec}$.

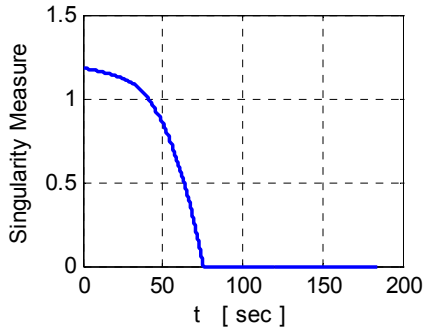

Figure 4.8 Singularity measure of the IPAC-CMG cluster

The torque and angular momentum profiles of the simulation are given in Figure 4.9. The cluster is not able to produce the desired torque after it gets trapped in this singularity. Instead, it produces only a small torque in x-direction, which is originated from the energy storage operation. Since it is not possible to produce torque by gimbal rotations, the power torque couldn't be eliminated in a singular configuration and produced inevitably.

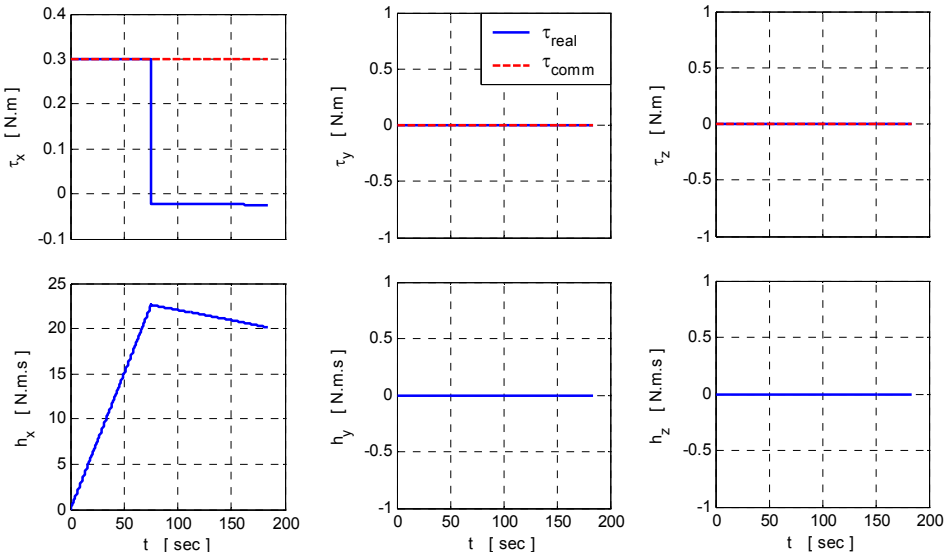

Figure 4.9 History of torque and angular momentum of the IPAC-CMG cluster

In the singular configuration the gimbal angles are [-90 0 90 0] in degrees, as seen in Figure 4.10. Physically, all the angular momentum vectors of the cluster are parallel to x-axis in this configuration and it is not possible for the IPAC-CMG cluster to produce torque in x-direction by gimbal rotation.

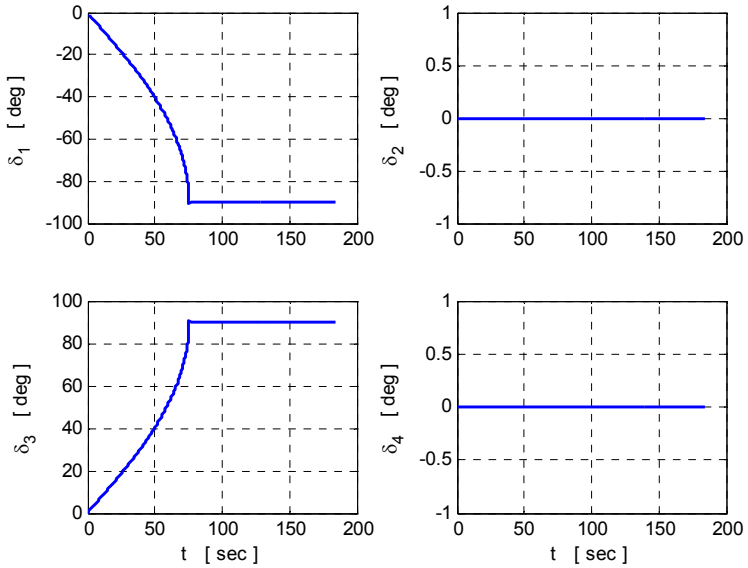

Figure 4.10 Gimbal angle history of the IPAC-CMG cluster

On the other hand, the energy storage operation of the cluster is not affected from the singularity and the cluster continues to realize the power command satisfactorily even in the singular configuration. Obviously this is an expected result, since the flywheel spin rates are directly driven by the power command. The energy and power profiles of the cluster and the flywheel spin rates are given in Figure 4.11 and Figure 4.12 respectively. Notice that, equal initial spin rates leads to equal decelerations in the flywheels throughout the simulation.

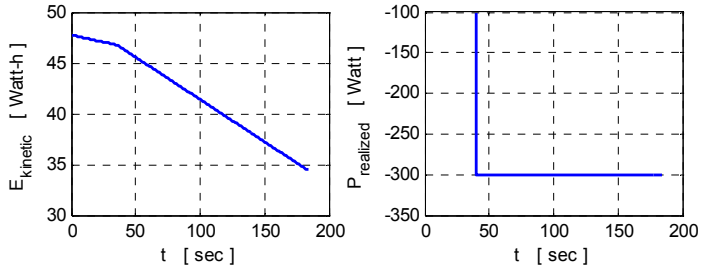

Figure 4.11 Energy and power profiles of the IPAC-CMG cluster

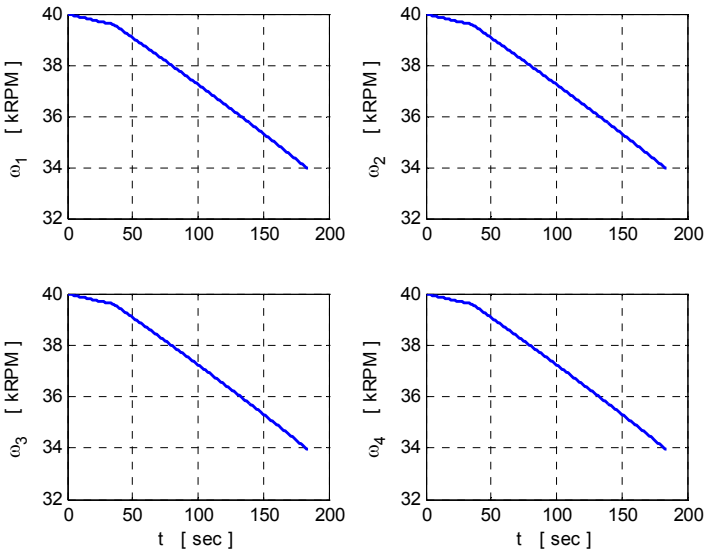

Figure 4.12 Flywheel angular speeds of the IPAC-CMG cluster

4.6.2 B-inverse Simulation

The same test case is repeated this time using the B-inverse steering law. B-inverse is used with proper nodes to steer the cluster and escape the singular configuration. The nodal gimbal angle configurations listed in TABLE 4.4 are directly taken from [51]. Their locations in time are changed since the angular momentum capacity of the IPAC-CMG cluster and torque commands of this test case are different than the simulations performed in [51]. Also, some unnecessary nodes are excluded to show the flexibility in the node selection.

TABLE 4.4 List of Nodes used by BI in cluster simulations

Node	Time [sec]	Gimbal Angles [deg]
1	24.0	[-11.6 -1.6 43.6 -27.4]
2	48.0	[-46.2 24.2 86.6 -43.4]
3	72.0	[-74.2 57.4 127.2 -42.6]
4	96.0	[-111 93.3 177.4 -6.3]
5	144.0	[-80.4 126.8 129.7 -35.5]
6	186.0	[-90 180 90 0]

The blending coefficients, $q_{attitude}$ and q_{power} of Eq. 4.13 are taken as 1×10^{-5} and 1×10^{-1} respectively according to the tracking objectives of the IPAC-CMG cluster. The tracking objectives in this actuator system are to satisfy the $\dot{\boldsymbol{\omega}}$ commands in an open loop fashion, and to generate the commanded torque accurately in the meantime. In generating this torque, the cluster is intentionally steered away from singularity by dictating the nodal configurations to the cluster. But these nodal configurations do not have to be followed strictly. Having a trajectory close to these configurations would be sufficient for the cluster to stay away from a singularity. For the gimbals, generating the commanded torque has higher importance than following the nodes firmly. That's why the blending

coefficient for the $\dot{\boldsymbol{\delta}}_{des}$ is small and the closed loop control is preserved, whereas the blending coefficient for the $\dot{\boldsymbol{\omega}}_{des}$ is greater, providing a control in open loop fashion.

The results of the simulation are given in graphs through figures Figure 4.13 to Figure 4.17. The cluster reaches to the saturation point, the end of its momentum storage capability, without encountering any singularity on the way. The singularity measure is given in Figure 4.13. It reaches to zero at the end of the simulation.

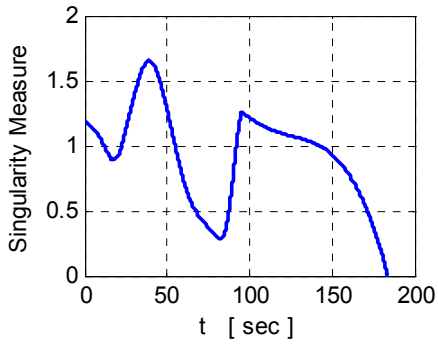

Figure 4.13 Singularity measure of the IPAC-CMG cluster

Since the singularity is avoided, in Figure 4.14 the torque error in realizing the commanded torque is plotted instead of the realized torque history. The realized angular momentum profile is also given in Figure 4.14. It may be observed from the figure that, the torque command is realized quite accurately. Note that, at the end of the simulation, where the angular momentum capacity of the IPAC-CMG cluster is reached, the torque error increases. In space applications, the accumulated angular momentum is always dumped with the thrusters or magnetic torquers to avoid reaching saturation.

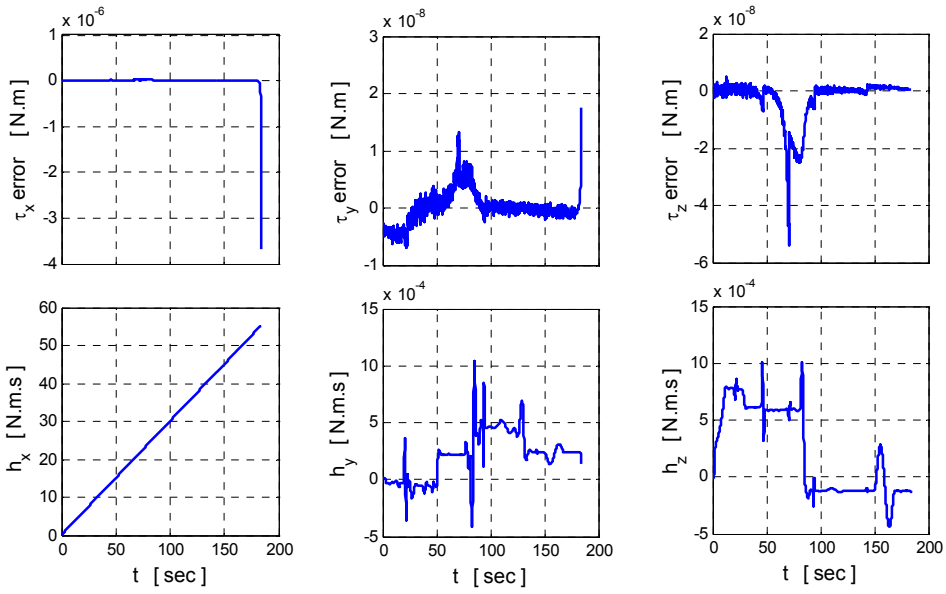

Figure 4.14 Torque errors and angular momentum of the IPAC-CMG cluster

The gimbal angle histories are plotted in Figure 4.15. The nodes to be followed are shown in the plots as large circles instead of specific points to spot the nodes with their neighborhoods. It is observed that the gimbals follow the nodal configurations very crudely, since the blending coefficient used is quite small ($q_{attitude} = 1 \times 10^{-5}$). However, this value is observed to be sufficient to keep the cluster away from a singular configuration.

The energy profile and the power error in realizing the commanded power are given in Figure 4.16 together. When the cluster is far from its angular momentum boundary, the power error is on the order of 10^{-8}. But, just like the torque error given in Figure 4.14, power error also increases as the maximum angular momentum capacity of the IPAC-CMG cluster is reached (saturation singularity).

The obtained flywheel spin rates during combined steering and power drainage operation are almost identical to those obtained by the MP-inverse simulations (Figure 4.17).

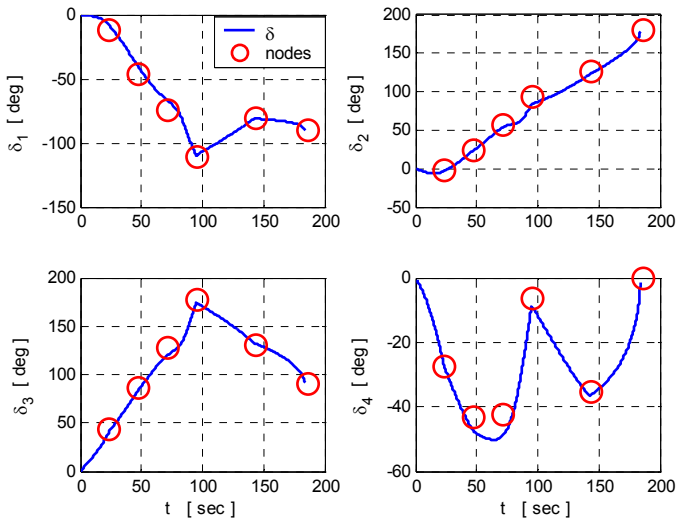

Figure 4.15 Gimbal angle history of the IPAC-CMG cluster

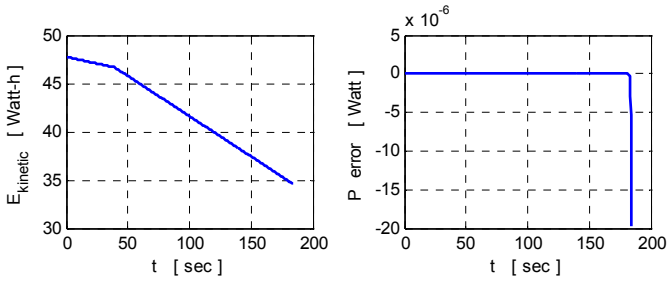

Figure 4.16 Power error and energy of the IPAC-CMG cluster

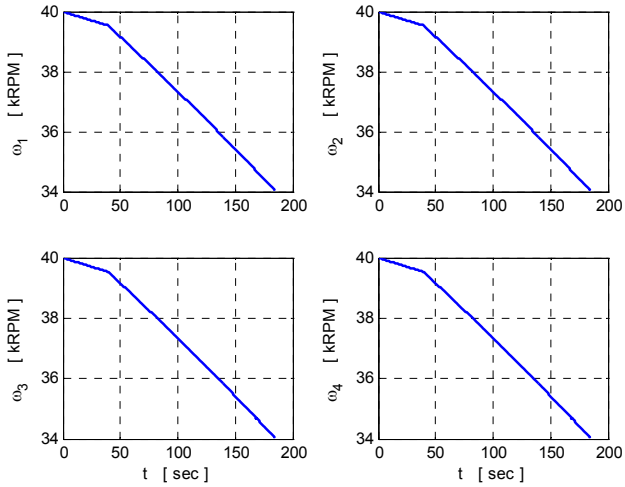

Figure 4.17 Flywheel angular speeds of the IPAC-CMG cluster

CHAPTER 5

SPACECRAFT INTEGRATED POWER AND ATTITUDE CONTROL SYSTEM SIMULATIONS

5.1 Introduction

The IPAC-CMG actuator system and the control algorithms that drive it are placed in a spacecraft IPACS simulation model. The governing equations are derived first. Then, a test case is arranged to investigate the performance of the IPAC-CMG cluster and B-inverse steering logic in a spacecraft IPACS. The test case is simulated first with MP-inverse steering law and then with B-inverse steering law. The results of these simulations are presented and compared.

5.2 Equations Governing the Spacecraft with IPACS

IPACS is a part of two different subsystems of a spacecraft. The attitude determination and control subsystem of the spacecraft is a closed-loop autonomous system, which controls the attitude of the spacecraft at the desired orientation as commanded by a higher-level decision unit. The task of IPACS in this subsystem is to generate the control torques required to perform this task. On the other hand, IPACS stores the necessary backup energy for the electrical power subsystem. This subsystem is in charge of generating and supplying the power to the whole spacecraft. In this context, power management and distribution unit of this subsystem delivers the power commands to IPACS system at each instant in order to store or draw backup energy. A block diagram describing the utilization of IPACS in these two subsystems is presented Figure 5.1.

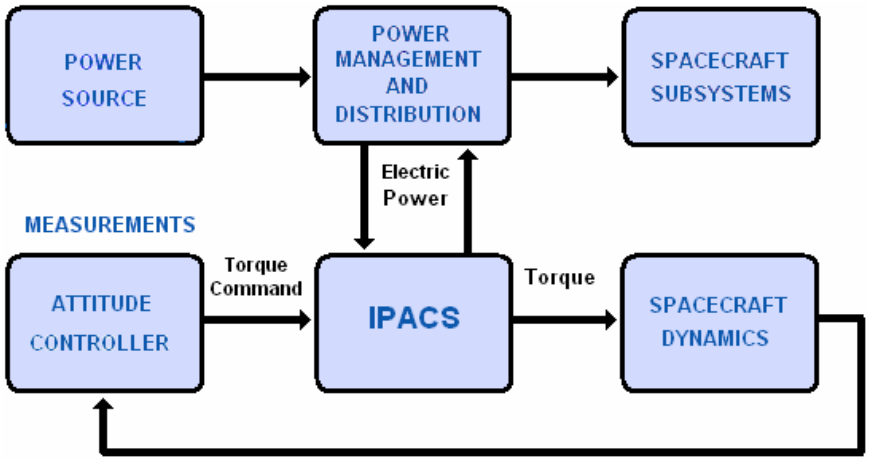

Figure 5.1 Generic block diagram of IPACS as a part of Attitude Determination and Control Subsystem and Electrical Power Subsystem

A simulation model of a spacecraft equipped with IPACS is given in Figure 5.2. In modeling the attitude control and determination subsystem, the attitude determination function of the subsystem is assumed to perfectly supply the attitude and rate information. The desired attitude and the desired power are directly commanded to the model, without modeling the attitude and power environment of IPACS and the spacecraft. The sources of these two commands are shown in dashed blocks in the figure. The model of the IPAC-CMG actuator system including the driving algorithms was presented in the previous chapter. The mathematical models of the rest of the system are given in the following subsections.

5.2.1 Spacecraft Equations of Motion

In this subsection, the set of equations governing the motion of a spacecraft are derived. The equations are set in a form suitable for the closed-loop attitude control of the spacecraft by the IPAC-CMG cluster. The equations are given in the spacecraft body-fixed frame. The following derivation is due to [50] and repeated here for the sake of completeness.

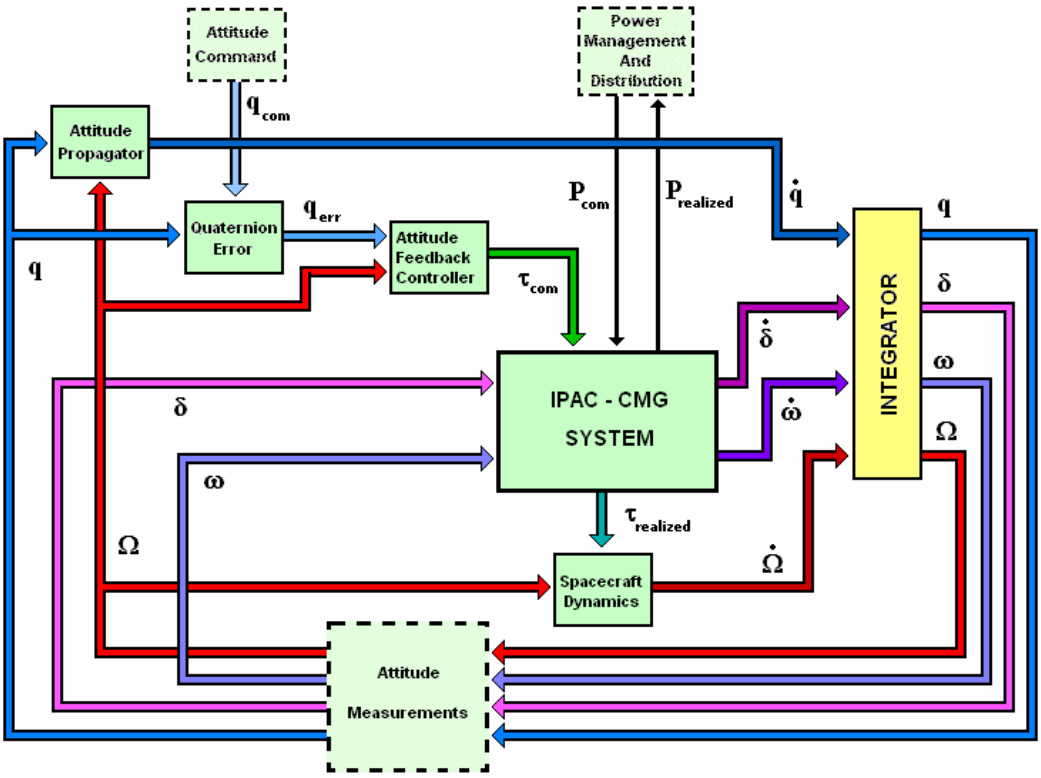

Figure 5.2 Block diagram of the simulation model of a spacecraft equipped with IPACS (dashed blocks are not modeled)

The angular momentum of the spacecraft is given by

$$\mathbf{h}_{S/C} = \mathbf{I}_{S/C}.\boldsymbol{\Omega} + \mathbf{h}_{IPACS} \tag{5.1}$$

where, $\mathbf{h}_{S/C}$ is the angular momentum vector of the total spacecraft, $\mathbf{I}_{S/C}$ is the spacecraft inertia matrix, including IPAC-CMGs, $\boldsymbol{\Omega}$ is the spacecraft angular velocity vector and $\mathbf{h}_{IPACS}$ is the total IPAC-CMG momentum vector, all expressed in the spacecraft body-fixed reference frame. Again in the body-fixed reference frame, the rotational equation of motion of a rigid spacecraft is given by

$$\dot{\mathbf{h}}_{S/C} + \boldsymbol{\Omega} \times \mathbf{h}_{S/C} = \boldsymbol{\tau}_{ext} \tag{5.2}$$

$\boldsymbol{\tau}_{ext}$ is the resultant external torque applied on the spacecraft. These equations are combined to have

$$\mathbf{I}_{S/C}.\dot{\boldsymbol{\Omega}} + \dot{\mathbf{h}}_{IPACS} + \boldsymbol{\Omega} \times (\mathbf{I}_{S/C}.\boldsymbol{\Omega} + \mathbf{h}_{IPACS}) = \boldsymbol{\tau}_{ext} \tag{5.3}$$

Rearranging the equation

$$\mathbf{I}_{S/C}.\dot{\boldsymbol{\Omega}} + \dot{\mathbf{h}}_{IPACS} + \boldsymbol{\Omega} \times \mathbf{h}_{IPACS} + \boldsymbol{\Omega} \times \mathbf{I}_{S/C}.\boldsymbol{\Omega} = \boldsymbol{\tau}_{ext} \tag{5.4}$$

Now, the terms including the parameters of the IPAC-CMG cluster may be gathered under a single variable, which is to be used in the feedback control:

$$\mathbf{u} = -\dot{\mathbf{h}}_{IPACS} - \boldsymbol{\Omega} \times \mathbf{h}_{IPACS} \tag{5.5}$$

In this equation, $\mathbf{u}$ can be defined as the total torque effect of the IPAC-CMG system on the spacecraft. Rewriting Eq. 5.4 using $\mathbf{u}$ gives us

$$\mathbf{I}_{S/C}\dot{\boldsymbol{\Omega}} = (\boldsymbol{\tau}_{ext} + \mathbf{u} - \boldsymbol{\Omega} \times \mathbf{I}_{S/C}.\boldsymbol{\Omega}) \tag{5.6}$$

We can simply integrate this equation to find the spacecraft angular rates in time. In principal coordinates this equation becomes:

$$\begin{aligned}
I_X\dot{\Omega}_X &= \tau_X - \Omega_Y\Omega_Z(I_Z - I_Y) - \dot{h}_X - \Omega_Y h_Z + \Omega_Z h_Y \\
I_Y\dot{\Omega}_Y &= \tau_Y - \Omega_X\Omega_Z(I_X - I_Z) - \dot{h}_Y - \Omega_Z h_X + \Omega_X h_Z \\
I_Z\dot{\Omega}_Z &= \tau_Z - \Omega_X\Omega_Y(I_Y - I_X) - \dot{h}_Z - \Omega_X h_Y + \Omega_Y h_X
\end{aligned} \tag{5.6}$$

5.2.2 Spacecraft Attitude Representation

The attitude representation of the spacecraft is described in terms of the quaternions, which is the most common way in today's aerospace applications. The error quaternion, $\mathbf{q_e} = [q_{1e} \quad q_{2e} \quad q_{3e} \quad q_{4e}]^T$, stating the instantaneous difference between the current attitude, $\mathbf{q_{cur}} = [q_{1cur} \quad q_{2cur} \quad q_{3cur} \quad q_{4cur}]^T$, and the commanded attitude, $\mathbf{q_{com}} = [q_{1com} \quad q_{2com} \quad q_{3com} \quad q_{4com}]^T$, is determined as follows:

$$\begin{bmatrix} q_{1e} \\ q_{2e} \\ q_{3e} \\ q_{4e} \end{bmatrix} = \begin{bmatrix} q_{4com} & q_{3com} & -q_{2com} & -q_{1com} \\ q_{3com} & q_{4com} & q_{1com} & -q_{2com} \\ -q_{2com} & q_{1com} & q_{4com} & -q_{3com} \\ q_{1com} & -q_{2com} & q_{3com} & -q_{4com} \end{bmatrix} \begin{bmatrix} q_{1cur} \\ q_{2cur} \\ q_{3cur} \\ q_{4cur} \end{bmatrix} \tag{5.7}$$

The propagation of the quaternions in time is performed by the below equation:

$$\dot{\mathbf{q}} = \frac{1}{2}\mathbf{Q}.\mathbf{q} \tag{5.8}$$

where $\mathbf{Q}$ is a matrix consisting of the spacecraft angular rates as:

$$\mathbf{Q} = \begin{bmatrix} 0 & \Omega_3 & -\Omega_2 & \Omega_1 \\ -\Omega_3 & 0 & \Omega_1 & \Omega_2 \\ \Omega_2 & -\Omega_1 & 0 & \Omega_3 \\ -\Omega_1 & -\Omega_2 & -\Omega_3 & 0 \end{bmatrix} \tag{5.9}$$

For the above formulations one may refer to [50,39].

5.2.3 Attitude Feedback Controller

A linear state feedback controller for the spacecraft given in Section 5.2.1 is also taken from [50]. The attitude error quaternions computed in Eq. 5.7 and the angular velocity vector of the spacecraft are fed to the controller to determine the control torque to be applied to the spacecraft as follows:

$$\mathbf{u} = -\mathbf{K}\mathbf{q}_{ev} - \mathbf{D}\boldsymbol{\Omega} \tag{5.10}$$

Here $\mathbf{q}_{ev} = \begin{bmatrix} q_{1ev} & q_{2ev} & q_{3ev} \end{bmatrix}^T$ is the quaternion vector with the first three quaternions. The controller gain matrices $\mathbf{K}$ and $\mathbf{D}$ are determined using the spacecraft inertia matrix as:

$$\begin{aligned} \mathbf{K} &= k\mathbf{I}_{S/C} \\ \mathbf{D} &= d\mathbf{I}_{S/C} \end{aligned} \tag{5.11}$$

where k and d are defined by the damping ratio (ζ) and the natural frequency (ω_n) as:

$$\begin{aligned} d &= 2\zeta\omega_n \\ \frac{k}{2} &= \omega_n{}^2 \end{aligned} \tag{5.12}$$

5.3 Numerical Simulations

In this section, simulation results are given to demonstrate the performance of B-inverse steering law for IPAC-CMG cluster in the spacecraft and. First, simulation with MP-inverse is performed. Then B-inverse results are given and compared with MP-inverse results.

The simulation parameters used are tabulated in TABLE 5.1. The IPAC-CMG cluster that is described in Chapter 4 is also used in the simulations below. The initial gimbal angle configuration is taken close to the [-90, 0, 90, 0] singular configuration to shorten the duration that the cluster falls into singularity.

TABLE 5.1 Spacecraft IPACS Simulation Parameters

Spacecraft Inertias [kg.m^2]	[15 15 10]
Initial Orientation of Spacecraft in Euler Angles [deg]	[0 0 0]
IPAC-CMG Flywheel Mass Moment of Inertia [kg.m^2]	0.0049
Max./ Min. IPAC-CMG Flywheel Spin Rates [kRPM]	60 / 15
Initial IPAC-CMG Flywheel Spin Rate [kRPM]	[39 40 41 42]
Initial Gimbal Angles [deg]	[-75 0 75 0]

This simulation includes a power command that changes in a stepwise manner in time and a roll maneuver command to be realized in 60 seconds. These power and attitude commands are plotted in Figure 5.3 and Figure 5.4 respectively. The attitude command is given 50 seconds after the simulation starts, so the power performance of IPACS may be observed independent of attitude operations. The power command is switched to different values at different time points to check the transient effects on IPACS.

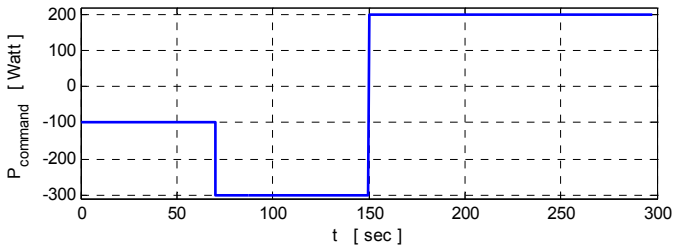

Figure 5.3 Power command to IPACS

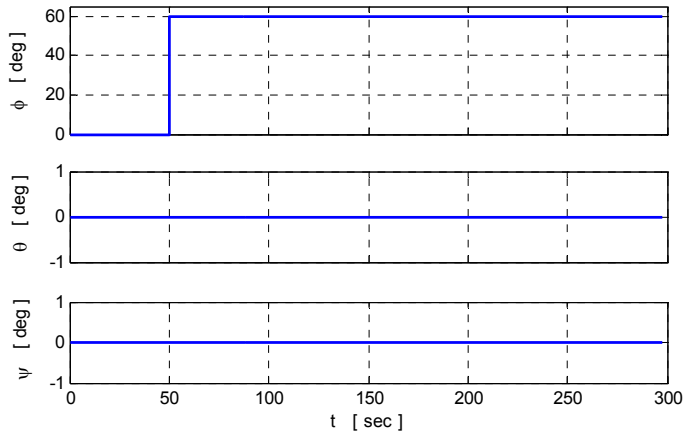

Figure 5.4 Attitude command to IPACS

5.3.1 MP-inverse Simulations

The IPAC-CMG cluster steered by MP-inverse falls into the singularity at around $t = 100\,\text{sec}$ (Figure 5.5). It is seen that the cluster cannot get out of the singular configuration into which it is trapped. Consequently, the attitude maneuver couldn't be performed in desired time and profile. The attitude history of the spacecraft is given in Figure 5.6. As it is seen from the figure, after $t = 100\,\text{sec}$, the orientation of the spacecraft is completely out of control and the attitude orientation of the spacecraft is changing with the torques produced by the power operations of the IPAC-CMG cluster. It should be noticed that the stepwise changes in the power operations do not disturb the singularity measure of the IPAC-CMG cluster.

The kinetic energy and power of the IPAC-CMG cluster, seen in Figure 5.7, shows that there is no anomaly in the power operations of the spacecraft and the power history of the IPAC-CMG cluster is identical to the commanded one given in Figure 5.3.

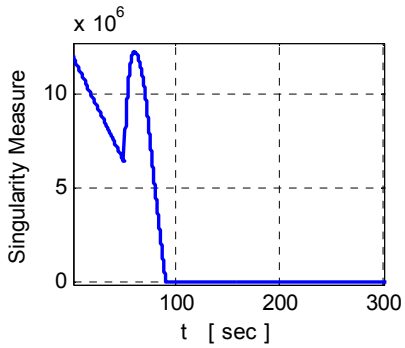

Figure 5.5 Singularity measure of IPAC-CMG cluster during the simulation

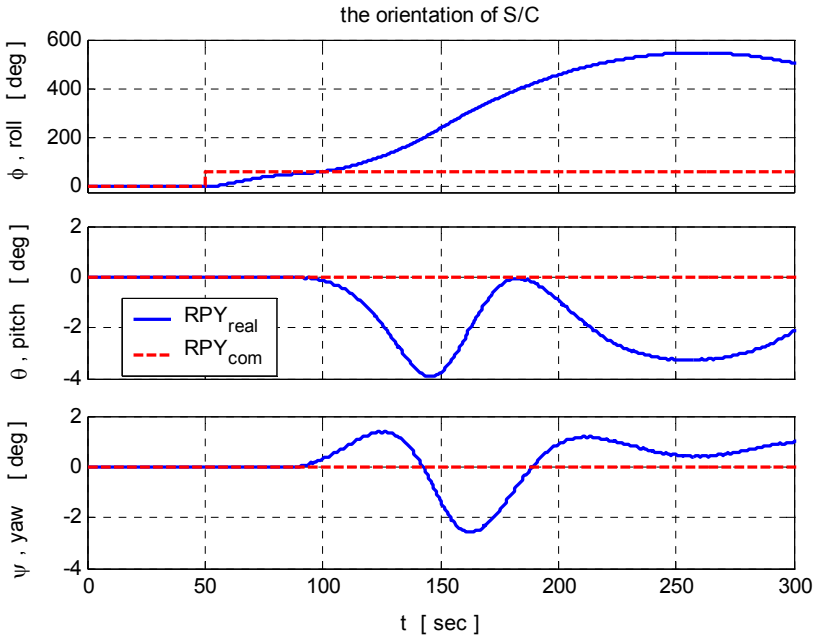

Figure 5.6 Attitude orientation of the spacecraft in Euler angles

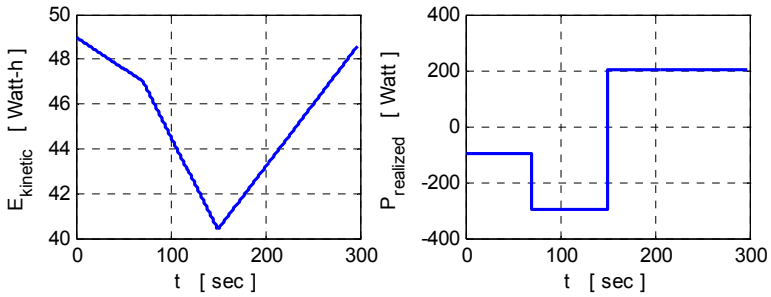

Figure 5.7 Energy and power of IPAC-CMG cluster during the simulation

The torques produced by the actuator system and the corresponding angular momentum values are presented in Figure 5.8. It is clearly seen that the torque commands cannot be realized after the cluster entered into the singular configuration. It is also seen in the figure that the feedback control system also fails after the singularity is reached; the torque commands in y and z directions changes abruptly. This is due to the inversion of the ill-conditioned Jacobian matrix in the steering calculations.

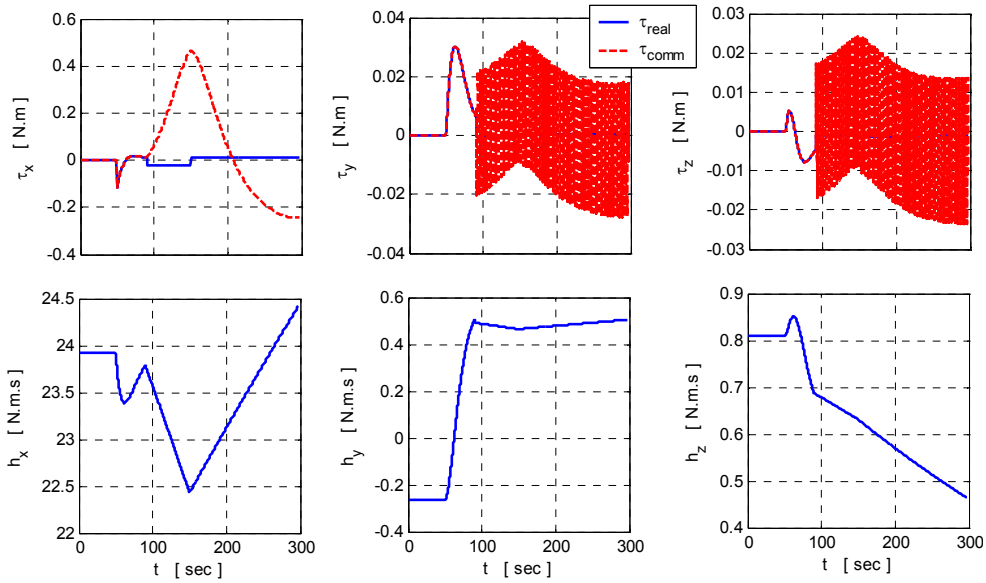

Figure 5.8 Torque and angular momentum of IPAC-CMG cluster during the simulation

The last two figures showing the gimbal configurations and the flywheel spin rates are given in figures Figure 5.9 and Figure 5.10 respectively. Looking at the gimbal configurations, it is seen that the singularity has not taken place at the expected configuration, but it has occurred in the neighborhood of this configuration. This is due to the different flywheel spin rates that each IPAC-CMG has during the simulation. Due to this difference in flywheel spin rates, the IPAC-CMGs have different angular momentums and these different angular momentum vectors trap into singularity in a slightly different configuration than what we have expected.

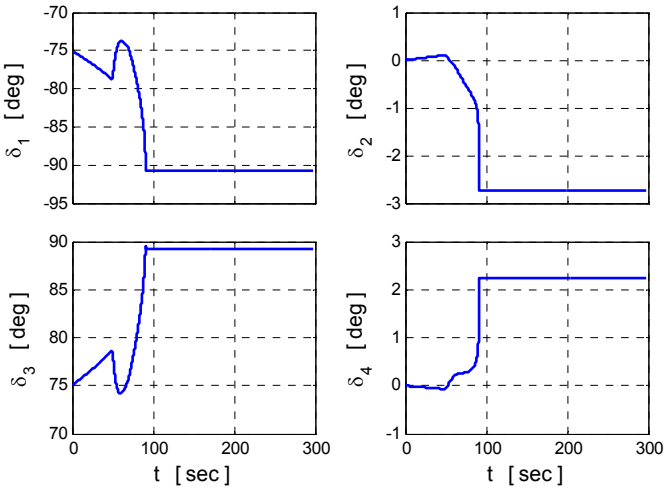

Figure 5.9 Gimbal Configuration of each IPAC-CMG in IPAC-CMG cluster

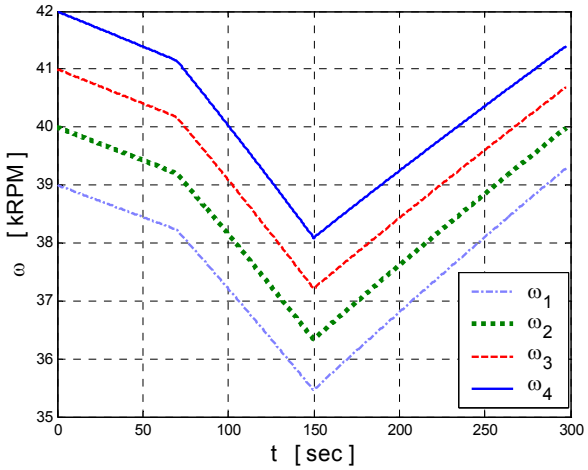

Figure 5.10 Flywheel angular rates of each IPAC-CMG in the cluster

5.3.2 B-inverse Simulations

The above simulation is performed this time using B-inverse algorithms. The command of desired gimbal rotational rate is supplied to the actuator system as before (See Chapter 4). The nodal positions and corresponding gimbal angles used in the simulations are given TABLE 5.2. These nodes are a part of a larger list of nodes used in the CMG simulations in [51]. Note that, here only two nodes are

used to demonstrate that a small number of nodes are enough to drive the system away from the singularity. However the temporal positions of the nodes are different, since the angular momentum capacity of IPAC-CMG cluster is different from the CMG cluster used in the related reference [51].

TABLE 5.2 List of nodes used in B-inverse simulation

Node	Time [sec]	Gimbal Angles [deg]
1	60	[-71.2 37.6 111.4 -34.2]
2	300	[-50.7 100.1 124.3 -80.2]

The blending coefficients of B-inverse are selected as $q_{power} = 1 \times 10^{-1}$ and $q_{attitude} = 1 \times 10^{-5}$.

The results of the simulation are given in the figures below. In the first figure, Figure 5.11, the realized spacecraft attitude is plotted together with respect to the attitude command. The spacecraft completes the commanded roll maneuver smoothly in about 60 seconds as desired. The attitude in pitch and yaw directions didn't change significantly from the commanded values. So, the maneuver is successfully realized by the B-inverse steering law.

In Figure 5.12, it is observed that the singularity measure of IPAC-CMG cluster is in an increasing trend in general. Thus, IPAC-CMG cluster is far from the singularity throughout the simulation.

The energy and power of IPAC-CMG cluster are given in Figure 5.13. These plots show that the power operation of IPACS is performed successfully throughout the simulation.

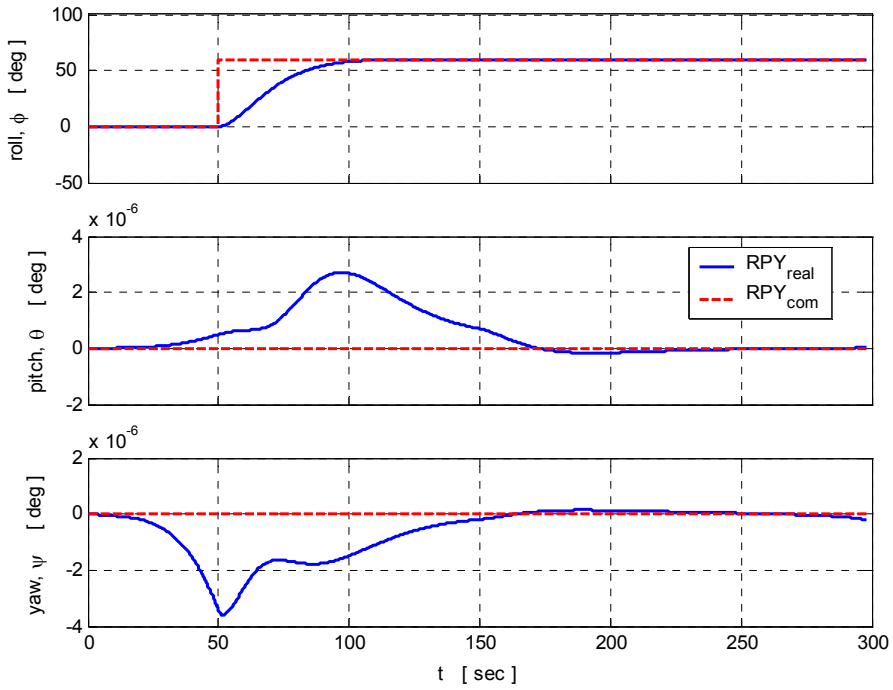

Figure 5.11 Attitude Orientation of the spacecraft during the simulation

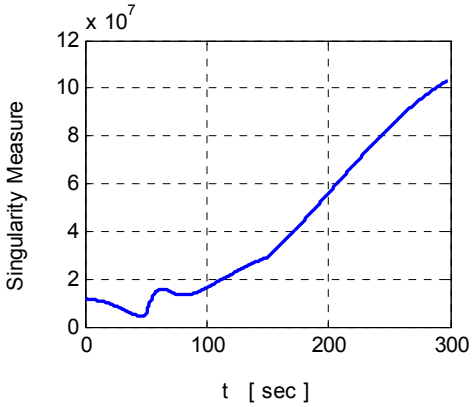

Figure 5.12 Singularity measure during the simulation.

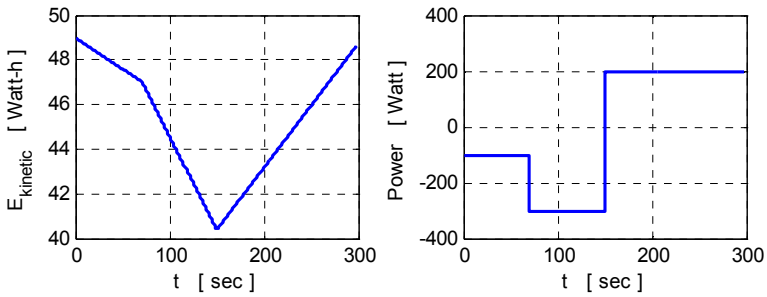

Figure 5.13 Energy and power of IPAC-CMG cluster during the simulation

The torque and angular momentum histories of the IPAC-CMG cluster are also shown in Figure 5.14. The torque and angular momentum profiles obtained during the simulation are smooth and attainable. When examining these profiles, one should bear in mind that the magnitudes of the angular momentum vectors of each IPAC-CMG unit continuously change during the whole simulation while, with the help of B-inverse, the resultant angular momentum vector of the cluster remains the same. In other words, the torques produced by the power operations are simultaneously being eliminated by the counter torques created by appropriate gimbal motions.

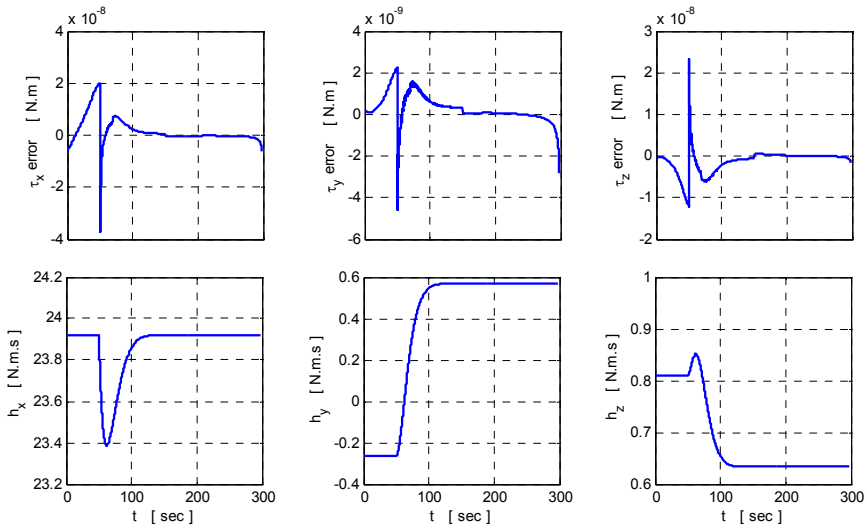

Figure 5.14 Torque and angular momentum plots of IPAC-CMG cluster during the simulation.

It is easily detected from the angular momentum plots given in the figure that, to perform a roll maneuver, the IPAC-CMG cluster produces net internal torque not only in the roll direction but also in all pitch and yaw directions. This is due to the directional couplings existing in the spacecraft dynamics as presented in Eq. 5.6. Since the IPAC-CMG cluster has an initial angular momentum vector with non-zero pitch and yaw components, the IPAC-CMG cluster must reorient its own angular momentum vector when it reorients the spacecraft. In other words, these pitch and yaw torques are not produced for the angular momentum transfer between the IPAC-CMG cluster and the spacecraft, but they are produced to change the direction of the resultant angular momentum vector of the IPAC-CMG cluster

The remaining two figures present the gimbal angles and the flywheel spin rates of each IPAC-CMG unit in the cluster respectively. The gimbal angles, given in Figure 5.15, all change smoothly presenting an attainable profile. The specified nodes are crossed quite closely. This also means that the desired gimbal rotational rates are followed in the desired profile.

The flywheel spin rates of each IPAC-CMG unit in the cluster are presented in Figure 5.16. They are identical to the ones obtained in the previous simulation, in which they were determined directly. Hence, we can conclude that both energy storage and attitude control operations may easily be managed through B-inverse.

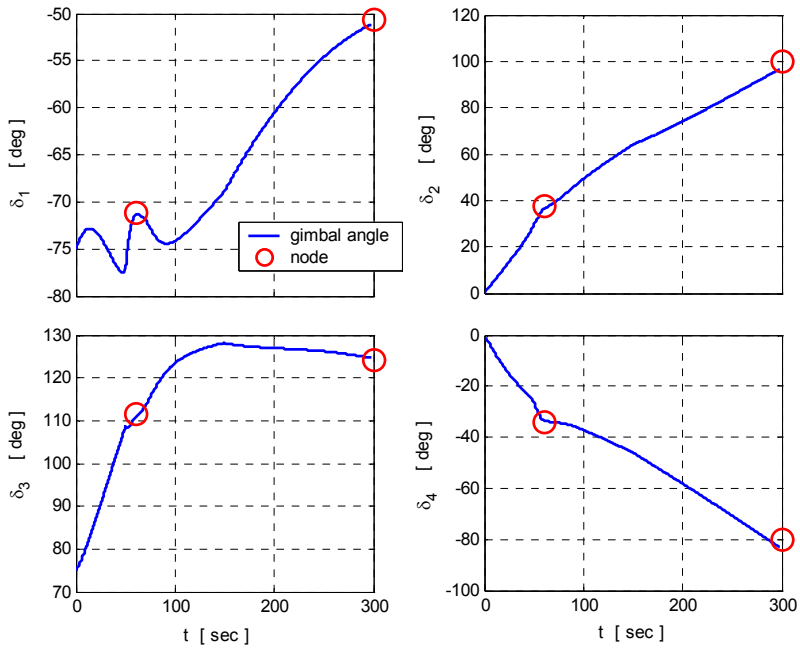

Figure 5.15 The angular orientations of the gimbals during the simulation.

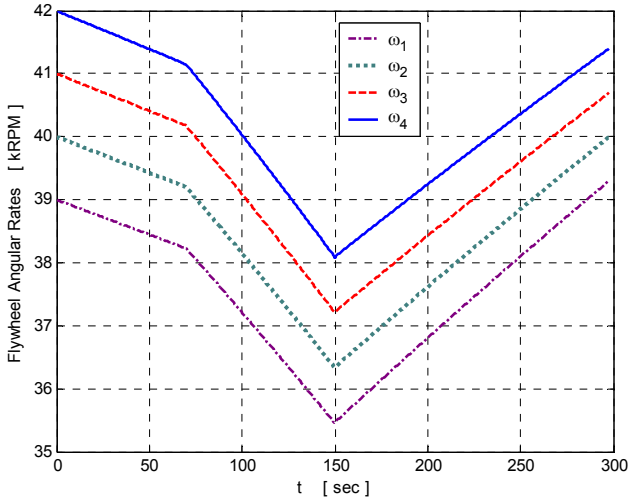

Figure 5.16 Flywheel spin rates during the simulation

CHAPTER 6

CONCLUSION

6.1 Concluding Remarks

In this thesis work, B-inverse is applied to redundant actuator systems.

First, it is shown that B-inverse may successfully steer redundant robotic manipulators as it is on CMG clusters. The repeatability of B-inverse is demonstrated through a redundant robotic manipulator. It is also shown that, given non-singular joint configurations at discrete waypoints (nodes), B-inverse steering law can avoid and transit singularities.

Determination of joint angles at various waypoints (nodes) is quite a straightforward task through optimization algorithms. It may also be performed manually. An operator may position the manipulator links by hand and requests the controller to memorize it as a node. In this way B-inverse steering algorithm not only realizes the desired trajectory, it also passes very close to those nodal joint angle configurations.

In the repeatability test of Chapter 2, it is also shown that the manipulator follows the desired trajectory without any increase in the error that is determined by the control strategy even if the manipulator is given a false nodal joint configuration.

The attitude control and energy storage devices that are commonly used in today's space applications are briefly presented. It is shown that flywheel energy storage is

possible and advantageous- thus, more promising- when it is compared to today's electrochemical storage technology. IPAC-CMG is also compared to its competitors; attitude control actuators and energy storage devices.

B-inverse is also tested on an IPAC-CMG cluster using two separate approaches: steering for attitude control and combined steering for energy management and attitude control. The latter approach is only possible for B-inverse. With B-inverse one may put more weight to any of the two tasks by properly selecting the blending coefficient.

6.2 Future Work

This thesis work is a part of a continuing study on steering of redundant actuators [51,43,3].

Additional B-inverse application policies for different redundant actuator systems and IPACS shall be developed in the future. The intuitions gained through simulations indicate that B-inverse is a repeatable steering algorithm. However, a mathematical proof to the repeatability shall be made in the future.

Turkey has selected the satellite technologies as an area to be acquired and developed. IPAC-CMG is a technology, which may give a foothill to Turkish industry among worldwide satellite industries. Thus, the conceptual design presented in this thesis shall be continued by designing, testing and flying an IPAC-CMG system.

APPENDIX A

IPAC-CMG FLYWHEEL SIZING

A.1 Introduction

A conceptual flywheel sizing is performed here both to provide the necessary parameters to the simulations presented in the previous chapters (Chapter 4, Chapter 5) and to see the key design variables and their effects on the design.

A.2 Governing Equations For The Rotating Annular Cylinder

In sizing the flywheel, the general shape of the flywheel is determined first. A high inertia-to-mass ratio is obtained with an annular cylinder. The entire flywheel designs in the literature are also based on this shape [41,18,32,19,13,1].

Consider the hollow cylinder given in Figure A.1. The mass and the mass moment of inertia of the cylinder are given as

$$m = \rho.t.\pi.R_0{}^2(1-C^2) \tag{A.1}$$

$$I = \frac{1}{2}\rho.t.\pi.R_0{}^4(1-C^4) \tag{A.2}$$

where $C = \frac{R_i}{R_0}$ is the ratio of inner and outer radii that are given in the figure;.

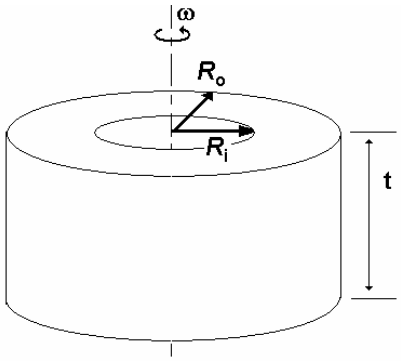

Figure A.1 Sketch of an annular flywheel

The angular momentum equation for this cylinder is

$$h = I.\omega = \frac{1}{2}.\rho.t.\pi.R_0^{\,4}.(1-C^4).\omega \tag{A.3}$$

The kinetic energy of this cylinder, while it is rotating around its symmetry axis with an angular velocity of ω is stated by

$$E_{kin} = \frac{1}{2} I\omega^2 \tag{A.4}$$

For an energy-storing cylinder, having maximum and minimum angular velocities of $\omega_{\max}$ and $\omega_{\min}$, the total amount of energy stored is given by

$$E_{stored} = \int_{\omega_{\max}}^{\omega_{\min}} I.\omega.d\omega = \frac{1}{2} I\omega_{\max}{}^2 (1 - \frac{\omega_{\min}{}^2}{\omega_{\max}{}^2}) \tag{A.5}$$

in which depth of discharge for this storage element becomes

$$DOD = 1 - \frac{\omega_{\min}{}^2}{\omega_{\max}{}^2} \tag{A.6}$$

Furthermore, substituting Eq. A.2 for I in Eq. A.5, the energy equation for the flywheel becomes

$$E_{stored} = \frac{1}{4}.\rho.t.\pi.R_0^{\,4}.(1-C^4).\omega_{\max}^{\,2}.DOD \tag{A.7}$$

The key metric of energy storage systems, the specific energy, which denotes the energy stored per unit mass, is given as:

$$SE = \frac{E_{stored}}{m} = \frac{\frac{1}{4}.\rho.t.\pi.R_0^{\,4}.(1-C^4).\omega_{\max}^{\,2}.DOD}{\rho.t.\pi.R_0^{\,2}(1-C^2)} = (\frac{1}{4}\omega_{\max}^{\,2}DOD).R_0^{\,2}(1+C^2) \tag{A.8}$$

It is seen that, the amount of energy stored in unit mass may be adjusted either by changing the angular rates of the flywheel through the parameters $\omega_{\max}$ and DOD or by changing the shape of the flywheel through R_0 and C.

Here, DOD is the parameter that depends only on the ratio of the maximum and minimum angular velocities of the flywheel. This relationship is presented in Figure A.2. The graph shows that the ratios over 4 do not produce significant gains in the energy.

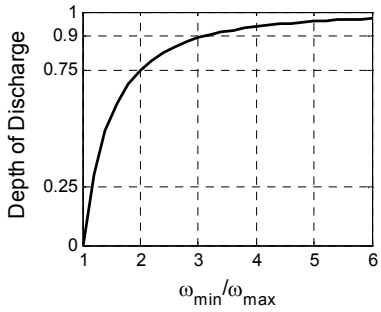

Figure A.2 Depth of discharge as a function of angular speed ratio

The rest of the variables that affects the specific energy are all related to eachother through the rotation-induced stress equations. For this, stress equations for the rotating annular cylinder should be considered.

Eq.A.9a and Eq.A.9b give the rotation-induced stresses in a rotating annular cylinder in tangential and radial directions respectively [41]. Note that, these equations govern the applications with both anisotropic (e.g., composites) materials and isotropic materials (e.g., metals).

$$\sigma_\theta = \mathrm{P}_1.\left\{(3+\nu_\theta).k.[\mathrm{P}_2-\mathrm{P}_3]-(k^2+3.\nu_\theta).(\frac{r}{R_0})^2\right\} \tag{A.9a}$$

$$\sigma_r = \mathrm{P}_1.(3+\nu_\theta).\left[\mathrm{P}_2+\mathrm{P}_3-(\frac{r}{R_0})^2\right] \tag{A.9b}$$

where

$$\begin{aligned}
\mathrm{P}_1 &= \frac{\rho.\omega^2.{R_0}^2}{9-k^2} \\
\mathrm{P}_2 &= \frac{1-C^{k+3}}{1-C^{2k}}.(\frac{r}{R_0})^{k-1} \\
\mathrm{P}_3 &= \frac{1-C^{k-3}}{1-C_{2k}}.C^{k+3}.(\frac{R_0}{r})^{k+1}
\end{aligned} \tag{A.10}$$

and

$$k = \sqrt{\frac{E_\theta}{E_r}} \tag{A.11}$$

which is the stiffness coefficient. $k = 1$ for isotropic materials and $k > 1$ for anisotropic materials (e.g., $k \approx 4$ for carbon composites). υ_θ is the Poisson's Ratio in tangential direction.

To visualize the stress distributions in the cylinder defined by Eq.A.9a and Eq.A.9b, normalized tangential (hoop) and radial stress distributions over radius are presented in Figure A.3 and Figure A.4. The stresses are normalized by the factor of $\rho\omega^2 R_0$.

In Figure A.3, stress distributions are plotted for different C values for isotropic materials, where $k = 1$. And the same plot is drawn for the anisotropic materials with $k = 4$ in Figure A.4.

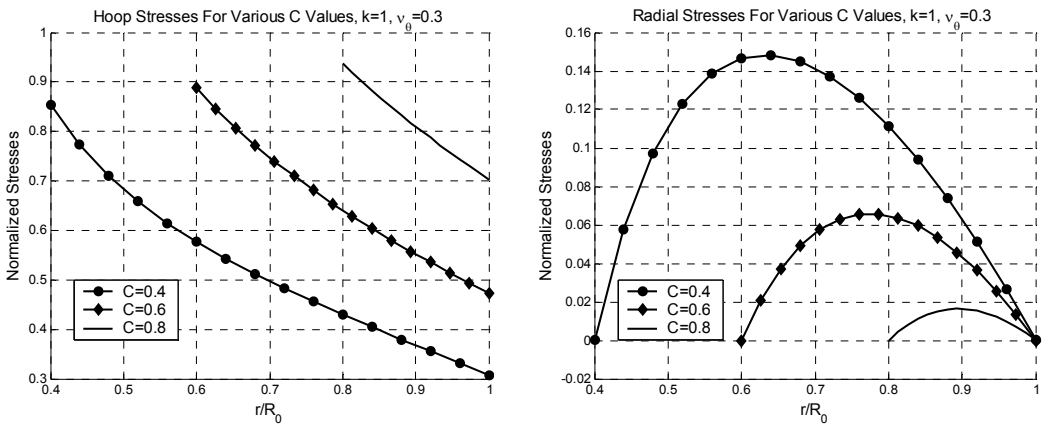

Figure A.3 Hoop and radial stress values throughout the cylinder for various values of *C* for isotropic materials

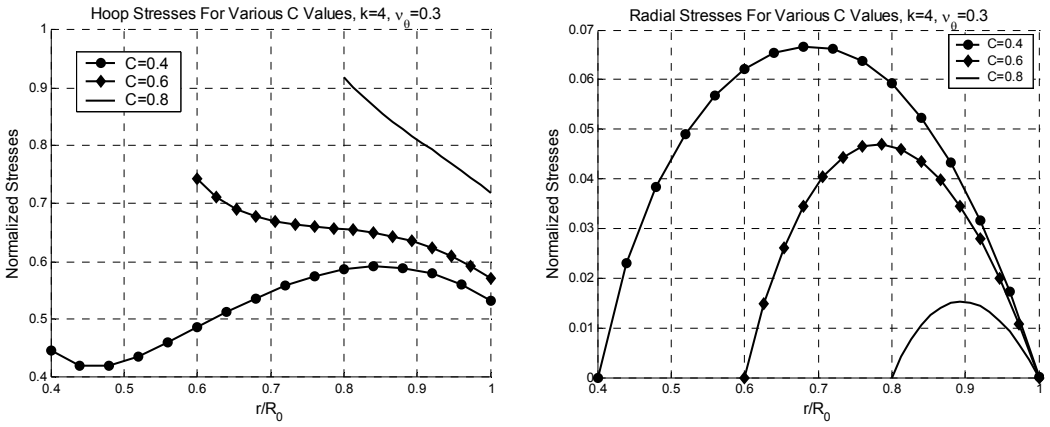

Figure A.4 Hoop and radial stress values throughout the cylinder for various values of C for anisotropic materials

In these plots, notice that as C increases the hoop stresses also increase whereas the radial stresses decrease in both cases. On the other hand, the radial stress levels are lower in the anisotropic material. Also the peak stress values occur in different radial positions in isotropic and anisotropic materials, especially in the hoop stresses, which is the critical stress type in this case. The hoop stresses are distributed better for the anisotropic materials. This distribution greatly reduces the innermost stresses in the anisotropic material as C decreases. From the stress distribution point of view, it would be advantageous to employ an anisotropic material in this application.

A.3 Sizing Calculations

Number of sizing calculations are carried out and results are presented in this section. The sizings are made for a spacecraft with the attitude and energy storage requirements given in TABLE A.1. The energy storage capacity and the angular momentum capacity of the spacecraft are the design drivers.

TABLE A.1 Requirements per IPAC-CMG For Conceptıual Design

	Spacecraft Need	**Per IPAC-CMG**
Energy Storage [Wh]	100	25
Ang. Mom. Capacity [Nms]	6	1.9

The angular momentum capacity of the spacecraft indicates the capacity of the spacecraft in all three axis. Each IPAC-CMG should have 1.9 Nms of angular momentum for the cluster to have 6 Nms of angular momentum capacity in each direction, for a CMG cluster in pyramid configuration with a skew angle of 54.73 deg [51].

As discussed in Chapter 3, design of an IPAC-CMG should be based on the minimum angular momentum. Thus, the angular momentum value given in TABLE A.1 should be considered as the minimum angular momentum value of the flywheel, which is obtained by substituting $\omega_{\min}$ with ω in Eq. A.7.

The thickness of the flywheel (t in Figure A.1) is taken constant ($t = 10$ cm) in the calculations. If the motor/generator system, which is required to operate the flywheel between its maximum and minimum angular speeds, is to be installed into the flywheel, this value should be determined by the height of the motor/generator. However, this is a problem that is to be handled in the detail design phase. In this thesis work, the conceptual drawing is given in Figure A.5 to demonstrate the idea.

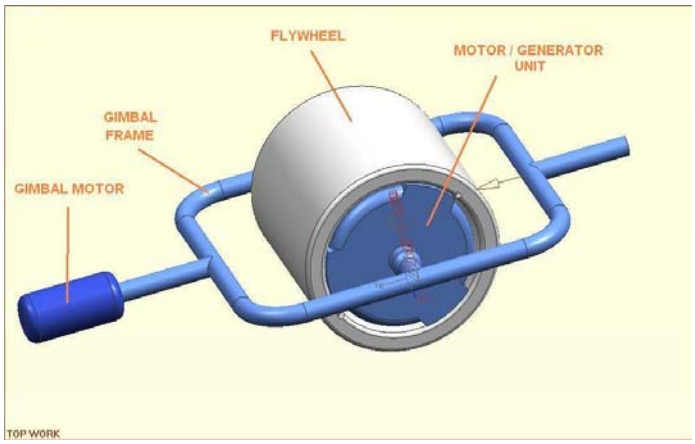

Figure A.5 A 3-D illustration of an IPAC-CMG

The sizing calculations are performed using two different metals and two composites. The properties of these materials are presented in TABLE A.2.

TABLE A.2 Material Properties [41,47]

	ρ [kg/m^3]	E_θ [GPa]	E_r [GPa]	S_θ [Mpa]	S_r [Mpa]	υ_θ	v_f
Steel (AISI 302)	7920	190	190	520	520	0.3	-
Titanium (6Al-4V)	4730	115	115	830	830	0.3	-
E-Glass (Glass/Epoxy)	2000	39	8.6	1080	15	0.28	61%
Toho G30 (Carbon/Epoxy)	1510	142	10.3	2280	15	0.27	60%

First sizing calculations are performed for a fixed maximum angular speed of 30 kRPM and DOD of 0.9375, which corresponds to an angular speed ratio of 4. The sizes obtained with each material are given in TABLE A.3. The calculations are performed using three different C values.

TABLE A.3 List of Flywheel Sizing Results

For ω_{max} = 30 *kRPM* , *DOD = 0.9375* , *t = 0.1 m* , E_{stored} = 25 ± 0.5 *Wh*							
Material	**C**	**R_0 [m]**	**m [kg]**	**SE [Wh/kg]**	**h_{min} [N.m]**	**$\sigma_0)_{max}/S_0$**	**$\sigma_r)_{max}/S_r$**
Steel	0.6	0.065	6.73	3.7	15.2	0.56	0.04
Steel	0.8	0.072	4.64	5.5	15.5	0.73	0.013
Steel	0.9	0.082	3.18	7.8	15.2	0.98	0.004
Titanium	0.6	0.074	5.21	4.8	15.2	0.27	0.02
Titanium	0.8	0.082	3.60	7.1	15.6	0.35	0.006
Titanium	0.9	0.094	2.49	10.3	15.7	0.48	0.002
E-Glass	0.6	0.092	3.40	7.4	15.4	0.13	0.67
E-Glass	0.8	0.101	2.31	10.8	15.2	0.17	0.22
E-Glass	0.9	0.116	1.61	15.7	15.4	0.24	0.07
Toho G30.	0.6	0.099	2.98	8.6	15.6	0.05	0.47
Toho G30	0.8	0.109	2.03	12.5	15.5	0.07	0.18
Toho G30	0.9	0.124	1.38	17.9	15.1	0.1	0.06

In the results it is seen that carbon composite Toho G30 gives minimum stresses as well as minimum mass for all C values. So Toho G30 is decided to be the suitable material for this IPAC-CMG flywheel design.

It is already seen in Eq. A.8 that an increase in C increases the specific energy of the flywheel, leading to a lower mass. But in TABLE A.3 it is also seen that for every material, an increase in C decreases the increases hub stresses and decreases radial stresses in the flywheel. Having radial stresses larger than hub stresses has an advantage in a probable failure of the flywheel since a crack due to radial stresses would be circumferential whereas a crack due to hub stresses would be radial as seen in Figure A.6. A radial crack is fatal for the flywheel since it would tear the whole flywheel apart but a circumferential crack would tear respectively smaller pieces from the flywheel, which is a less hazardous type of failure. In

addition, higher C value means added bulkiness to the system. Due to these, $C = 0.9$ is not preferable for this flywheel design. The composite materials have radial stresses higher for $C = 0.8$, so this value is selected.

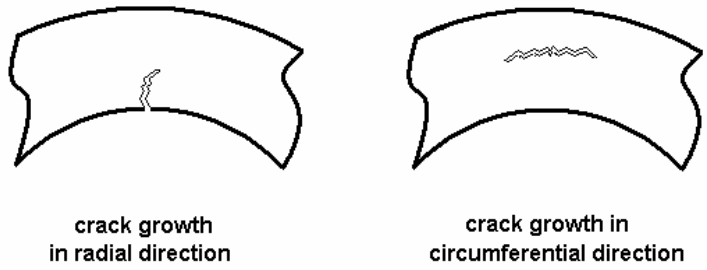

Figure A.6 Illustration of radial and circumferential cracks due to hub and radial stresses respectively

As the material and the parameter C are determined, the maximum angular velocity should be selected for the flywheel. TABLE A.4 gives the calculation results made for different maximum angular speeds.

TABLE A.4 Sizing results for different maximum flywheel speeds

For $C = 0.8$, $DOD = 0.9375$, $t = 0.1\ m$, $E_{stored} = 25 \pm 0.5\ Wh$								
Material	**ω_{max} [kRPM]**	**R_0 [m]**	**m [kg]**	**SE [Wh/kg]**	**h_{min} [N.m]**	**I [kg.m^2]**	**$\sigma_0)_{max}/S_0$**	**$\sigma_r)_{max}/S_r$**
Carb. Comp.	30	0.109	2.03	12.5	15.5	0.0197	0.07	0.18
Carb. Comp.	60	0.077	1.01	25.0	7.7	0.0049	0.14	0.36
Carb. Comp.	120	0.054	0.505	50.0	3.84	0.0012	0.28	0.72
Carb. Comp.	240	0.039	0.253	100	1.93	3.1×10^{-4}	0.57	1.45

Looking at the results given in the last row of TABLE A.4, it is seen that the maximum rotation-induced radial stress in the flywheel is 45% higher than the radial strength of the material. But the angular momentum of at that speed is nearly the exact amount that satisfies the angular momentum requirement of a single IPAC-CMG. At an angular speed lower than 240 kRPM, IPAC-CMG flywheel would have excess amount of angular momentum on it. That is why it is necessary to go up to such high speeds in these applications.

The material is not the only limiting factor in going up to higher speeds. Mechanical bearings quickly wear out in rotational speeds higher than 30 kRPM, so magnetic bearing technology is used for higher speeds. The problem with the magnetic bearings is that they require complex active control techniques. 60 kRPM of angular speed is reported to be reached in such an application [18]. Thus, to stay in the limits of today's technology, the maximum angular speed of the IPAC-CMG flywheel is selected to be 60 kRPM for this thesis work.

The final parameters of the flywheel design are listed in TABLE A.5 below.

TABLE A.5 Properties of the IPAC-CMG flywheel

Material	Toho G30
Outer radius, R_0 [m]	0.077
Thickness, t [m]	0.1
Ratio of inner radius to outer radius, C	0.8
Mass, m [kg]	1.01
Mass Moment of Inertia, I [kgm^2]	0.0049
Minimum Angular Momentum, h_{min} [Nms]	7.7
Maximum angular speed, ω_{max} [kRPM]	60
Depth of Discharge, DOD	0.9375
Energy storage Capacity, E_{stored} [Watt-hour]	25

APPENDIX B

NODE DETERMINATION BY STANDARD OPTIMIZATION TECHNIQUES

The nodal joint angles that are used in B-inverse simulations of the 3-link planar robotic manipulator are determined using the derivative-based single objective optimization technique offered by MATLAB. The aim of this is to show the application ease of B-inverse. The m-files that are used for node determination are presented below.

B.1 Knotfinder.m

```
function [ thetas, rs ] = knotfinder ( r0, theta0, lb, ub, le )
% KNOTFINDER finds the joint angle sets for the desired end-effector
% coordinates at all the knots. Works with coster.m & kinematics.m
%
% Specify r0, le, lb, theta0 and ub in the workspace, all being matrices
% with rows for each knot to be identified
%
% r0       ==> target positions, i.e. [1.3 0 ; 1 0]
% theta0 ==> initial guess of joint angles,    i.e. [pi/10 pi/2 pi ; 0 pi pi]
% lb       ==>  lower bounds to joint angles,  i.e.  [0 0 pi/2 ; 0 pi/6 pi/6]
% ub       ==>  upper bounds to joint angles, i.e. [pi pi 2*pi ; pi 2*pi pi ]
% le       ==>  link lengths                          i.e. [1 0.8 0.5]
% Usage :    [ thetas, rs ] = nodefinder ( r0, theta0, lb, ub, le );

rad = pi/180 ; % radians
knot = size (r0) ;
knot = knot (1) ; % # of knots

% options for the MatLab optimization command "fmincon"
optionss = optimset ('Display','iter','TolFun',1e-15,'TolX',1e-15);
```

```
thetas = [] ; rs = [] ;

for i = 1: knot

   % the optimization command "fmincon" is used
   theta = fmincon (@coster,theta0,[],[],[],[],lb,ub,[],optionss,r0,le);

   % display the local minimum obtained by "fmincon"
   disp ('   ')
   disp ([ 'joint angles in knot ' num2str(i) ' are :'] )
   disp (num2str(theta/rad))
   disp (['in degrees'])
   disp ('   ')
   r_real = kinematics (theta, le);


   disp (['realized position of the end-effector at knot ' num2str(i) ' is :'])
   disp (num2str(r_real))
   disp('  ')
   disp ( 'error between realized and desired positions is ')
   err = r0'-r_real
   thetas = [thetas theta] ;
   rs = [rs r_real] ;

end
```

B.2 coster.m

```
function cost = coster( theta, r0, le )
% COSTER gives the cost function for the script knotfinder.m
% Calculates the difference (cost) between desired position of
% the end effector and the current one as optimization progresses,
% using the kinematic relation between joint angles and end effector
% position

r= kinematics (theta,le) ; % kinematics for the current configuration

W = [1 1] ; % cost weighting

cost = W(1)*((r0(1)-r(1))^2)+W(2)*((r0(2)-r(2))^2) ;
```

B.3 kinematics.m

```
function r = kinematics( Th, le )
% KINEMATICS gives the direct kinematic relationship for the specified
% manipulator. Tailored to be used with knotfinder.m to determine knots.

% Three link planar manipulator kinematics
l1 = le(1) ; l2 = le(2) ; l3 = le(3) ;
r1 =  l1 * cos(Th(1)) - l2 * cos(Th(1)+Th(2)) + l3 * cos(Th(1)+Th(2)+Th(3));
r2 =  l1 * sin (Th(1)) - l2 * sin(Th(1)+Th(2)) +  l3 * sin(Th(1)+Th(2)+Th(3));

r = [r1;r2]; % x position, y position (and any third constraint, if any)
```

REFERENCES

1. Active Power, Inc., “Active Power”, http://www.activepower.com/, September 2005, last date accessed: 20.11.2005

2. Ahuactzin,J.M.,Gupta,K.K., “The Kinematic Roadmap: A Motion Planning Based Global Approach for Inverse Kinematics of Redundant Robots”, IEEE Transactions on Robotics and Automation, vol. 15, August 1999, pp. 653-669

3. Altay,A.,Tekinalp,O., “Spacecraft Energy Storage and Attitude Control”, IEEE Proceedings of 2nd International Conference on Recent Advances in Space Technologies, June 2005, pp. 201-206

4. Anderson, W. W., Keckler, C.R., “An integrated power/attitude control system (IPACS) for space application,” Proceedings of the 5th IFAC Symposium on Automatic Control in Space, 1973.

5. Babuska, V., et. al.,”A Review of Technology Developments in Flywheel Attitude Control and Energy Transmission Systems”, IEEE Aerospace Conference Proceedings, 2004, pp. 2784-2800

6. Bedrossian, N. S., “Classification of Singular Configurations For Redundant Manipulators,” IEEE International Conference on Robotics and Automation, 1990, pp. 818-823

7. Bedrossian, N.S., “Steering Law Design for Redundant Single Gimbal control moment gyroscpoes,” M.Sc. Thesis, MIT, 1987

8. Christopher, D. A., Beach, R., “Flywheel technology development program for aerospace applications”, IEEE Proceedings of the National Aerospace and Electronics Conference, 1997

9. Brown,C.D., “Elements of Spacecraft Design”, AIAA Education Series, 2002

10. Duleba, I., Sasiadek, J.Z., “Redundant Manipulators Motion Through Singularities Based On Modified Jacobian Method,” 3rd Int. Workshop on Robot Motion and Control, 2002, pp. 331-336

11. EADS SPACE Transportation, “EADS Hydrazine Thrusters”, http://cs.space.eads.net/sp/SpacecraftPropulsion/MonopropellantThrusters.html#ModelCHT400, February 2005, last date accessed: 20.11.2005

12. Fausz, J.L., Richie D.J., “Flywheel Simultaneous Attitude Control and Energy Storage Using a VSCMG Configuration”, Proc. Conf. Control Applications, September 2000, pp. 991-995

13. Ginter,S., Gisler,G., Hanks,J.,”Spacecraft Energy Storage Systems”, IEEE AES Systems Magazine, May 1998, pp. 27-32

14. Hall,C.D., ”Integrated Spacecraft Power and Attitude Control Systems Using Flywheels”, Air Force Institute of Technology Technical Report, 1997

15. Hansen, F., Danish Space Research Institute, “Satellite Technology Course Electrical Power Subsystem,” http://www.dsri.dk/roemer/pub/sat_tech, May 2004, last date accessed: 20.11.2005

16. Honeywell Aerospace, “Pointing and Momentum Control”, http://www.honeywell.com/sites/aero/Pointing-Momentum-Control.htm, January 2005, last date accessed: 20.11.2005

17. Kelly, C.O., Wilson, S., “Satellite cell development: lithium-ion profile,” 12thAIAA/USU Small Satellite Conference, SSC98-I-1, 1998

18. Kenny, B.H., Kascak, P.E., Jansen, R., Dever, T., Santiago W., “Control of a high speed flywheel system for energy storage in space applications,” NASA/TM –2004-213356, October 2004

19. Kirk, J.A., Schmidt, J.R., Sullivan, G.E., Hromada, L.P., “An open core rotator design methodology”, IEEE National Aerospace and Electronics Conference, 1997, pp. 594-601

20. Klein,C.A., Huang,C.H., “Review of Pseudoinverse Control for Use with Kinematically Redundant Manipulators”, IEEE Transactions on Systems, Man and Cybernetics, vol. SMC-13, 1983, pp. 245-250

21. Lappas,V.J., “A Control Moment Gyro Based Attitude Control System for Agile Satellites”, Ph.D. Dissertation, University of Surrey, October 2002

22. Lin, C.S., Chang, P.R., “Joint Trajectories of Mechanical Manipulators for Cartesian Path Approximation,” IEEE Transactions on Systems, Man and Cybernetics, 1983

23. Lin, C.S., Chang, P.R., Luh, J.Y.S., "Formulation and Optimization of Cubic Polynomial Joint Trajectories for Industrial Robots," IEEE Transactions on Automatic Control, 1983

24. Lorenzo, S., and S. Bruno, "Modeling and Control of Robot Manipulators", Mc Graw Hill, New York, 1996

25. Manzo, M.A., Strawn, D.M., Hall, S.W., "Aerospace nickel-cadmium cell verification – final report," NASA/TM –2001-210598

26. Margulies, G., Auburn J.N., "Geometric theory of single-gimbal control moment gyro systems", Journal of the Astronautical Sciences, Vol. 26, No. 2, 1978, pp. 159-191

27. Mayorga, R.V., Wang, A.K.C., "A Singularities Prevention Approach For Redundant Robot Manipulators", Proceedings of IEEE International Conference on Robotics and Automation, 1990

28. McDowall, J., "Nickel-cadmium batteries for energy storage applications," 14th Annual Battery Conference on Applications and Advances, IEEE, 1999, pp. 303-308

29. Microcosm, Inc., "Magnetic Torquers for Spacecraft", http://www.smad.com/analysis/torquers.html, January 2005, last date accessed: 20.11.2005

30. Nakamura, Y., Hanafusa, H., "Inverse Kinematic Solutions With Singularity Robustness for Robot Manipulator Control," Journal of Dynamics, Measurement and Control, vol 108, 1986, pp. 163-171

31. NASA GRC Electrochemistry Branch, "Evolution of Flight Batteries", http://www.grc.nasa.gov/WWW/Electrochemistry/doc/batteries.html, July 2002, last date accessed: 20.11.2005

32. NASA GRC Power & Propulsion Office, "Aerospace Flywheel Development", http://space-power.grc.nasa.gov/ppo/projects/flywheel /index.html, October 2004, last date accessed: 20.11.2005

33. Oh H.S., Vadali S.R., "Feedback control and steering laws for spacecraft using single gimbal control moment gyros," Journal of the Astronautical Sciences, Vol. 39, No. 2, 1994, pp. 183-203

34. O'Neil, K.A., Chen, Y., Seng, J., "Escapability of Singular Configuration for Redundant Manipulators via Self –Motion," IEEE Int. Conf. on Intelligent Robots and Systems ,vol. 3, 1995, p. 3078

35. O'Neil, K.A., Chen, Y., Seng, J., "On The Existence and Characteristics of Solution Paths at Algorithmic Singularities," IEEE Transactions on Robotics and Automation, vol. 14,1998, pp. 336-342

36. Roes, J.B., "An electro-mechanical energy storage system for space application," Progress in Astronautics and Rocketry, vol. 3, New York: Academic Press, 1961, pp. 613-622

37. Schaufler, R., Fedrowitz, C.H., Kammüller, R., "A Simplified Criterion for Repeatability and its Application in Constraint Path Planning Problems", Proceedings of the 2000 IEEE/RSJ Int. Conf. on Intelligent Robots and Systems, 2000, pp. 2345-2350

38. Shamir, T., Yomdin, Y., "Repeatability of Redundant Manipulators: Mathematical Solution of the Problem", IEEE Transactions on Automatic Control,vol. 33, 1988, pp. 1004-1009

39. Sidi M.J., "Spacecraft Dynamics and Control", Cambridge University Press,1997

40. Steyn, W.H., "Photo Gallery", http://staff.ee.sun.ac.za/whsteyn/photo.htm, July 2004, last date accessed: 20.11.2005

41. Taehan, K., "Design of composite flywheel rotors with soft cores," Ph. D. Dissertation, Stanford University, March 2003

42. Tchoń, K., Muszyński, R., "Singular Inverse Kinematic Problem for Robotic Manipulators: A Normal Form Approach," IEEE Transactions on Robotics and Automation, vol. 14, 1998, pp. 93-104

43. Tekinalp, O., Yavuzoglu, E., "A New Steering Law for Control Moment Gyroscope Clusters," Aerospace Science and Technology, vol 9, 2005, pp. 626-634

44. Tsiotras, P., Shen, H., Chris, H., "Satellite attitude control and power tracking with energy/momentum wheels," Journal of Guidance, Control, and Dynamics, Vol. 24, No.1, 2001, pp. 23-34

45. University of California Integration Engineering Laboratory, "Interactive Motion Control", iel.ucdavis.edu/projects/imc/, October 2005, last date accessed: 20.11.2005

46. Wampler, C. W., “Manipulator inverse kinematic solutions based on vector formulations and damped least squares methods,” IEEE Transactions on Systems, Man, and Cybernetics, vol. 16, 1986, pp. 93-101

47. Wertz, J.R., Larson, W.J., “Space mission analysis and design”, 2nd edition, Torrance, CA: Microcosm Inc., 1995

48. Wertz, J.R., “Spacecraft Attitude Determination and Control”, D.Reidel Publishing Company, 1978

49. Whitney,D.E., “Resolved Motion Rate Control of Manipulators and Human Prostheses,” IEEE Transactions on Man-Machine Systems, Vol. 10, 1969, pp 47-53

50. Wie, B., “Space vehicle dynamics and control,” AIAA Educational Series, Tempe, Arizona, 1998

51. Yavuzoglu, E., “Steering laws for control moment gyroscopes used in spacecraft attitude control,” M. Sc. Thesis, Middle East Technical University, November 2003

52. Yoon, H. and Tsiotras, P., "Singularity Analysis of Variable Speed Control Moment Gyros," AIAA Journal of Guidance, Control, and Dynamics, Vol. 27, No. 3, pp. 374-386, 2004

53. Yoon, H. and Tsiotras, P., "Spacecraft Adaptive Attitude and Power Tracking with Variable Speed Control Moment Gyroscopes”, Journal of Guidance, Control and Dynamics, vol. 25, 2002, pp. 1081-1090

54. Yoshikawa, T., “Manipulability of Robotic Mechanisms,” The International Journal of Robotics Research, vol.4, 1985, pp. 3-9